Università degli Studi di Torino

Scuola di Scienze della Natura

Dipartimento di Fisica

Laurea Magistrale in Fisica

The SST camera for CTA: the commissioning facility and first measurements

Supervisor:

Prof. Andrea Chiavassa

Co-Supervisor:

Dr. Davide Depaoli

Examiner:

Prof. Alessandro Ferretti

Candidate:

Isabella Sofia

A.Y. 2022/2023

Abstract

Imaging Atmospheric Cherenkov Telescopes (IACTs) are reliable and powerful detectors for gamma-ray astronomy, a branch of astroparticle physics that studies Very High Energy (VHE) photons produced by non-thermal processes in the Universe.

These telescopes allow us to capture the Cherenkov light emitted by the particles of a gamma-ray induced extensive air shower (EAS); by analyzing these images it is possible to reconstruct the energy and direction of the primary particle.

The Cherenkov Telescope Array (CTA) will be the next generation observatory in this field, equipped with up to one hundred telescopes of different sizes in two different sites in the northern and southern hemispheres.

This thesis is dedicated to the Small-Sized Telescopes (SSTs), with a specific focus on the development of their detectors, which are silicon photomultiplier-based cameras, and of a facility required to verify the performance and functionality of all the cameras intended for the southern site of CTA.

The scientific context of gamma-ray astronomy is presented first, followed by a description of the IACT technique and of the CTA observatory. SSTs are then introduced, with a particular emphasis on silicon photomultipliers and on the final design of the SST camera.

An entire chapter is then dedicated to the study and development of the commissioning facility for such detectors performed at the Max Planck Institut für Kernphysik in Heidelberg, Germany.

Finally, the last chapter centres on initial measurements carried out on one of the first SST camera modules, along with an analysis of the camera's heat dissipation.

Contents

List of Tables

List of Figures

Chapter 1

Gamma Rays: neutral cosmic messengers

In astroparticle physics, the term "gamma rays" is used to refer to photons that are so energetic that they must be produced in a non-thermal way, i.e. in peculiar cosmic environments that are not in hydrostatic equilibrium, so very different from, for example, stars like our Sun.

These astrophysical objects act as powerful particle accelerators and are therefore extreme environments where peculiar phenomena can take place. As the accelerated Cosmic Ray (CR) particles travel through the region surrounding their source and into farther regions, they undergo not only diffusion, but also energy losses caused by various mechanisms: some of these mechanisms can lead to the production of γ-rays and will be discussed in the following sections (1.1), together with the description of methods to detect such Gamma Rays (1.2).

First, it is useful to remember that γ-rays are typically classified into different energy bands according to their energy:

- Low/Medium energy (LE/ME), 0.1 MeV $\leq E <$ 30 MeV
- High energy (HE), 30 MeV $\leq E <$ 100 GeV
- Very High energy (VHE), 100 GeV $\leq E <$ 100 TeV
- Ultra High energy (UHE), $E \geq$ 100 TeV

1.1 Producing γ-rays

Gamma rays can be emitted by various channels, in particular by two types of processes, characterised by whether the physical origin of the cosmic ray is leptonic or hadronic: hence, we refer to the *leptonic model* or the *hadronic model*.

Leptonic processes

The main interpretation for the high-energy photons in the astrophysical leptonic model is the so-called Synchrotron Self Compton (SSC) mechanism, which can be divided into two

distinct processes: synchrotron radiation and Inverse Compton (IC) scattering. In this phenomenon, relativistic electrons traveling in a magnetic field emit photons (Synchrotron emission) with a spectrum ranging from the infrared to the X-rays. This synchrotron radiation is polarised and boosted into the direction of motion of the particle with an opening angle inversely proportional to its Lorentz factor Γ: the power of this radiation, which is also the energy loss of the particle, is for an electron

$$P_{sync} = -\left(\frac{dE}{dt}\right) = \frac{4}{3} c\sigma_T \left(\frac{E}{mc^2}\right)^2 \beta^2 u_B$$

where σ_T and u_0 are the Thomson cross-section and the energy density of the magnetic field, defined by

$$\sigma_T = \frac{8\pi}{3}\left[\frac{e^2}{m_e c^2}\right]^2, \qquad u_B = \frac{B^2}{2\mu_0}$$

Here, μ_0 is the magnetic permeability of the vacuum.

Synchrotron emission will be stronger for lighter particles, since $P_{sync} \propto \sigma_T \cdot 1/m^2 = 1/m^4$; the radiation emitted by a single electron of energy E_e can be described by an energy spectrum peaked at a characteristic energy of [1]

$$E_{sync} \simeq 0.2\left(\frac{E_e}{1\ \text{TeV}}\right)^2 \left(\frac{B}{10\ \ \mu\text{G}}\right)\ \text{eV}$$

The second process involved in the production of gamma rays is the Inverse Compton Scattering, which is the scattering between a low-energy photon and a high-energy electron, resulting in a boosted photon and an energy loss for the electron. In general, such an interaction can take place between cosmic electrons and photons of the Cosmic Microwave Background (CMB) or starlight, for example. The energy loss of the electron can be approximately described by

$$P_{IC} = -\left(\frac{dE_e}{dt}\right) = \frac{4}{3} c\sigma_T \left(\frac{E_e}{m_e c^2}\right)^2 \beta^2 u_R$$

where u_R is the energy density of the ambient radiation field. The energy of the scattered photon is given by

$$E_{IC} \simeq 33\left(\frac{E_e}{1\ \text{TeV}}\right)^2 \left(\frac{E_{ph}}{1\ eV}\right)\ \text{TeV}$$

For example, an electron of energy E_e of 100 TeV that interacts via IC with a CMB photon having $E_{ph} \simeq 6 \cdot 10^{-4}$ eV, will produce a $\simeq 10$ TeV γ-ray. Here we are interested in the Synchrotron Self Compton scattering, where the photons emitted by the synchrotron process are the target for the same electrons that emitted them. The Inverse Compton process can greatly increase the energy of a photon. Figure 1.1 shows the Synchrotron and Inverse Compton spectra.

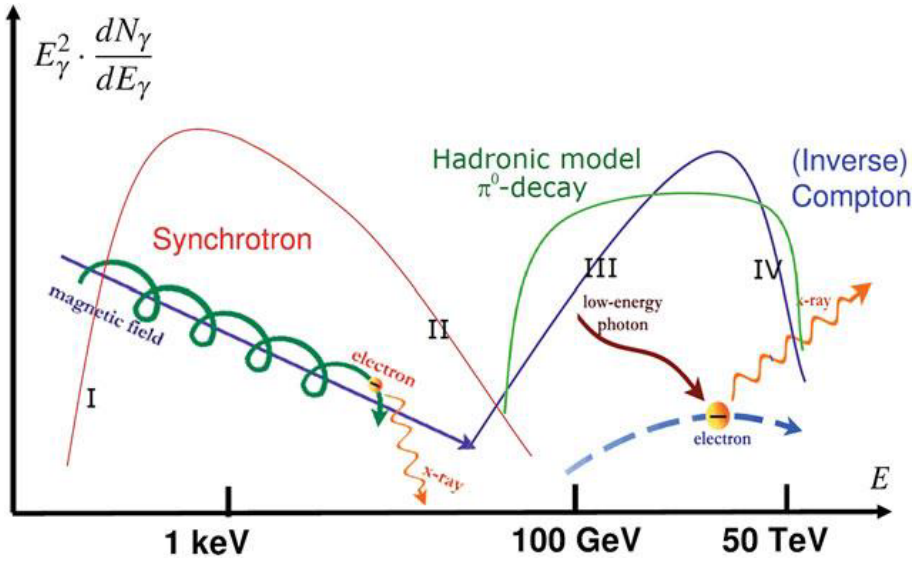

Figure 1.1: Spectral Energy Distribution (**SED**).

Hadronic processes

Gamma rays are also emitted through hadronic processes, such as inelastic hadronic interactions like proton-proton collisions, where one is usually a cosmic proton and the other is a proton or a nucleus of the Interstellar Matter (ISM): such interaction leads to the production of charged and neutral pions - together with other particles - and can take place in an environment rich of accelerated protons.

Photoproduction, i.e. the interaction of high-energy protons with low-energy photons, is another process that can lead to the production of gamma rays: it can occur close to the sources, where there is usually a high density of low-energy photons - radio, infrared, visible or UV photons.

As anticipated, both interactions produce mesons such as pions, which decay rapidly; in particular, neutral pions decay into two photons. Schematically, these processes can be described as

$$\begin{aligned} p + p &\rightarrow \pi + p + ... \\ p + \gamma &\rightarrow \pi_0 + p \\ \pi_0 &\rightarrow \gamma + \gamma \end{aligned}$$

The decay of neutral pions generates the so-called "pion bump" in the Spectral Energy Distribution (SED) shown in Figure 1.1. The observed photons resulting from π_0-decay can have energies in the VHE γ-ray regime, especially in regions of dense gas, where there is a high abundance of Interstellar Matter hadrons and relativistic protons.

Charged pions, on the other hand, will decay via

$$\begin{aligned} \pi^+ &\rightarrow \mu^+ + \nu_\mu \rightarrow e^+ + \overline{\nu_\mu} + \nu_e + \nu_\mu \\ \pi^- &\rightarrow \mu^- + \overline{\nu_\mu} \rightarrow e^- + \overline{\nu_e} + \overline{\nu_\mu} + \nu_\mu \end{aligned}$$

This is very important, because the detection from a source of the neutrinos generated in these decays would be incontrovertible evidence that hadronic processes are taking place in such cosmic environment, meaning that the accelerated particles are indeed hadrons and not leptons.

Other processes

All the processes described so far rely on the Standard Model (SM) description of fundamental physics. There are, however, other theories beyond the SM that include particles which can decay in photons: gamma rays can then be excellent probes for "New Physics". For example, considering the question of dark matter, cosmological observations place several constraints on the type of particle that can explain dark matter, and many candidates have been proposed in recent decades.

Among them are the Weakly Interacting Massive Particles (WIMPs), which are candidates for Cold Dark Matter (CDM), i.e. they must have decoupled from the primordial plasma while being non relativistic.

Such particles, if present in our Universe, could annihilate in pairs of particles such as

$$\chi\chi \;\rightarrow\; b\bar{b},\; \tau^+\tau^-,\; W^+W^-,\; \mu^+\mu^-,\; q\bar{q},\; ZZ,\; ...\; \rightarrow\; \gamma\gamma$$

as pictured in Figure 1.2.

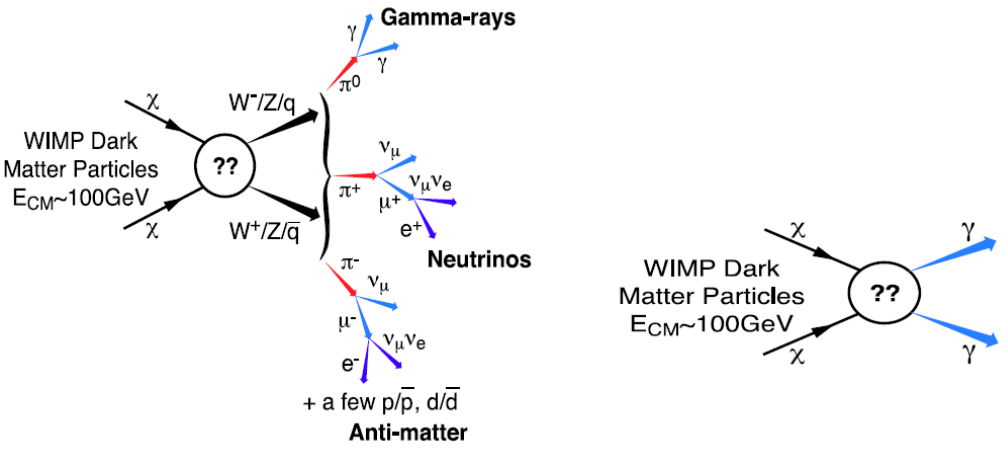

Figure 1.2: Possible channels of WIMP annihilation with the gamma-ray production [2].

1.1.1 Cosmic and gamma rays sources

An essential constraint for the acceleration of cosmic rays was given by A.M. Hillas in 1984 and states that the maximum energy an accelerated charged particle can reach in a given source depends on the source's characteristics, such as its size and magnetic field. The Hillas condition is given by

$$E_{max} = 3eZB\beta_s R_s$$

where eZ is the particle's electric charge, β_s is the velocity of the shock wave and B and R_s are the magnetic field and radius of the source. Such condition can be pictured in the homonymous plot - Figure 1.3, that displays a variety of astrophysical objects of different sizes where particle acceleration could potentially take place. However, sites below the diagonal line fail to meet the Hillas condition for a 10^{20} eV proton, even with $\beta_s = 1$, while the dashed line refers to 10^{20} eV iron nuclei. Considering more reasonable plasma velocities (for example, within the range of $c > v > 1000\,km\,s^{-1}$), the line will be positioned even higher: this means that only a limited number of sites remain as viable possibilities. These sites would either involve extremely compact objects with substantial magnetic fields or exceedingly large objects. In either scenario, achieving very high speeds becomes necessary [3].

Of course, this holds true for extreme energies such as $10^{20}\,eV$, while at lower energies the number of candidate sources increases.

Furthermore, in Figure 1.3 the Large Hadron Collider is also depicted: this highlights the necessity and importance of studying cosmic sources, since extreme energies can only be reached in astrophysical environments and are not currently reproducible by human-made facilities. Some examples of cosmic rays' sources are described in the following paragraphs.

Supernova remnants (SNRs)

Supernova remnants consist of the combination of ambient gas and expanding ejected material remaining after a supernova explosion, which takes place as the end of the life of stars with mass above 8 solar masses ($M_\odot$). It is believed that $\sim 1\%$ of the rest mass of the star is transferred to the ejected material, while $\sim 99\%$ is carried away by neutrinos. SNRs have been observed to contain shock fronts, very efficient particle accelerators able to reproduce the observed CR spectrum on Earth; another main argument for SNRs to be source candidates for Galactic cosmic rays results from global energetic considerations. The typical energy expected to be transferred from a supernova to the supernova remnant is $\simeq 10^{51}$ erg, which results in an expected power of Galactic SNRs of

$$P_{SNR} = \frac{E_{SNR}}{\Delta t_{SNR}} \simeq 10^{42}\ \text{erg/s}$$

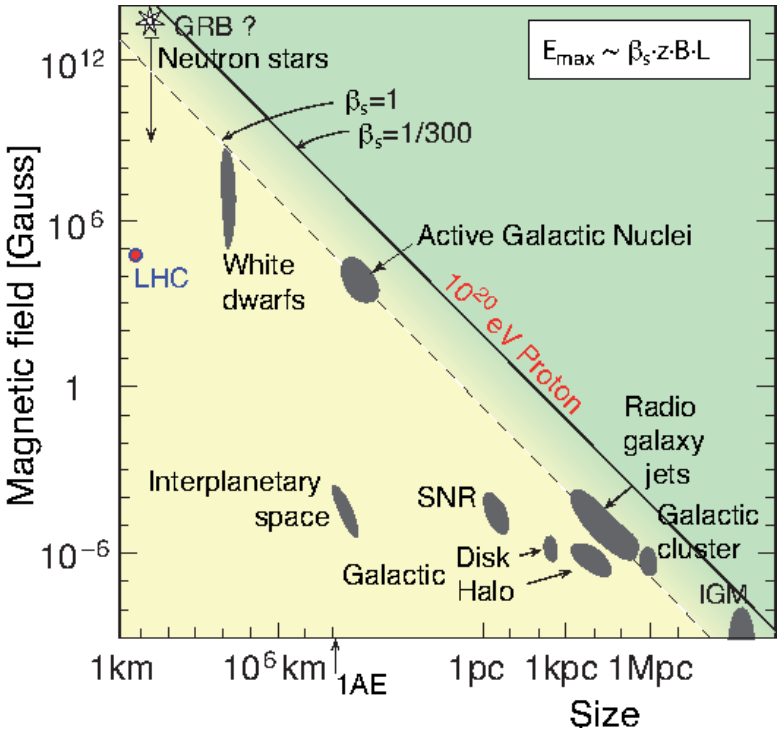

Figure 1.3: Hillas plot: Hillas condition showing the size and magnetic field strength of astronomical objects acting as possible sites for particle acceleration [3].

Also, the required power to reproduce the observed Galactic Cosmic Rays energy density, which is equal to $\omega_{GCR} \simeq 0.5$ eVcm^{-3}, is

$$P_{GCR} = \frac{\omega_{GCR} V_{galaxy}}{\tau_{GCR}} \simeq 10^{41} \text{ erg/s}$$

with $V_{galaxy} \simeq 5 \cdot 10^{67}$ cm^3, volume of our Galaxy, and $\tau_{GCR} \simeq 2 \cdot 10^7$ yrs, the typical time cosmic rays remain in our Galaxy.

Hence, SNRs can be able to accelerate Galactic Cosmic Rays if at least $\simeq 10\%$ of their energy if transferred to Cosmic Rays.

Indeed, observations in High and Very High Energy γ-rays confirmed the acceleration of cosmic rays in SNRs.

Neutron stars, Pulsars and Pulsar Wind Nebulae

Neutron stars are compact, highly magnetized, rapidly spinning objects that originate from the core of a massive star as it exhausts its nuclear fuel and undergoes a gravitational collapse, while its outer layers undergo a supernova explosion. As a result of angular momentum conservation during the collapse, the neutron star ends up spinning at very high speeds, with periods P between 0.01 s and 1 s.

Such objects have masses $\simeq M_\odot$, radii of a few tens of kilometres, very high densities ($\simeq 10^{14}$ gcm^{-3}) and intense magnetic fields of the order of $10^8 \div 10^{15}$ G [4].

In 1967, neutron stars were given the name "pulsars" after they were discovered to emit radiation pulses in the radio spectrum [5].

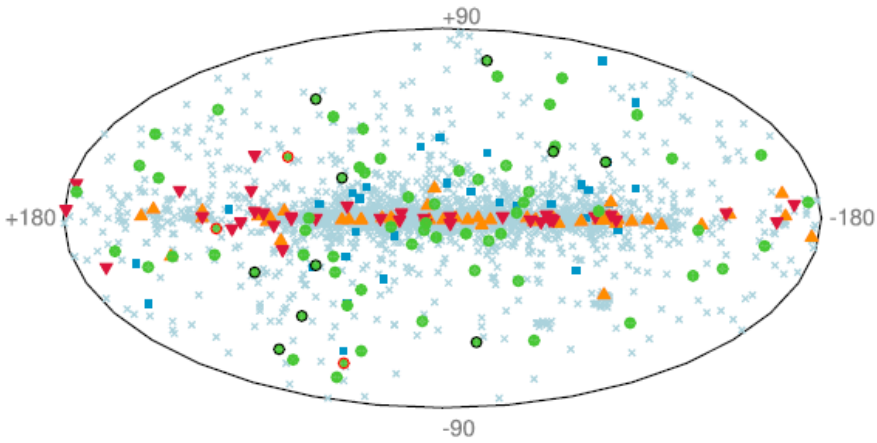

Figure 1.4: Position in Galactic coordinates of some radio and γ-ray pulsars, with radio- and γ-loud young pulsars shown as orange upward triangles, radio-faint and γ-loud young pulsars denoted as red downward triangles, and radio- γ-loud millisecond pulsars shown as green filled circles. Blue squares highlight the radio pulsars that have been recently discovered in the direction of Fermi-LAT point sources. From [4].

Subsequently, in 1969 and the early 1970s, these pulsars were found to emit pulses also in the optical, X-ray, and γ-ray wavelengths [6–9].

The short pulses of constant frequency were quickly understood to be caused by rotating beams of light passing the Earth at the angular velocity of the star, denoted by $\Omega = 2\pi/P$: only dense stars like neutron stars could achieve such high rotation rates required to match the observed frequencies. The pulsed radiation is believed to originate from accelerated particles near the magnetic poles, if the magnetic and rotational axes are not aligned.

In addition, particles escaping from the vicinity of a pulsar as part of the supersonic pulsar wind may form a wind termination shock in the surrounding region: here they can undergo diffusive shock acceleration, with an energy gain at each shock crossing. This results in a Pulsar Wind Nebulae with very energetic particles, mostly electrons, that can here undergo energy losses via synchrotron processes.

Pulsar wind nebulae are then expansive sources of non-thermal emission, visible across radio, X-ray, and γ-ray wavelengths, which often surround pulsars. These nebulae indicate the presence of a magnetized wind containing relativistic particles, carrying away most of the pulsar's rotational energy. It is not yet clear how the pulsar's energy is distributed between magnetic dipole radiation and relativistic particles.

Gamma Ray Bursts (GRBs)

Cosmic gamma-ray bursts (GRBs) are highly intense emissions of gamma radiation that last from fractions of a second (short GRBs, < 2 s) to several minutes (long GRBs, > 2 s); these bursts release the majority of their energy in the γ-ray spectrum (above ~ 0.1 MeV).

They are *transient* events, since they occur unpredictably - so unpredictably that they were discovered accidentally by the American military series of satellites VEGA, designed to monitor the nuclear test ban treaty of 1963; since then, there have been several GRBs'

detection both by satellite experiments - by FERMI-GBM, for example - and by ground-based observatories like MAGIC [10, 11]

GRBs are quite peculiar astrophysical events: a GRB explosion can be as luminous as objects near us, such as the Crab nebula, although it is very distant. For example, GRB 050904 observed by the Swift satellite, launched in 2004, has a redshift z = 6.295 [12].

The typical amount of energy released by a GRB ranges from 10^{44} to 10^{47} J (10^{51} to 10^{54} erg), which must, however, be corrected by a factor $\Omega/4\pi$, which takes into account the fact that emission is collimated in a solid angle Ω. Then, the energy radiated in gamma rays is always close to 10^{44} J (10^{51} erg). Given the time scales involved, the size of the source must be very small: it cannot exceed the distance radiation can travel in the same time interval, i.e. at most a few hundred kilometers. Energy must have been ejected in an ultra-relativistic flow which converted its kinetic energy into radiation away from the source.

A fundamental question is the nature of such energetic events: the enormous energies involved greatly restrict the number of possibilities. Only the merging of the components of evolved binary systems with compact objects (neutron stars or black holes), or the collapse of the most massive stars at the ends of their lifetimes (described in the "hypernova" and "collapsar" models), appear to meet the gigantic energy requirements. Recent detections of iron-line emission at X-ray wavelengths in GRB afterglows favors the latter class of models, because the quantity of iron estimated from such observations seems most likely to have originated in an evolved massive star that exploded in a supernova-like event [13, 14].

1.2 Detecting γ-rays

Gamma Rays can be detected in space, thanks to satellite experiments, and on Earth's surface with ground experiments; then the detection is called *direct* in the first case and *indirect* in the latter. Both methods are important in order to survey the sky over a wide range of γ-ray energies and their efficiency is defined by the cosmic photons' flux, which determines the effective area of an experiment and therefore its dimensions and feasibility. In the following paragraphs, both methods are described, together with their perks and limits.

1.2.1 Direct detection

Direct detection is best suited for γ-rays in the lower energy range: these observations are carried out by satellites that host proper detectors. The interaction of photons with matter is dominated by different processes, depending on the energy of the photons themselves: therefore, different detection techniques are needed.

However, at energies over $\approx$ GeV the predominant process is pair production.

FERMI-LAT

One of the latest satellite experiments that would be worth mentioning is surely the FERMI Large Area Telescope (LAT), sensitive to gamma rays in the range $20\,\text{MeV} \leq E_\gamma \leq 300\,\text{GeV}$; FERMI is also equipped with the Gamma-Ray Burst Monitor (GBM), specialized for gamma-ray bursts studies in the energy range between 8 keV to 40 MeV.

The operating principle of FERMI-LAT is the following: an incoming γ-ray reaches a precision converter-tracker: here it interacts with an atom in one of the thin tungsten foils, producing an electron-positron pair. These charged particles are detected and tracked by a x-y array of silicon strips, and finally are stopped by a cesium iodide calorimeter, which measures the total energy deposited. A plastic anticoincidence detector surrounds the whole LAT: here the photon will produce no signal, but a charged cosmic ray will. Since charged cosmic rays outnumber gamma rays by a factor of $10^2 \div 10^5$, they would represent a potentially overwhelming background that can be rejected by the use of this anticoincidence detector. The telescope's field of view is very wide, about 60°.

Fermi-LAT has successfully identified thousands of γ-ray sources both within our galaxy and in distant regions of the universe: a lot of these sources are active galactic nuclei.

Furthermore, Fermi-LAT has detected over 200 pulsars within our galaxy, contributing to our understanding of these objects. These observations are contained, together with a lot more of them, in the *Fourth Fermi Large Area Telescope Source Catalog (4FGL)* (May 2019): specifically, such catalogue contains, for each source, the spectral energy distributions over eight years and the light curves at one-year intervals.

The 4FGL comprises 5065 sources with a significance of 4σ, providing their localization and spectral properties:

- 75 sources are explicitly modeled with spatial extension.

- 355 sources are classified as identified based on angular extension, periodicity, or correlated variations observed at other wavelengths.
- For 1323 sources, no plausible counterpart or association has been found at other wavelengths.
- Over 3130 of the identified or associated sources are active galaxies of the blazar class, specifically active galactic nuclei with two jets emanating from the galaxy's core, where both jets are directed towards the Earth. On the other hand, 239 sources are pulsars.

Out of the 5065 LAT sources included in the 4FGL, 1323 sources ($\sim 30\%$) are not associated with any known counterparts; moreover, 92 sources are classified as "unknown" and other 90 sources are classified as "Source Position Prioritization" (SPP), meaning they are of unknown nature but overlap with known Supernova Remnants (SNR) or Pulsar Wind Nebulae (PWN), making them candidates for these classes. These unknown and SPP sources collectively represent 4% of the total. The fraction of associated sources is lower for faint sources, primarily due to larger errors in their regions of detection. Conversely, all bright sources are successfully associated with known counterparts. A detailed and astonishing map from the Catalogue is shown in Figure 1.5.

Moreover, Fermi-LAT has yielded surprising discoveries, one of which is the γ-ray emission originating from *novae*: novae are astronomical events that occur in binary star systems, consisting of a white dwarf and a companion star, usually a main-sequence star or a red giant. During a nova event, the white dwarf accretes material from its companion star, building up a layer of hydrogen-rich material on its surface; when enough material accumulates, a thermonuclear explosion occurs on the surface of the white dwarf, causing a sudden and dramatic increase in brightness. This explosion ejects the accumulated material into space, leading to the emission of intense light across various wavelengths, including optical, X and γ: specifically, these γ-rays are produced through the already described interactions between accelerated particles, such as protons and electrons, with the surrounding material during the nova explosion.

The detection of γ-rays from novae has provided valuable insights into the acceleration of particles and the dynamics of the nova explosion: indeed, such gamma-ray emission indicates the presence of relativistic particles and the existence of strong magnetic fields, which are involved in the acceleration and transport of these particles.

Furthermore, Fermi-LAT precisely measured the diffuse γ-ray emission, which arises from the interactions between Galactic cosmic rays and interstellar gas and radiation fields. Such observations have led to unexpected findings, including the detection of vast bubbles above and below the Galactic center and an excess of γ-ray emission near the Galactic center itself. Measures by Fermi-LAT are consistent with the hypothesis that cosmic rays fill the entire galaxy.

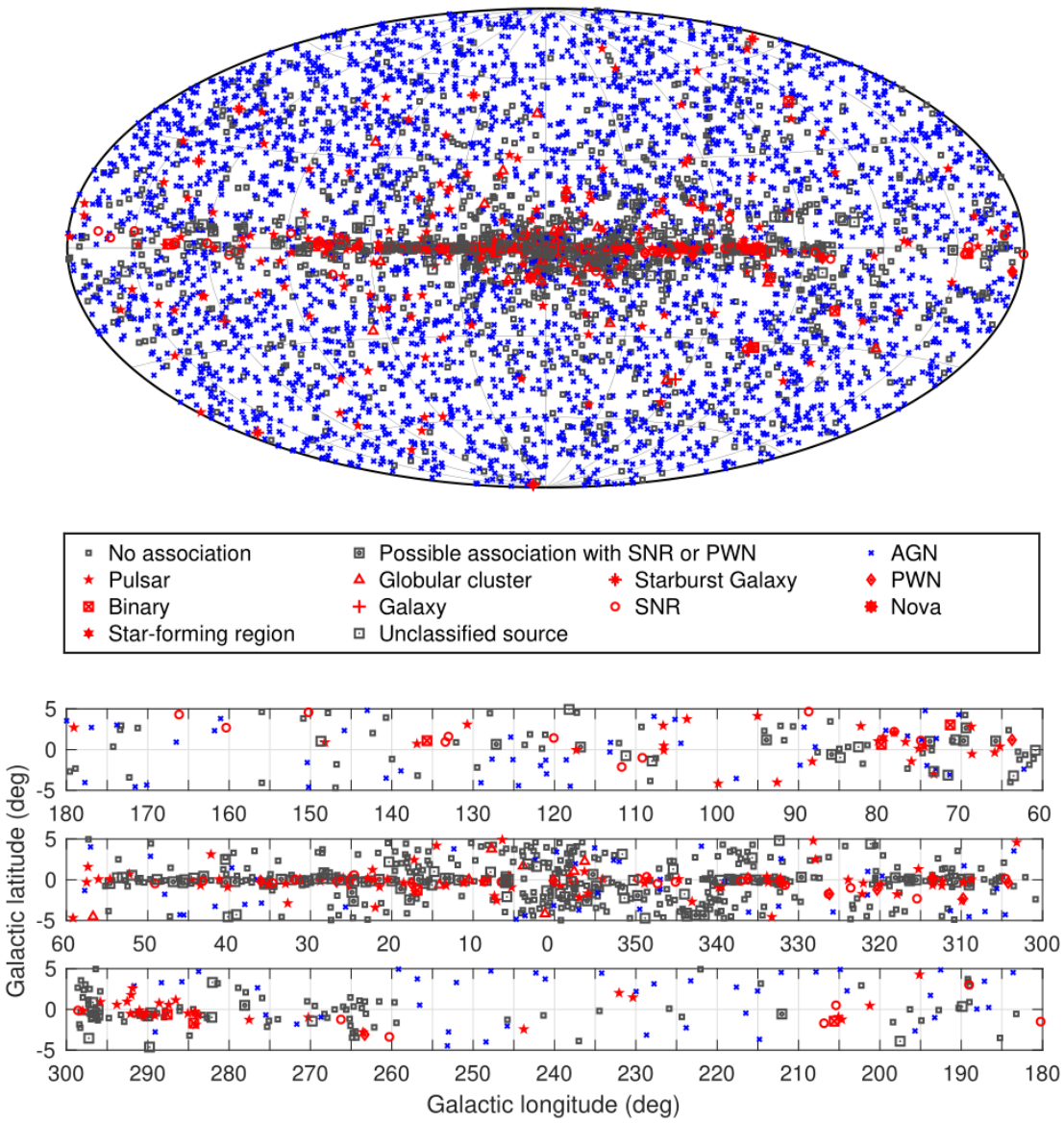

Figure 1.5: Full-sky map (top), and map of the Galactic plane divided into three longitude bands (bottom). The sources are categorized by their source class; no differentiation is made between associations and identifications. Active Galactic Nuclei of all classes are represented using the same blue symbol, while the other sources that are confidently associated with a well-defined class are shown in red. Un-associated sources and those associated with counterparts of unknown nature are depicted in black [15].

Limits of space-based detection As the gamma-ray energy increases, the flux decreases, making a satellite detector less efficient, since a bigger effective area is required to achieve reasonable statistics and observational timescales; furthermore, higher energy particles require bigger detectors in order to be able to lose a sufficient amount of energy for detection. Therefore, a small detector becomes less and less suited for observations: for γ-ray energies above $\approx 10\,\mathrm{GeV}$, gamma-ray astronomy is best performed with ground-based facilities, i.e. through *indirect* detection.

1.2.2 Indirect detection

Ground-based experiments aim to detect γ-rays by studying the air showers induced by them in the atmosphere: an energetic gamma ray, in fact, will interact with the atmosphere producing an electromagnetic shower made of positrons, electrons and photons. Such shower develops thanks to two phenomena: e^+e^- pair production and Bremsstrahlung. Electrons and positrons of the shower are very energetic and they may emit Cherenkov radiation if they travel faster than the light in the medium. This radiation can be detected on ground by proper telescopes, called Imaging Atmospheric Cherenkov Telescopes (IACT), which will be extensively described in chapter 2.

Alternatively, it is possible to directly detect the electrons and positrons of the cascade. There are two techniques most commonly used for this purpose: Resistive Plate Chambers and Water Cherenkov detectors.

ARGO-YBJ

The *Astrophysical Radiation with Ground-based Observatory* experiment is a main example of the first method: it was located at the Yangbajing Cosmic Ray Laboratory in Tibet, China, at an altitude of 4300 m above sea level. Its detector consisted of a large array of Resistive Plate Chambers (RPCs) covering a total area of about $11\,200\,\mathrm{m}^2$.

ARGO-YBJ has provided detailed measurements of the energy spectrum of cosmic rays in the TeV energy range; it has also detected and identified several γ-ray sources in the sky and has been involved in the detection and study of γ-rays from solar flares and other solar events. Its observations have indeed covered several important physical topics, ranging from very high energy γ-ray astronomy to cosmic-rays and helio-physics.

HAWC

The *High-Altitude Water Cherenkov Gamma-Ray Observatory* is a major example of the Water Cherenkov Detection technique: it consists of an array of large water Cherenkov detectors sensitive to gamma rays and hadrons in the 100 GeV - 100 TeV energy range. It is built at 4100 m above sea level on the northern slope of the volcano Sierra Negra, Mexico.

When a charged particle enters the detector, it emits Cherenkov light if it's sufficiently energetic; this light is collected by photomultiplier tubes, which convert it into an electrical signal.

HAWC has detected, identified and contributed to the study of numerous γ-ray sources, including active galactic nuclei, pulsar wind nebulae and supernova remnants. Moreover, HAWC has been used to search for γ-ray signals that could potentially originate from dark matter annihilation or decay: while no conclusive dark matter signal has been identified, HAWC's sensitivity has been valuable in placing constraints on certain dark matter models. Furthermore, HAWC has mapped the diffuse γ-ray emission in the sky as well and has also conducted detailed surveys of the Galactic plane, revealing numerous γ-ray sources and regions of interest for further study. The observatory's observations have been combined with data from other telescopes and instruments, such as Fermi-LAT and VERITAS, to conduct multi-wavelength studies of γ-ray sources and cosmic ray phenomena.

LHAASO

Among the wide-field of view facilities, the *Large High Altitude Air Shower Observatory* has distinguished itself in the latest years: it is located at 4410 m above sea level at Mount Haizi, China, and is designed to detect air showers induced both by γ-rays and by cosmic rays with energy ranging from a few tens of GeVs to a few EeVs.

One of the most astonishing results from this young observatory is certainly the observation of 12 candidate PeV sources, since they showed γ-rays above TeV energies and an event above PeV; for this reason they are expected to be the first candidate"PeVatrons", i.e. sources that can accelerate particles to an energy of at least 1 PeV (10^{15} eV) and emit the observed photons during interactions with surrounding materials. Such PeVatrons are observed to be concentrated along the Galactic plane, with 11 out of the 12 having counterparts detected in the very-high-energy band, i.e. above 100 GeV. Moreover, the SEDs of the bright PeVatron sources among the 12 do not exhibit significant cut-offs around 100 TeV. This discovery has two important implications: firstly, it suggests that PeVatrons are widely distributed in our galaxy and secondly, it indicates that the supposed limit on particle acceleration capability around 1 PeV for the Galactic accelerators may not be real [16].

SWGO

Nowadays, a wide-field of view observatory in the southern hemisphere is under development, the *Southern Wide-Field Gamma-Ray Observatory*: it will have a design very similar to HAWC and it will be the only wide-field of view observatory sensitive to the southern sky. For this reason it would represent a valuable instrument in the gamma-ray astronomy. SWGO would allow to deeply study the Galactic Center and give access to the full sky for transient phenomena, fundamental also for providing follow-up alerts to IACTs.

Chapter 2

The IACT technique and the CTA Observatory

2.1 IACTs

As previously described, γ-ray astronomy can be carried out using both direct - on satellite - and indirect - ground-based - methods: the latter are more convenient when observations at higher energies are required. One of the suitable techniques is the Imaging Atmospheric Cherenkov Telescopes (IACT) one. This method exploits that fact that very high energy photons - such as γ-rays - will interact with the atmosphere, generating a so-called *electromagnetic shower*, i.e. a particle shower containing photons, electrons and positrons. Such particles, being way faster than light in the atmosphere, will emit the so-called *Cherenkov light*: it is indeed this light that the IACTs aim to detect.

In the following paragraphs the main involved physical phenomena will be briefly described.

2.1.1 Air showers

When a primary particle enters the atmosphere, it may interact with a nucleus and give origin to an extensive particle cascade. Depending on the primary particle, which can be a charged cosmic ray or a gamma ray, different air showers can occur, since the processes that take place are, indeed, different from particle to particle.

Air showers can be divided into electromagnetic and hadronic showers; their development is schematised in Figure 2.1.

Electromagnetic showers Electromagnetic showers are initiated by a high-energy gamma ray or by a positron or electron interacting with the atmosphere. The propagation and extinction of this cascade follow the same evolution, since the processes involved are the same.

Such processes are

- e^+e^- pair production, starting from a photon of energy $E_\gamma > 2m_ec^2 = 1.022\,\mathrm{MeV}$

- Bremsstrahlung, which is the radiation emitted by a charged particle (here an electron or a positron) that decelerates due to the interaction with a nucleus in the atmosphere

Essentially, a primary high-energy gamma ray of energy E_0 will interact with the atmosphere, generating an electron-positron pair: each of the latter will generate a gamma ray via Bremsstrahlung, which will again undergo pair production, and so on, until the energy of the particles involved decreases below the threshold required by the processes. Such limit is called critical energy E_C and corresponds to the energy value below which electrons and positrons will lose their energy via ionization rather then Bremsstrahlung ($E_c^e = 85\,\text{MeV}$ in air).

The development of an electromagnetic shower can be described by the Heitler model, which assumes that the energy is distributed equally among the produced particles at each interaction; also, one can assume that the radiation lengths λ_T for pair production and Bremsstrahlung are the same and have a value in air of $\lambda_T \simeq 37\ \text{gcm}^{-2}$. Energy loss by Bremsstrahlung follows an exponential decay, therefore the average distance between two interactions is evaluated as

$$e^{-\frac{d}{\lambda_T}} = \frac{1}{2} \quad \Rightarrow \quad -\frac{d}{\lambda_T} = \ln\left(\frac{1}{2}\right) \quad \Rightarrow \quad \frac{d}{\lambda_T} = \ln 2$$

So

$$d = \lambda_T \ln 2$$

The shower will have, after n interaction, 2^n particles, each with an energy of $E_0/2^n$. In the Heitler model one can also define the maximum size of the shower, when all particles have an energy corresponding to the critical one, as

$$E_0 = E_c^e N_{max} \quad \Rightarrow \quad N_{max} = \frac{E_0}{E_c^e}$$

Defining as n_{max} the steps after which the shower is constituted of N_{max} particles, one finds

$$N_{max} = 2^{n_{max}} = \frac{E_0}{E_c^e}$$

and then

$$n_{max} = \frac{\ln\left(\frac{E_0}{E_c^e}\right)}{\ln 2}$$

Then one can define the total shower propagation as

$$X_{max} = n_{max} \cdot d = \frac{\ln\left(\frac{E_0}{E_c^e}\right)}{\ln 2} \cdot \lambda_T \ln 2 = \lambda_T \ln\left(\frac{E_0}{E_c^e}\right)$$

Although the Heitler model is quite straightforward, it provides a reasonably accurate description of the shower development. However, the model tends to underestimate the photon-to-electron ratio, as it predicts an excessive number of $e^{\pm}$ particles. One factor con-

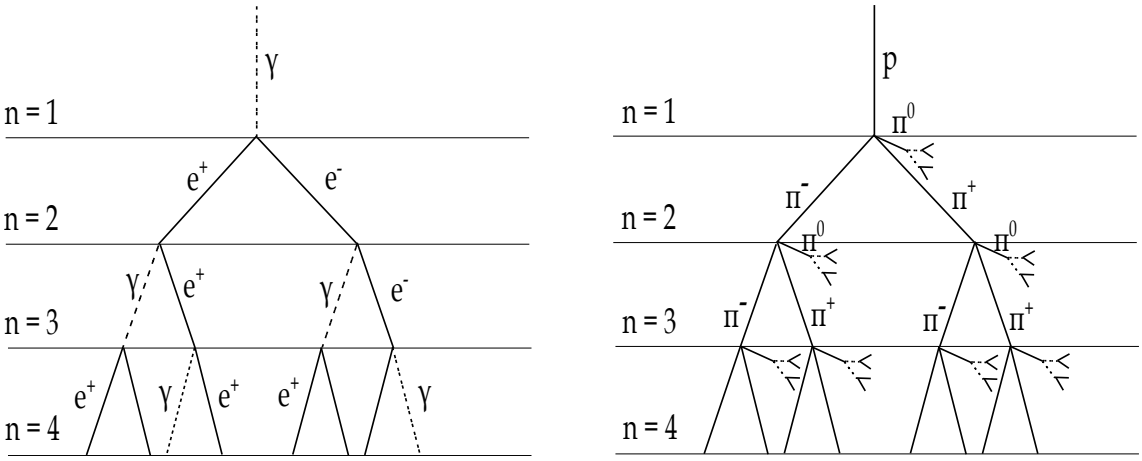

Figure 2.1: Schematics of the development of electromagnetic (left) and hadronic (right) showers.

tributing to this discrepancy is the emission of multiple photons during Bremsstrahlung.

In addition, many electrons or positrons are absorbed by the air as the shower progresses, again leading to an overestimation of the number of $e^{\pm}$ with respect to photons.

In order to extract the number of electrons N_e from the overall size N given by the Heitler model, a correction factor g is adopted as follows

$$N_e = \frac{N}{g}$$

Which is of the order of magnitude of ~ 10 [17].

Hadronic showers Hadronic showers are initiated by a charged cosmic ray interacting with the atmosphere; such phenomena are more complicated to study and to describe than the electromagnetic case, because the interactions can be of different kinds - including, for example, the strong and weak forces - and the variety of particles involved is much greater.

Again, we can use the Heitler model as a first and simple description: here, when a primary charged cosmic ray - typically a proton or a nucleus - interacts with the atmosphere, it is most likely to produce light particles like pions, both charged $\pi^{\pm}$ and neutral π^0. The latter will decay almost immediately ($\tau_{\pi_0} = 8.5 \cdot 10^{-17}$ s) in photons

$$\pi^0 \rightarrow \gamma\gamma$$

which will generate an electromagnetic shower.

Charged pions will, on the other hand, interact with the atmosphere producing charged and neutral pions, until they reach a critical energy value E_C below which they will decay via

$$\pi^+ \rightarrow \mu^+\nu_\mu$$
$$\pi^- \rightarrow \mu^-\overline{\nu_\mu}$$

For simplicity, one can assume that the same number of positive, negative and neutral pions are produced, so that at each interaction one has N_{ch} charged pions and $1/2N_{ch}$ neutral ones; moreover, we can assume that the energy is equally distributed between such particles. Considering the interaction length of strongly interacting particles λ_I, assumed constant with a value of 120 gcm^{-2}, an interaction will take place every $d = \lambda_I \ln 2$. After n interactions the shower will have $(N_{ch})^n$ charged particles that carry an energy of $(2/3)^n E_0$, while the remainder will go into neutral pions, therefore in electromagnetic showers.

Hence, these secondary electromagnetic showers carry away approximately 1/3 of the initial energy, which is a non negligible amount.

Such showers will then develop as seen in the previous paragraph; on the other hand, after n interactions charged pions will carry an energy equal to

$$E_\pi = \frac{E_0}{\left(\frac{3}{2}N_{ch}\right)^n}$$

and the shower development will go on until $E_\pi < E_c^\pi$, i.e. after n_c interactions

$$n_c = \frac{\ln E_0/E_c^\pi}{\ln \frac{3}{2}N_{ch}}$$

When the individual pion energies fall below a critical energy E_c^π, it becomes more likely that a $\pi^\pm$ will decay rather than interact: here the shower has its maximum development and all of the primary particle's energy E_0 is shared between N_π pions and N_{max} electromagnetic particles; since the number of muons N_μ is equal to the number of pions, we can write

$$E_0 = E_c^e N_{max} + E_c^\pi N_\mu$$

and considering the correction factor g for electromagnetic showers, we have $N_e = N_{max}/g$ and

$$E_0 = E_c^e \frac{N_{max}}{g} + E_c^\pi N_\mu = g E_c^e \left[N_{max} + \frac{E_c^\pi}{g E_c^e} N_\mu \right]$$

The total energy can also be divided into an electromagnetic component and a hadronic one

$$E_0 = E_{em} + E_h = E_{em} + N_\mu E_c^\pi$$

Hence, the fraction of energy that goes into the electromagnetic counterpart is

$$\frac{E_{em}}{E_0} = \frac{E_0 - N_\mu E_c^\pi}{E_0}$$

which is, for example, about 72% with a primary energy $E_0 = 10^{14}$ eV and about 90% with $E_0 = 10^{17}$ eV, evaluated with the approximation of simply adding up all the EM subshowers from each interaction to determine the total number of electrons produced [17]. One can also define another important quantity that contributes to the shower description, which is the atmospheric depth at which electrons and photons reach their maximum

number, X_{max}: in order to estimate it, one should consider all the electromagnetic sub-showers that will compose the hadronic cascade. As an approximation, one can consider only the electromagnetic showers initiated at the first interaction, which occurs at an atmospheric depth of $X_0 = \lambda_I \ln 2$: then, $2 \cdot 1/2N_{ch} = N_{ch}$ photons are produced and each one will initiate a cascade of energy $E_0/(3N_{ch})$. The depth of the shower maximum, starting at X_0, will then be

$$X_0^p = X_0 + \lambda_T \ln\left(\frac{E_0}{3N_{ch}E_c^e}\right)$$

Models such as the Heitler one presented here are good descriptions that allow to simply understand the development of particle showers; nevertheless, Monte Carlo simulations are required in order to get a more complete description of such complex phenomena.

During their journey in the atmosphere, the particles of a shower can be capable of producing Cherenkov light through the homonymous effect, which is described in the following section.

2.1.2 The Cherenkov effect

Charged particles that are traveling in a medium can have a velocity that is bigger than the speed of light in that medium; when this occurs, radiation is emitted as a consequence. Such radiation is known as *Cherenkov light*, from the name of the physicist who first published a complete study of this phenomenon in 1934, Pavel Cherenkov.

The Cherenkov effect is, then, another mechanism through which particles can lose their energy, but is numerically of second-rate importance with respect to ionization or Bremsstrahlung. Cherenkov light has some peculiar and interesting properties: for example, it is *not* isotropic, i.e. it is emitted with a certain angle. As mentioned, it is emitted when

$$v > \frac{c}{n} \quad \Rightarrow \quad \beta c > \frac{c}{n} \quad \Rightarrow \quad \beta > \frac{1}{n} \tag{2.1}$$

where c is the speed of light in vacuum and n is the refractive index of the medium. Light is emitted in a cone with an angle of

$$\theta_C = \frac{1}{\beta n} \tag{2.2}$$

In order to better understand the origin of such peculiar effect, a brief physical description is presented in the following paragraph.

Physical origin of the Cherenkov effect As the charged particle moves through a medium, the molecules of the material around it polarize in response (Figure 2.2), i.e. the charged particle generates a time-varying electric field at each point while traveling through the material, which induces a time-varying electric dipole moment in the medium's molecules. Upon returning to their ground state, these molecules release the energy they received as photons, which will form the spherical wavefronts originating from the moving particle. When the velocity of the charged particle is lower than the speed of light in the medium, the polarization field around the particle is usually symmetric; consequently, the corresponding emitted wavefronts will not intersect or overlap, leading to no interference effects.

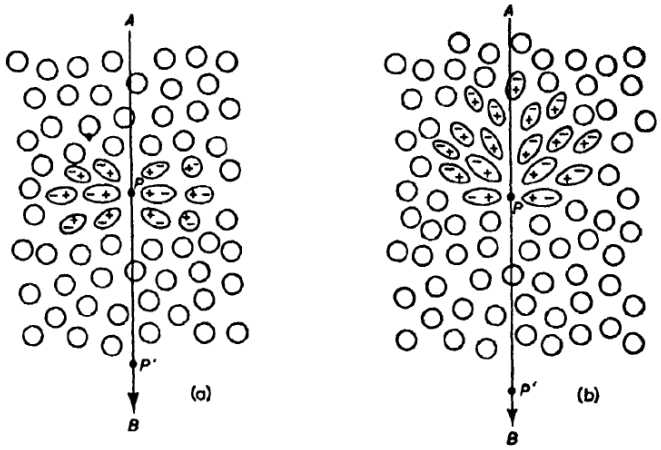

Figure 2.2: The polarization in a dielectric induced by the passage of a charged particle at low velocity (a) and at high velocity (b) [18].

In the opposite scenario, where the particle's velocity exceeds the speed of light in the medium, the polarization field becomes asymmetric along the direction of motion: as a result, the waveforms emitted by these polarized particles overlap and interfere constructively, creating a cone-like light signal observed at a characteristic angle known as Cherenkov light (Figure 2.3).

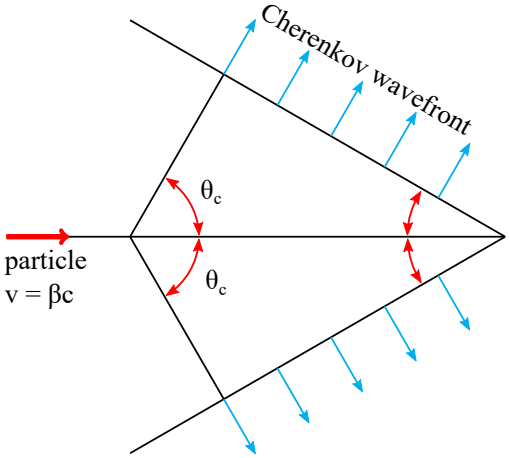

Figure 2.3: Cherenkov Light emitted by a charged particle traveling in a medium with velocity $v = \beta c$.

Energy spectrum and numerical distribution of the Cherenkov light The energy emitted as photons in a radiator of length L, having a frequency between ν and $\nu + d\nu$, is

$$\frac{dE}{d\nu} = \frac{2\pi\alpha Z^2 h}{c} L sin^2(\theta)\nu$$

where Z is the charge of the particle, $\alpha = e^2/4\pi\epsilon_0\hbar c$ and θ the Cherenkov angle. Keeping in mind that the energy of a photon is equal to $h\nu$, one can extract the number of photons emitted

$$\frac{dN}{d\nu} = \frac{1}{h\nu} \cdot \frac{dE}{d\nu} = \frac{2\pi\alpha z^2}{c} L sin^2(\theta)$$

which suggests that Cherenkov photons are equally probable in frequency. Although, as seen in equation 2.2, $\sin\theta$ depends on the β of the particle: particles with greater β will cause a larger emission.

As seen, the numerical distribution $dN/d\nu$ is constant: the same is not true for $dN/d\lambda$, in fact

$$c = \lambda\nu \;\Rightarrow\; d\nu = \frac{c}{\lambda^2} d\lambda$$

and

$$\frac{dN}{d\lambda} = \frac{dN}{d\nu} \cdot \frac{c}{\lambda^2} \;\Rightarrow\; \frac{dN}{d\lambda} \propto \frac{1}{\lambda^2}$$

More specifically, the number of emitted photons per unit length and wavelength is

$$\frac{d^2 N_{ph}}{dz d\lambda} = 2\pi^2 \frac{sin^2\theta_C}{\lambda^2} \;\propto\; \lambda^{-2}$$

and presents the most emission in the ultraviolet band.

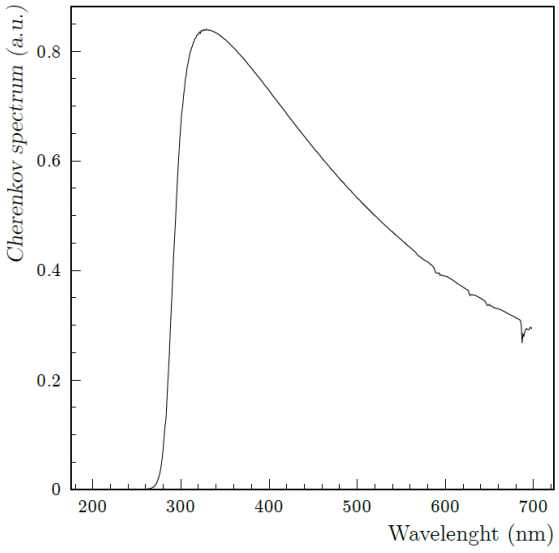

Figure 2.4: Typical spectrum of Cherenkov light generated by vertical TeV air showers at an altitude of 2200 m. From [19].

Although the Cherenkov effect can occur whenever the condition 2.1 is satisfied, here we are interested in the Cherenkov light emitted by the particles of an electromagnetic shower induced by a γ-ray in the atmosphere. Here the Cherenkov photons undergo absorption and scattering processes, in particular

- Absorption by the ozone, via

$$O^3 + \gamma \;\rightarrow\; O^2 + O$$

  which happens mostly near the UV band (λ from 200 to 300 nm)

- Rayleigh scattering, where photons scatter elastically on air particles that have much smaller sizes with respect to λ: the absorption length goes as $\Lambda_R \propto \lambda^4$
- Mie scattering, where photons scatter on particles with sizes comparable to λ, such as, for example, aerosol molecules. The absorption length goes linearly as $\Lambda_M \propto \lambda$
- Diffusion due to water vapour in clouds or air humidity.

The fraction of light arriving at ground level from a point at atmospheric depth x is given by

$$\tau_{atm} = e^{-\frac{(1020 - x)\sec\phi}{\Lambda}}$$

where ϕ is the zenithal angle and Λ the absorption length in gcm^{-2}.

Lateral distribution of Cherenkov photons As the air density varies with altitude, the refraction index also changes with altitude, making the Cherenkov angle increase during the shower propagation: for example, it goes from $\theta \simeq 0.2°$ at $z \sim 30$ km to $\theta \simeq 0.66°$ at $z \simeq 10\,\mathrm{km}$, to $\theta \simeq 0.74°$ at $z \simeq 8\,\mathrm{km}$, to $\theta \simeq 1.3°$ at sea level. There exists an empirical relation

$$\eta = n - 1 \approx \eta_0 e^{-\frac{z}{h_0}}$$

where $\eta_0 = 2.9 \cdot 10^{-4}$ and $h_0 = 7250\,\mathrm{m}$. The variation of the Cherenkov angle with altitude almost precisely compensates for the effect of the changing distance from the Earth, which leads to the formation of a light ring at a distance of $\sim 150\,\mathrm{m}$ from the core of the shower. In other words, Cherenkov light emitted at higher altitudes is highly collimated, while the one emitted at lower altitudes is more spread out over a larger angle. At sea level, this results in an accumulation of light at a distance of approximately 120 to 150 meters from the shower axis. The light is thus collimated in a so-called Cherenkov Pool while it reaches the ground (Figure 2.5).

Consequently, the lateral distribution of light peaks at such distance and then rapidly decreases for greater distances, as shown in Figure 2.6.

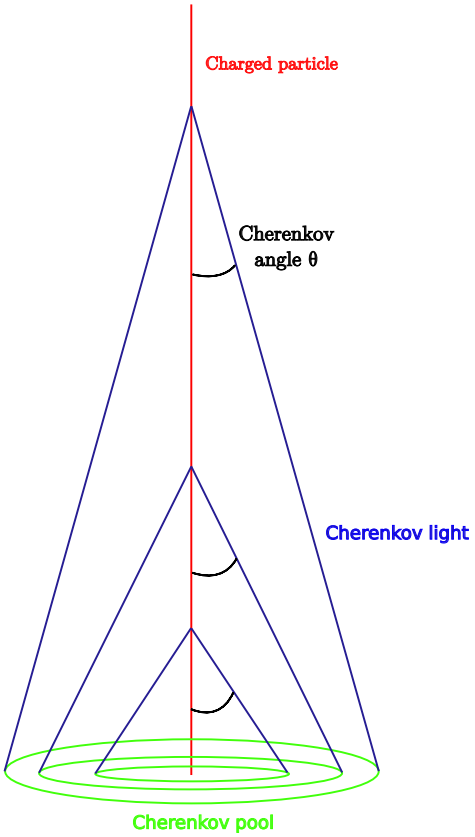

Figure 2.5: Cherenkov pool.

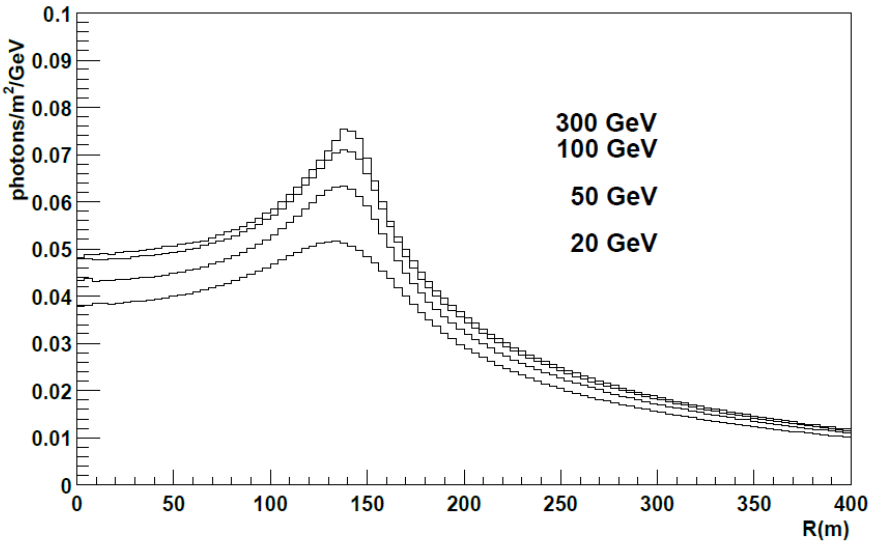

Figure 2.6: Lateral distribution of Cherenkov photons.

Cherenkov photons time distribution Cherenkov photons reach the Earth at different times, spreading out over a certain time interval. Near the shower axis, photons emitted at lower altitudes reach the detector before those emitted at higher altitudes. However, at larger impact distances, photons emitted lower in the atmosphere follow a longer geometric trajectory compared to photons emitted higher up. As a result, the lower-emitted photons reach the detector after the higher-emitted ones. At a distance of approximately 120 m from the shower, the two effects almost completely compensate each other, resulting in most of the Cherenkov light arriving at ground within few ns; the shower duration can extend up to 5 ns at the shower axis and significantly increase for impact distances > 200 m, as represented in Figure 2.7.

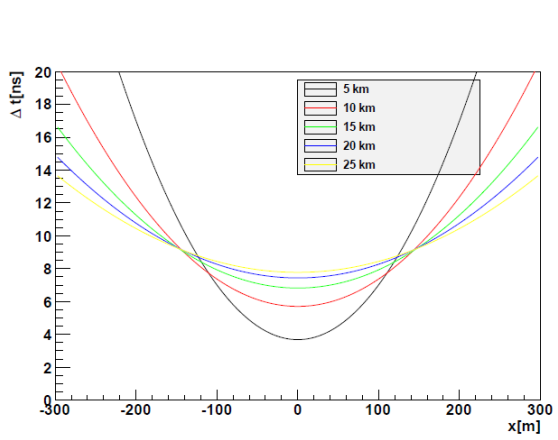

(a) Time of arrival of photons as a function of the distance from the shower axis, depending on the altitude at which they are emitted.

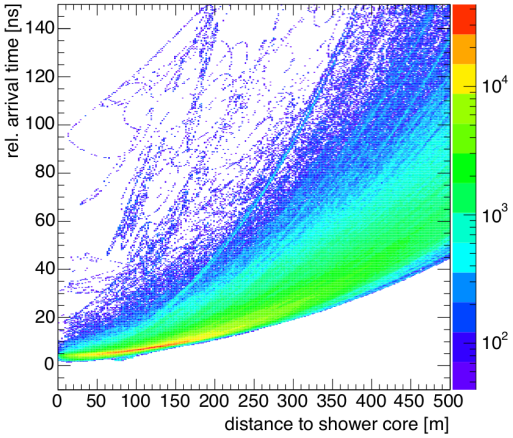

(b) Time distribution of Cherenkov photons for a 1 TeV vertical γ-ray induced air shower. Most of the photons arrives within $\simeq 10$ ns.

Figure 2.7: Cherenkov photons' time characteristics.

Gamma-hadron separation In order to select a sample of events generated by γ-rays, it is essential to distinguish and eliminate hadronic shower events. Analyzing primary particles with identical energy, it becomes evident that hadrons produce significantly less Cherenkov light - approximately one third - compared to γ-rays. Additionally, γ-ray induced showers exhibit reduced fluctuations and display a more uniform and compact distribution in both space and time. Conversely, the Cherenkov pools created by primary protons or other hadronic particles are marked by clusters, mainly caused by their secondary electromagnetic showers. An example of such differences is shown in Figure 2.8.

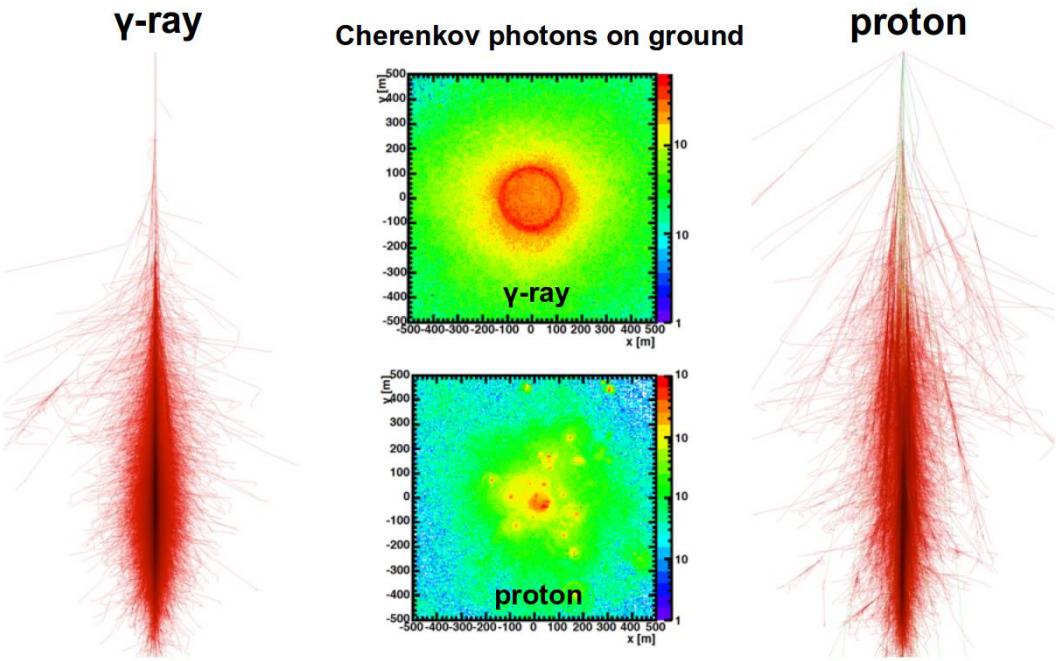

Figure 2.8: Difference between Cherenkov emission from a γ-induced and a proton-induced shower.

2.1.3 The Imaging Atmospheric Cherenkov Telescopes

The Earth's atmosphere is not transparent for the whole electromagnetic spectrum: indeed, it is opaque to most of wavelengths, being transparent only for two windows: the visible and the radio regime, as shown in Figure 2.9.

The absorption of X-rays and γ-rays by the atmosphere precludes the possibility for direct detection of cosmic γ-rays with ground-based experiments. However, as was already mentioned, it is always possible to use balloons or satellites with suitable detectors in order to perform a direct observation. The Imaging Atmospheric Cherenkov Telescope technique works with ground-based observatories and allows indirect detection.

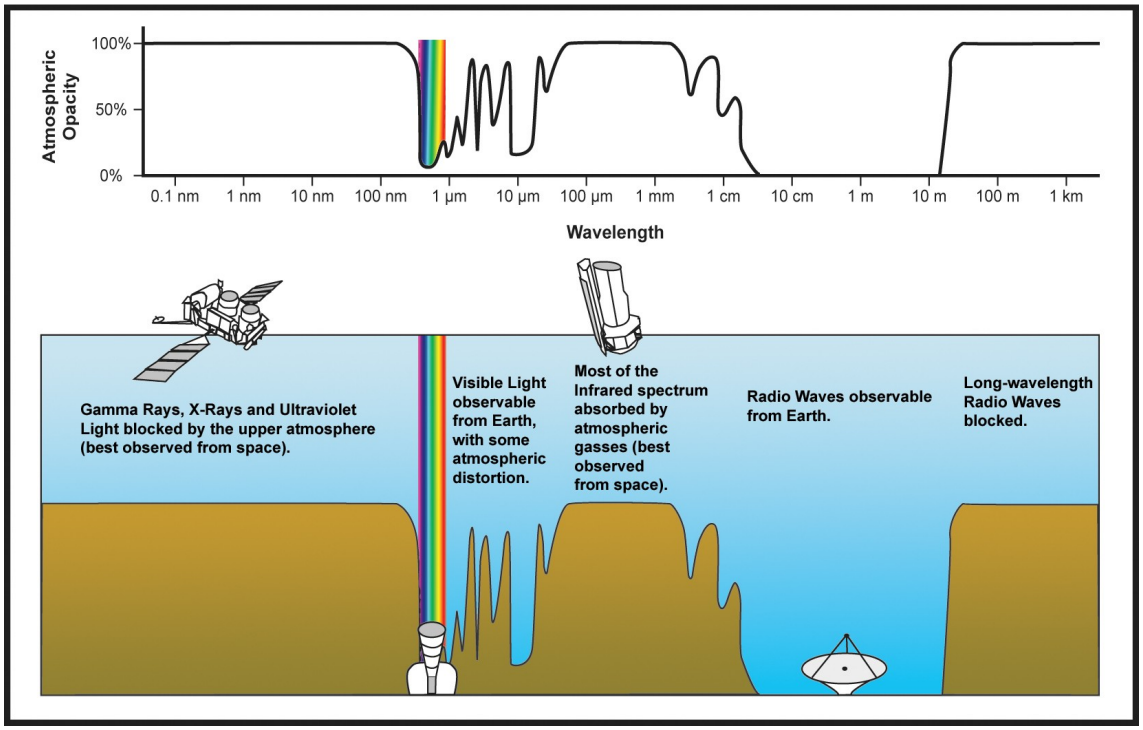

Figure 2.9: Opacity of the atmosphere for different wavelengths and suitable methods of detection [20].

Working principle

As anticipated at the beginning of chapter 2, such telescopes aim to detect the Cherenkov light emitted by the particles of γ-ray induced electromagnetic showers: to do so, they are equipped with a mirror - single or segmented - that reflects and focuses such light on a camera. A schema of this method of detection is pictured in Figure 2.10.

The atmospheric Cherenkov light yield exhibits a significant dependence on the primary energy, with, for example, $2\,\text{photons}\,\text{m}^{-2}$ in the shower core for an EAS generated by a 100 GeV γ-ray compared to $600\,\text{photons}\,\text{m}^{-2}$ for a 10 TeV γ-ray [22]; this leads to the usage of larger dishes for lower VHE γ-ray observations, typically ranging from tens to hundreds of GeV, which are mostly from extragalactic sources. On the other hand, when observing VHE γ-rays in the TeV-regime, mainly from Galactic sources, the use of smaller dishes is adequate. Since Cherenkov photons originate from various heights within an

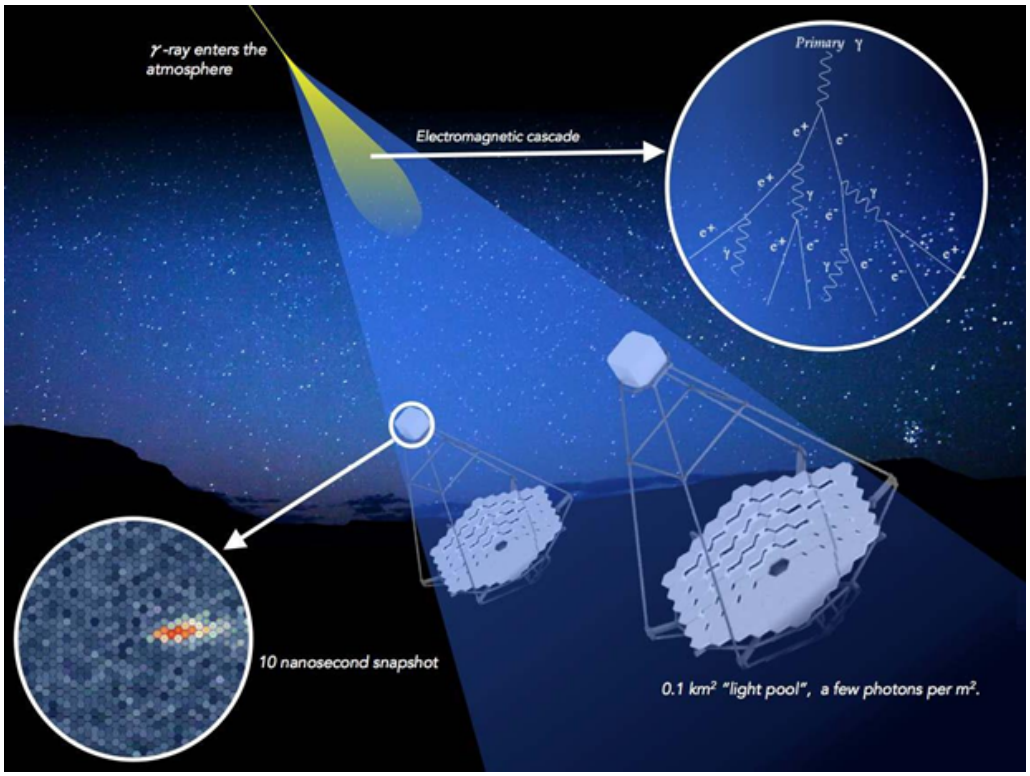

Figure 2.10: The IACT technique [21].

Extensive **A**ir **S**hower (EAS), they are emitted with different angles, causing them to hit the mirror at different incident angles, consequently hitting different positions or pixels in the camera: hence, the image in the Cherenkov camera reflects the specific characteristics of the shower. The resulting geometry of a γ-induced event forms an elliptical - or comet-like - shape, with the head pointing towards the source. The length of the observed ellipse is influenced by both the inclination of the EAS relative to the telescope pointing and the distance of the shower core from the telescope, also known as the *impact distance*. The angular size of the image spans from 1° to 5° and the total number of detected photons for an event typically falls between 10^2 and 10^5, while the signal duration lasts from 5 to 100 ns. Conversely, the recorded image of a hadron-induced event presents a more irregular pattern due to the presence of sub-showers, reflecting the characteristics already described through Figure 2.8 and shown also in Figure 2.11.

Typically, telescopes work simultaneously and perform *stereoscopic* observations, i.e. at least two telescopes observe the same EAS: this method enables a more accurate determination of the shower direction by projecting the images of all the triggered telescope cameras into a single camera.

Furthermore, a Cherenkov telescope operates as a self-triggering unit: this means that it has an internal threshold established in terms of photoelectrons (p.e.) or signal amplitude (mV) and, once the signal surpasses this threshold, it activates the readout chain. This trigger is typically dominated by the Night Sky Background photons at low thresholds; increasing the threshold will lead to photons from cosmic and γ-rays becoming dominant.

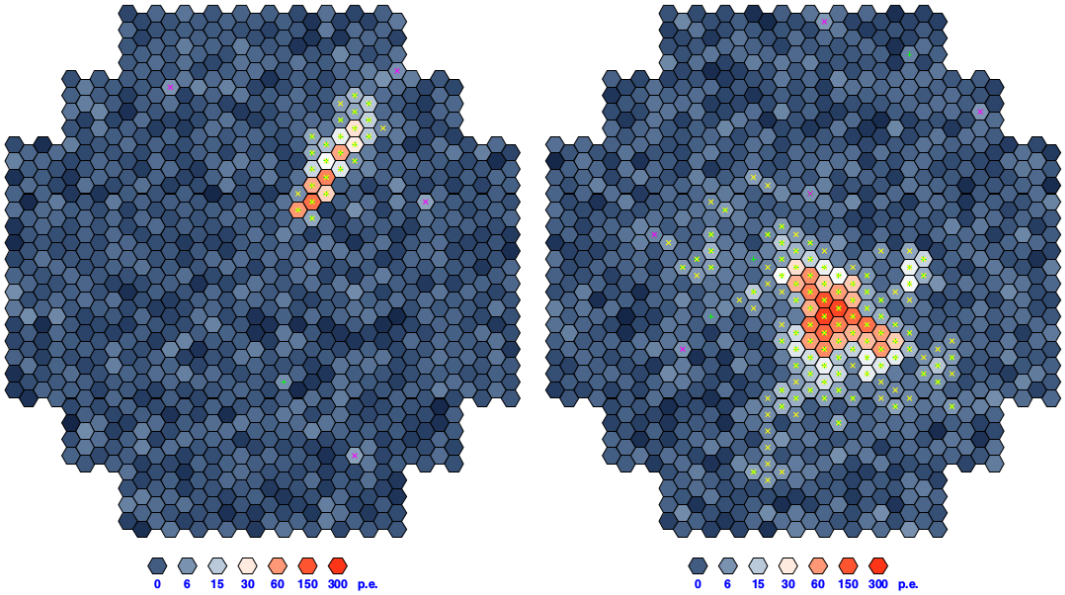

Figure 2.11: Simulations of Cherenkov events detected by the H.E.S.S. cameras and generated by a 1 TeV γ-induced EAS (left) and a 2.6 TeV proton-induced shower (right) [23].

Image analysis

The elliptical images captured by a IACT camera can be analyzed thanks to the so-called "Hillas analysis" [3], which was firstly introduced by M.A. Hillas in 1985 and is based on the study of the characteristics of the ellipse. These allow to reconstruct the direction of the primary cosmic ray, to separate γ-rays from hadrons and to estimate the energy of the primary γ-ray using the integrated intensity of the shower image in the camera, known as the *image size*.

Let's describe the main steps of a typical IACT data analysis. The interesting pixels in an event image are those illuminated by Cherenkov photons generated in the air shower, while the remaining pixels contain only noise signals, caused either by the NSB or by electronics. Thus, an image cleaning is needed in order to isolate the relevant information and select the pixels associated with Cherenkov photons. Once the cleaned and calibrated images are obtained, they can be parameterized using the Hillas parameters: the main ones are (Figure 2.12)

- **Intensity (or size)**: represents the total number of photoelectrons in the cleaned image, directly related to the primary particle's energy
- **Length**: half of the major axis of the ellipse, indicating the standard deviation along the major axis
- **Width**: half of the minor axis of the ellipse, representing the standard spread along the minor axis
- **Center of gravity** (or directly **centroid**): provides the coordinates of the centroid of the shower images relative to the camera center

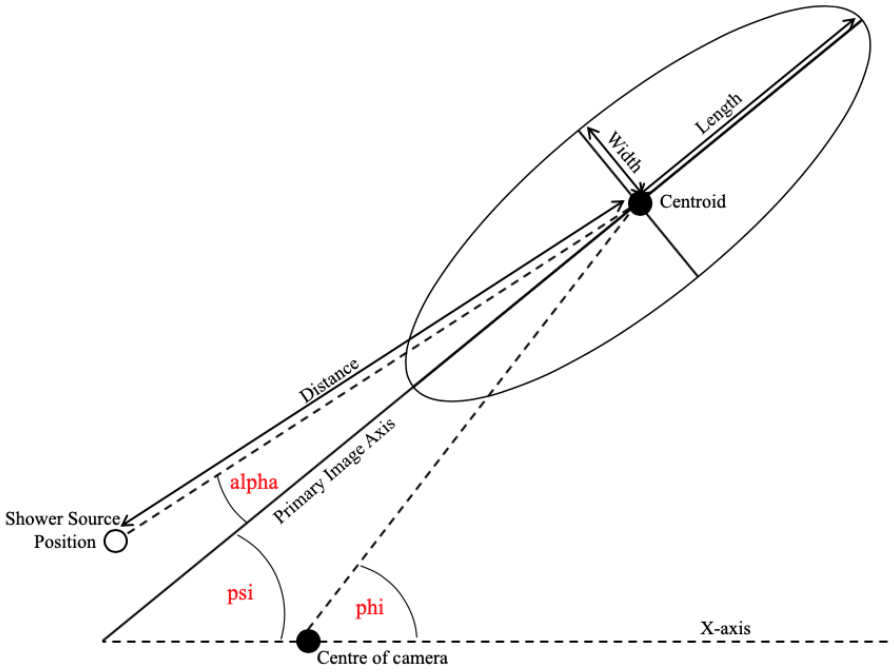

Figure 2.12: Representation of some Hillas parameters [21].

These parameters are associated with individual telescope data; however, when multiple telescopes observe the same event, their information can be combined to achieve a three-dimensional reconstruction of the shower, which is clearly a more powerful approach and is referred to as *stereo mode*. Here, besides obtaining the Hillas parameters for each telescope involved in the event, it is also possible to determine the stereo parameters, which provide a more comprehensive view of the shower; they are mainly the following

- **Shower maximum height**: the height at which the shower reaches its maximum development
- **Core**: the coordinates of the impact point of the shower on the ground
- **Impact**: the distance between the shower axis and the telescope pointing axis

2.2 CTA

The Cherenkov Telescope Array - briefly known as CTA - will be a next generation γ-ray observatory consisting of a multi- km^2 IACT array of numerous closely spaced telescopes of different sizes. CTA aims to observe the whole sky thanks to two sites, one in the northern hemisphere, at Roque de Los Muchachos in La Palma, Canary Islands, and one in the southern, in the Atacama Desert, Chile. Such observatory will be capable of detecting over a wide energetic range, from the tens of GeVs to the hundreds of TeVs, particularly between 20 GeV and 300 TeV: to do so, CTA is developing three telescopes classes with different mirror diameter:

- Small-Sized Telescopes (SST) - 4 m
- Medium-Sized Telescopes (MST) - 12 m
- Large-Sized Telescopes (LST) - 23 m

Each telescope class will have the best sensitivity in a certain energetic range: especially

- SST: 5 TeV - 300 TeV
- MST: 150 GeV - 5 TeV
- LST: 20 GeV - 150 GeV

Both the Medium-Sized Telescopes and the Large-Sized telescopes will have a camera made of Photomultiplier tubes (PMTs) with a field of view of about 8° and 4.3° respectively.

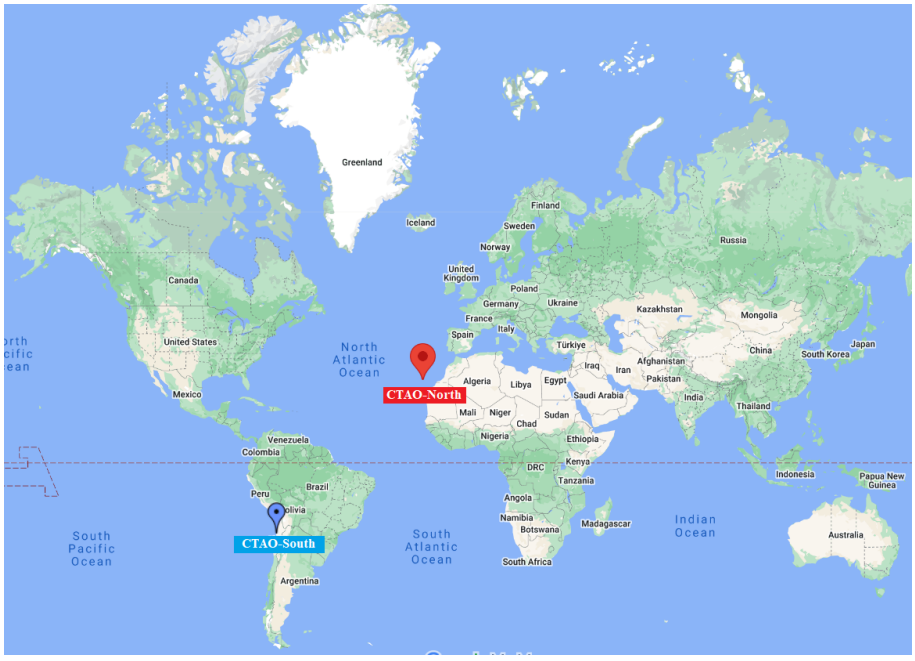

Figure 2.13: CTA sites map.

My work has been focused on the Small-Sized telescopes, that will exploit a Silicon Photomultiplier-based camera.

2.2.1 CTA Sites

The sites of the CTA have been chosen after several analysis of environmental conditions, scientific performance and construction and operational expenses.

CTA-North is situated on the island of La Palma within the Canary Islands of Spain, precisely at the Instituto de Astrofísica de Canarias (IAC) at 2200 m.

CTA-South will be located 10 km south-east with respect to the European Southern Observatory's (ESO) Paranal Observatory. Situated in the arid expanse of the Atacama Desert in Chile, this location is renowned for its extreme dryness and isolation (as shown in Figure 2.14 for the nearby city of Antofagasta, Chile).

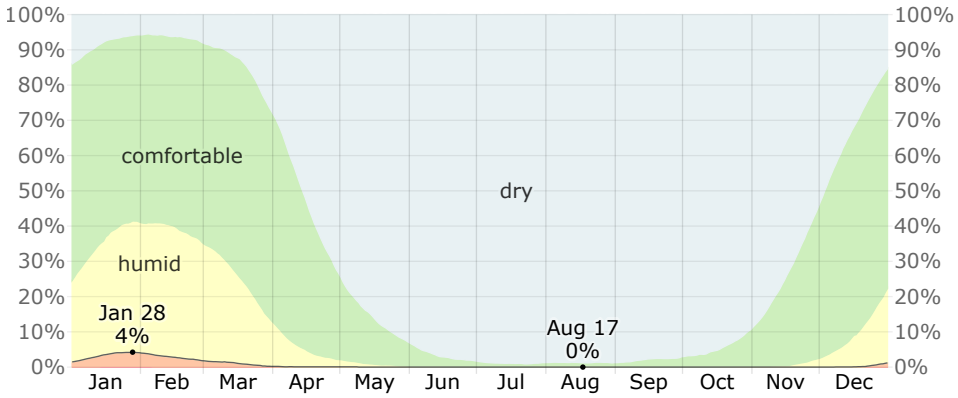

Figure 2.14: Humidity Comfort Levels in Antofagasta, Chile (history) [24].

The layout of the northern and southern arrays of CTA is pictured in Figure 2.15. As we can observe, the northern array will exploit only the Large and Medium Sized telescopes, while the Small Sized ones will be the most numerous in the southern site.

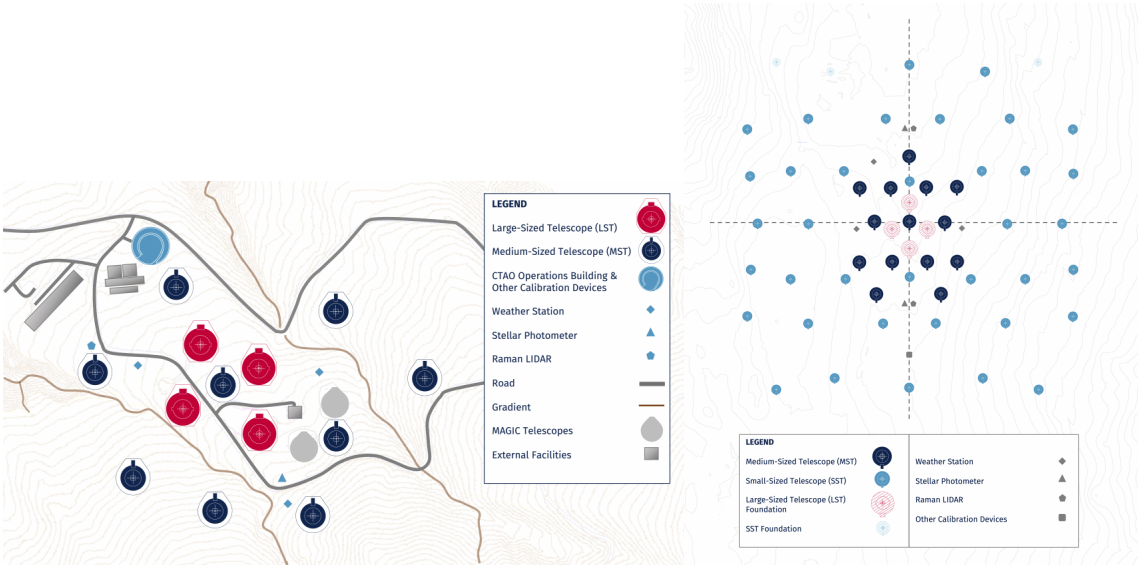

(a) (b)

Figure 2.15: Layout of the northern (a) and southern (b) arrays of CTA [21].

This choice can be explained thinking about the energetic range that each telescope aims to focus on: SSTs are thought to observe at highest energies, where the incoming γ-flux is way lower with respect to lower energies. Therefore, they need to cover a larger area, while the single telescopes can have a smaller sized mirror and detector.

On the other hand, larger telescopes will focus on lower energy ranges, needing larger dimensions for mirrors and cameras in order to capture enough Cherenkov photons. Also, SSTs will be built only in the southern array because most of TeV γ-rays are expected to come from the galactic plane and center, and these are best observed from the Southern hemisphere.

2.2.2 Performance

Although CTA will not be the first ground-based γ-ray facility, it will outperform the currently operating observatories.

The main experimental features of such array have been evaluated specifically for the so-called *"Alpha configuration"*, which consists of

- Northern array: 4 LSTs and 9 MSTs, with a covered area of ~ 0.25 km^2
- Southern array: 14 MSTs and 37 SSTs, with a covered area of ~ 3 km^2

CTA's differential sensitivity, i.e. the minimum flux required to obtain a 5σ detection of a point-like source in a 50 h observation [21], is shown in Figure 2.16a, together with the sensitivity of the other main IACT experiments currently operating, such as MAGIC, VERITAS and H.E.S.S.. In the lower energy range sensitivity is limited by the background noise, while in the higher range by the low γ-ray flux.

In Figure 2.16b the differential sensitivity of the three classes of telescopes is shown.

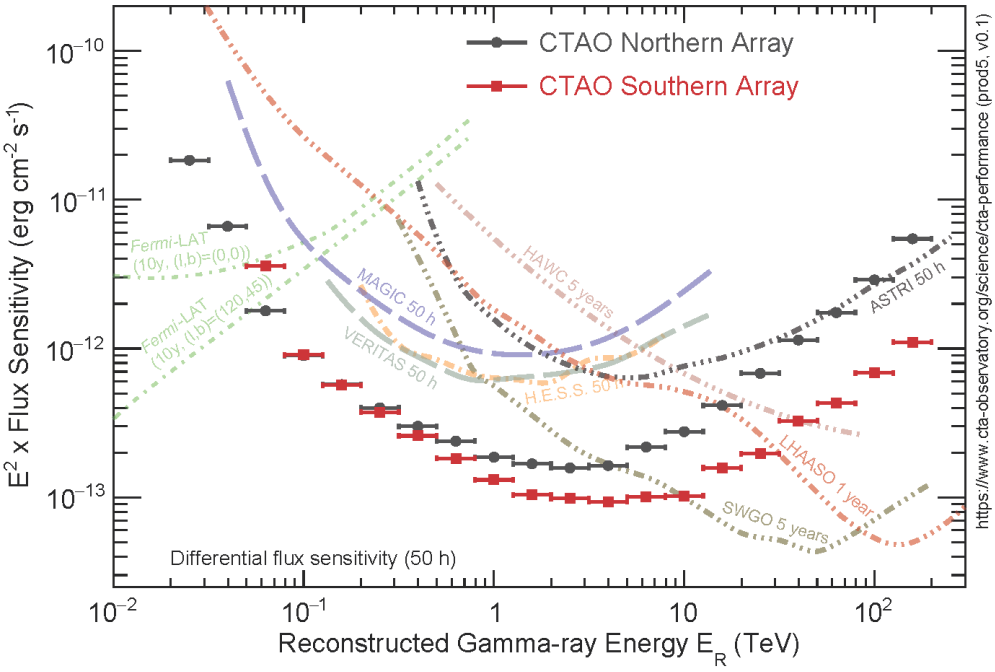

(a) CTA's differential flux sensitivity compared to other experiments. [21]

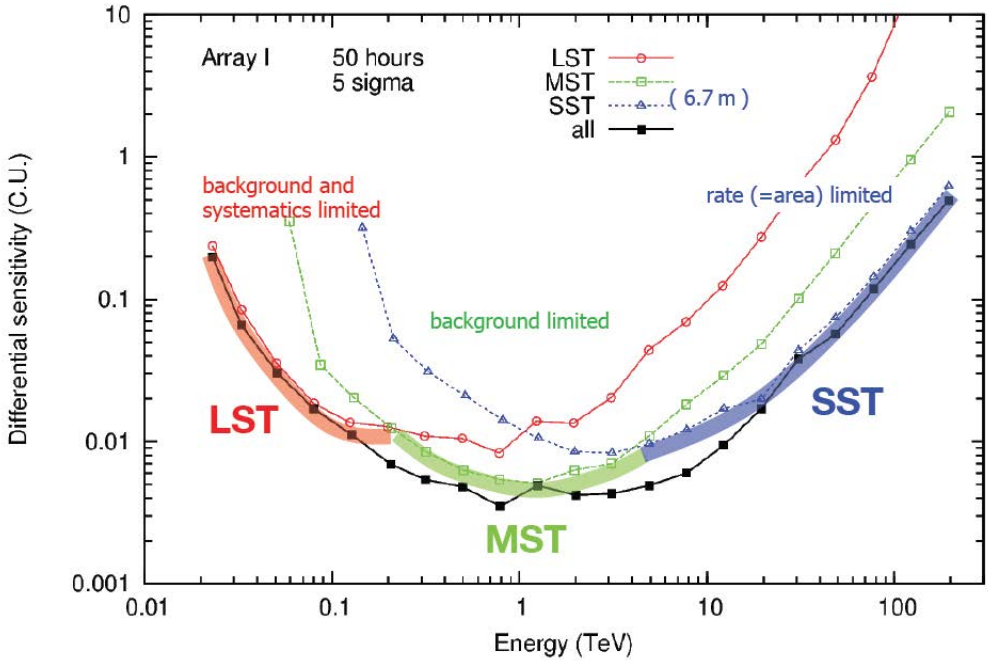

(b) CTA's differential sensitivity - in Crab Nebula units - for the three classes of telescopes [25].

Figure 2.16: CTAO performance.

Chapter 3

The Small-Sized Telescopes

The Small-Sized Telescopes of CTA will have the best sensitivity in the higher part of the observatory's energy range, i.e. between 5 TeV and 300 TeV.

Observing at such high energy levels requires a considerable quantity of SSTs spread over a vast area: the precise number of telescopes and the spacing between each of them are determined through Monte Carlo simulations and cost analysis.

Additionally, the working rate of an SST is 600 Hz, which is in accordance with the simulations and also allows the management of moderate data volumes, a factor that must be taken into account when working with many telescopes.

Each telescope is equipped with a primary mirror of 4 m of diameter. Additionally, SSTs, together with the Schwarzschild-Couder Telescope (SCT) proposed for the Medium-Sized Telescopes, are currently the sole class of CTA telescopes also equipped with a secondary mirror, having then a dual-mirror design.

This mirror configuration prevents the occurrence of coma aberration, which is an optical distortion effect that results in off-axis point sources of light appearing as distorted, comet-shaped blurs instead of clear points. Additionally, it enables the use of a smaller and more compact camera setup since the images produced are smaller in size, allowing the use of smaller pixels that are more commonly available commercially. Therefore, the dual-mirror design has a substantial impact on the economic costs.

The main technical features of an SST are summarized in Table 3.1.

Regarding the specific structure of an SST, it is comprised of the ASTRI telescope structure (**A**strofisica con **S**pecchi a **T**ecnologia **R**eplicante **I**taliana), proposed by INAF, and a camera based on the CHEC-S prototype (**C**ompact **H**igh **E**nergy **C**amera), mainly developed by Max Planck Institut für Kernphysik, Heidelberg (Germany).

The CHEC design was not the only one proposed, as three major candidates were suggested, namely SST-1M, Astri-Horn and, of course, CHEC-S.

After an initial developmental phase and subsequent harmonisation process, CTA chose the SST technology as the dual-mirror Schwarzschild-Couder system based on the ASTRI structure and the Silicon Photomultiplier camera based on the CHEC design.

Pictures of these two main components are shown in Figure 3.1.

The SST camera is then made by an array of Silicon Photomultipliers (SiPMs), which are semiconductor devices and are described in Section 3.2.

SST main parameters	
Optical parameters	
Optical design	Schwarzschild-Couder
Primary mirror diameter	4.3 m
Secondary mirror diameter	1.8 m
Focal length	2.15 m
Mirror effective area	8 m^2
Camera Parameters	
Number of pixels	2048
Pixel size	6×6 mm^2
Camera field of view	8.8°
Mechanical parameters	
Total weight	19 t
Repositioning speed	60 s

Table 3.1: SST main technical features [21].

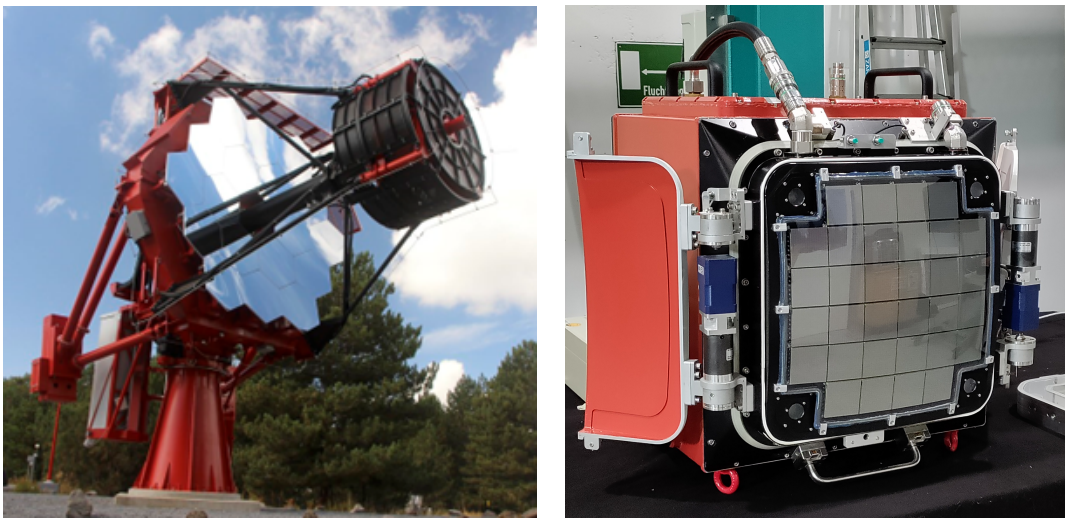

(a) (b)

Figure 3.1: The ASTRI telescope structure proposed by INAF, Italy (a) and the CHEC-S camera developed by MPIK, Germany (b).

For the purpose of this thesis, we will focus mainly on the camera, providing a brief description of the CHEC-S prototype in Section 3.3.

3.1 The final SST Camera design

The design of the SST camera is based on the currently existing prototype and incorporates various modifications and improvements.

This section will focus on these modifications and provide a detailed description of the actual design.

3.1.1 Design changes with respect to CHEC-S

After the commissioning and performance study of CHEC-S, a series of lessons-learned led to modify the design of the prototype for the final SST Camera.

First, the overall mechanical design has been changed in order to incorporate a flat window (Figure 3.2) that substitutes the original curved window of CHEC-S, in order to simplify the manufacturing process.

To avoid obstructing the outermost pixels on the curved focal plane, the window's dimensions must extend beyond the SiPM array, increasing the camera's size and weight; this, however, has minimal impact on telescope shadowing or the effective collection area [26]. Even though this introduction required an expansion in its dimensions, this adjustment allows also an improvement in the air cooling system design.

Furthermore, the entrance window is coated with a special layered coating in order to optimize the transmission of Cherenkov light, while also reducing the intensity of the background from the NSB.

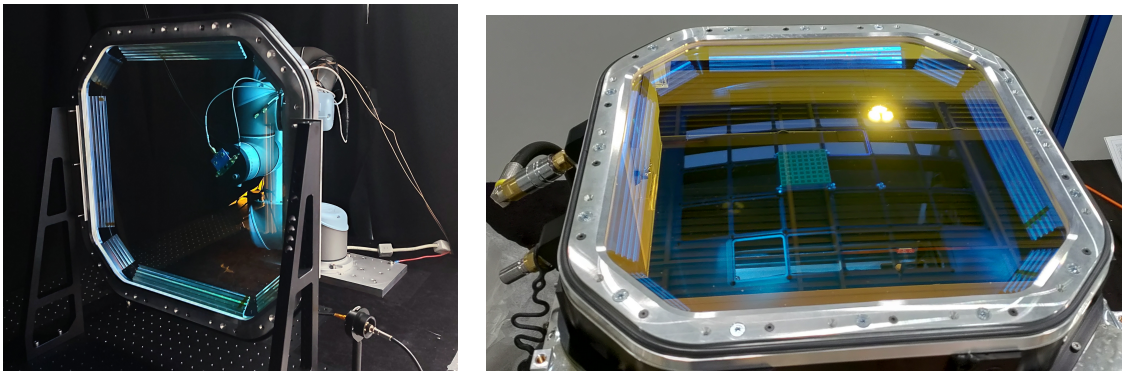

(a) Under test. (From R. White and D. Depaoli)

(b) Mounted on the camera.

Figure 3.2: The SST Camera flat window.

Also, significant advancements in performance have been achieved by SiPM manufacturers since the Silicon Photomultipliers used in CHEC-S were produced: new devices are then employed in the new camera.

After testing various SiPM options, the chosen SiPMs are the ones produced by Hamamatsu Photonics using the 50 µm LVR3 technology (Hamamatsu LVR36050VN); they have an area of 6 mm × 6 mm and don't have any protective coating. The absence of the latter allows to achieve a lower Optical Crosstalk (OCT), because there is no reflection on the coating.

These sensors are designed to achieve a Photon Detection Efficiency (PDE) of at least 50% with an OCT of less than 10%, making it well-equipped to meet the performance demands of the SST [27]; also, their PDE peaks in the near ultraviolet (Near-UV) region [28].

Additionally, it must be noted that upgrading the Silicon Photomultipliers results in changes to the front-end electronics as well.

Furthermore, the calibration flasher has been redesigned, replacing the previous version that used ten LEDs with a single LED with adjustable brightness: the flasher is an on-device system used to calibrate the camera on site.

Finally, in complete contrast to what was done for CHEC-S, the final design presents all power supplies embedded *inside* the camera, on the bottom panel of its enclosure. This was done not only to achieve a more compact camera, but also - and mainly - in order to avoid the use of huge power cables plugged into the camera from the outside, which can be critical when telescopes are moving to reach the requested pointing.

Of course, attaching the power supply system directly inside the camera gives rise to another matter: keeping the whole device cooled and stable, therefore ensuring a good heat dissipation. A discussion about this is presented in Section 5.2 of Chapter 5.

A side-to-side picture of the new SST camera and CHEC-S is shown in Figure 3.3.

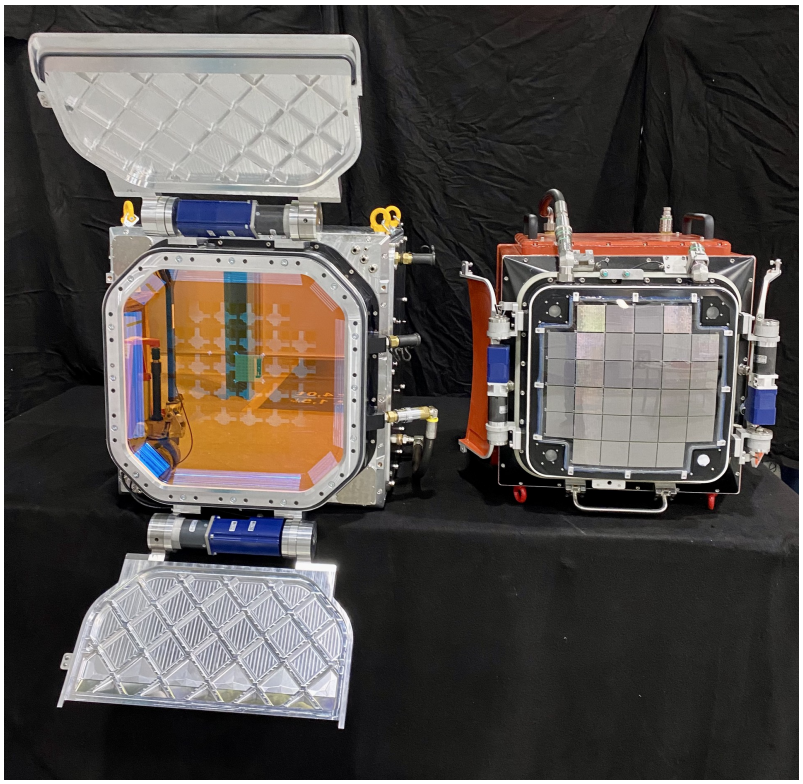

Figure 3.3: The final SST camera under assembly, next to the CHEC-S prototype. From J. Hinton.

3.1.2 Final design

Given the aforementioned design changes, the overall structure of one SST Camera unit (Figure 3.4) will include the following components:

- An enclosure, which is the protective casing for the camera made of machined aluminum components and measures 570 mm x 570 mm x 400 mm; it encompasses a thermal management system and a power supply system. Within the enclosure, there are input connections for AC 220 V power supply, a multi-core fiber connection for data and control transmission, as well as inlet and outlet points for refrigerant fluid.

- A focal plane, which entails the SiPMs mounted on a plate that is subject to liquid cooling, ensuring consistent temperature levels. The SiPMs are safeguarded by the flat coated entrance window.

  Two motorized doors act as a protective shield for the camera when it's not operational. The focal plane also accommodates preamplifiers, bias-voltage supply boards and interface boards, collectively forming the **F**ocal **P**lane **E**lectronics (FPE), which establishes connections with the SiPMs.

- The TARGET Modules (TM): a total of 32 TARGET Modules are integrated, serving as the initial level of triggering and facilitating the signal digitization originating from the focal plane.

- The electronics rack, which is a structure that houses the TMs in appropriate slots. Here there are multiple key components, like the backplane, responsible for camera-wide triggering and data readout, the timing board, that facilitates the generation of precise time stamps, and the slow control assembly that manages the camera doors, the distribution of the power and the environment monitoring within the camera.

- The flasher assembly, which is a system built around LED flashers used for calibration purposes; it features a main component built on the M2 mirror that faces the camera, two led flashers placed on the camera corners and one under the camera lids.

  The two flashers allow to extend the dynamic range of the main flasher and to study the mirror's performance, while the under-the-lid flasher allows the camera calibration through single photoelectron studies.

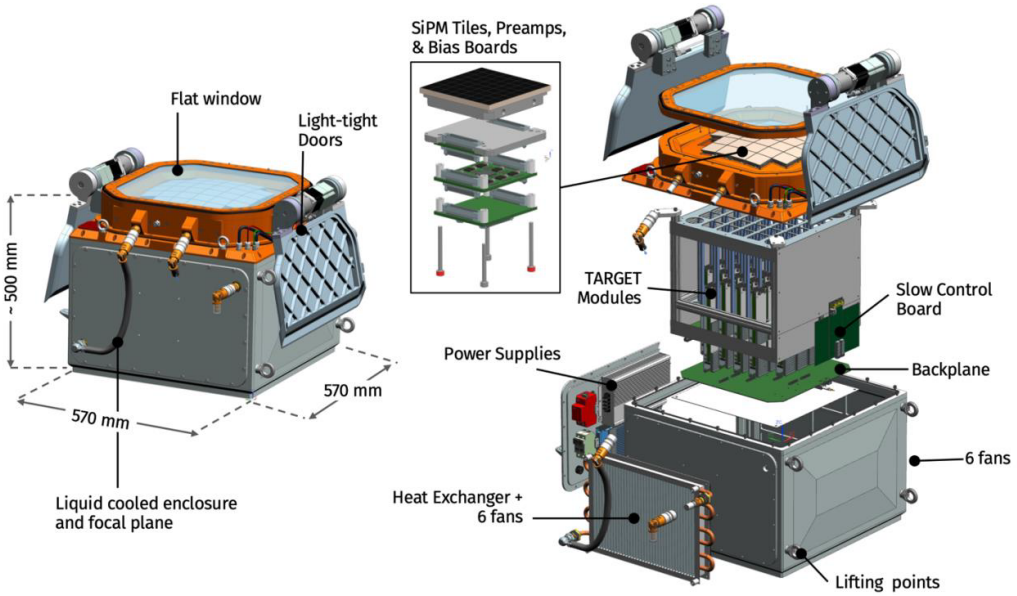

Figure 3.4: SST Camera CAD overview [29].

Lastly, an external chiller cools the camera by circulating a cooled liquid through the focal plane plate, while fans inside the camera move the cold air around. The camera is hermetically sealed and humidity is maintained at an acceptable level by a breather desiccator [30].

A picture of the first SST camera under assembly at MPIK is shown in Figure 3.5.

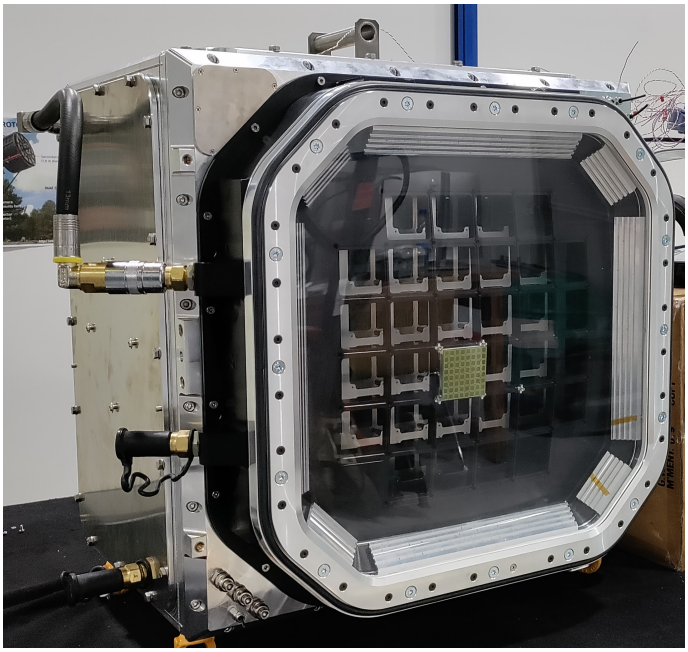

Figure 3.5: First SST camera under assembly, with a dummy plexiglass window on, mounted for the first measurements.

Power supply system

The lower section of the enclosure accommodates two **P**ower **S**upply **U**nits (PSU) with conductive cooling and electrical protection components.

It has been designed based on the fact that the SST camera power comes from a 220 V AC line.

The PSU components include:

- The Main Power Supply Unit, which delivers 24 V at 1500 W and serves to power all of the camera's electronics. Notably, it has a 95% efficiency, features remote ON/OFF control, and incorporates PM-Bus monitoring functionality. Moreover, it offers a 12 V auxiliary power source that keeps the Slow-Control Assembly operational even when the main power is turned off.
- The High Voltage Power Supply Unit, which operates at 48 V and provides 600 W for the bias voltage of the photosensors. It exhibits a 93% efficiency and offers remote ON/OFF control along with PM-Bus monitoring. The power output of this unit matches the power requirements of the SiPM.
- The circuit breakers, often referred to as fuses, are devices that play a crucial role in preventing damage to the surge arrester in instances of extremely close lightning strikes.
- The current surge (or spike arrester), which is a device that serves as a form of lightning protection and is capable of withstanding surges of up to 35 kA.

A CAD overview of such PSU board is shown in Figure 3.6, together with a picture.

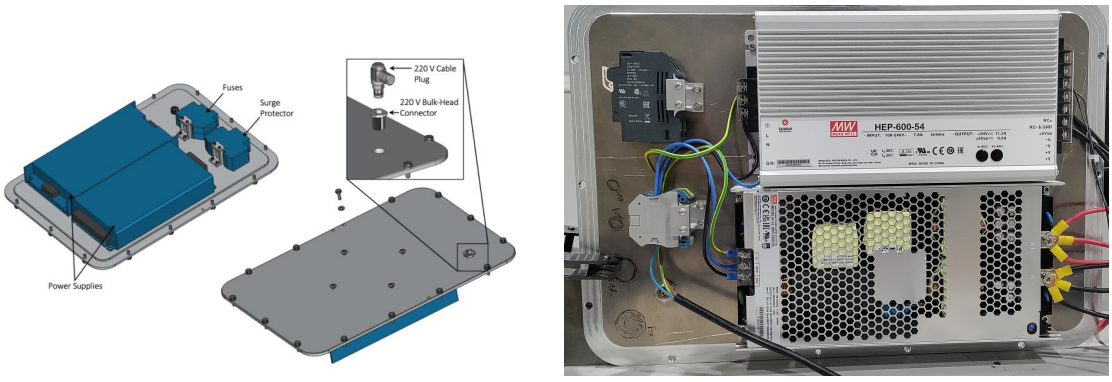

(a) (b)

Figure 3.6: Power panel assembly, CAD overview (a) [29] and picture (b).

SiPM tiles

The Silicon Photomultipliers (Hamamatsu LVR36050VN, 6×6 mm^2) modules are linked to the Focal Plane Electronics, which consists of a stack of printed circuit boards (PCBs). These serve the purpose of providing bias voltage to the SiPMs and preamplifying their signals; furthermore, to ensure accurate compensation for variations in gain within the same tile, each SiPM receives individual biasing.

The signals from the SiPMs are routed through the amplifiers and then go to the readout electronics, which comprises three interconnected boards per module. These electronics are built around the TARGET modules.

TARGET modules

The readout electronics of an SST camera is built around the **T**eV **A**rray **R**eadout Electronics with **G**Sa/s sampling and **E**vent **T**rigger (TARGET) **A**pplication **S**pecific **I**ntegrated **C**ircuits (ASICs). One module is composed of three interconnected **P**rinted **C**ircuit **A**ssemblies (PCAs - Primary, Power, and Auxiliary board), where the ASICs are assembled.

The arrangement of one module is such that each of these ASICs can accommodate inputs from 16 channels, necessitating four ASICs per TARGET Module - two on the primary board and two on the auxiliary board - to effectively handle the 64-pixel SiPMs tile; all these modules are linked to a backplane.

The primary functions of this system are to perform the initial level of triggering and digitize the signals [31].

Indeed, the preamplified SiPMs' signals are first directed to the TARGET module, where they undergo re-amplification and are subsequently split into two separate lines: a fast-signal line and a slow-signal line.

The fast signal goes through further shaping and is then AC-coupled to the TARGET sampling ASICs and the TARGET trigger ASICs.

The initial level of triggering is executed by part of the TARGET module as well: a trigger signal is generated when the sum of the fast signals from four neighboring SiPMs, referred to as a "superpixel", surpasses a set threshold. Each of these trigger signals is transmitted to the backplane board, which serves to determine the camera-level trigger, which is configured to require a coincidence between two adjacent superpixels.

A **F**ield **P**rogrammable **G**ate **A**rray (FPGA) located on the primary board serves the purposes of overseeing the operation of all elements within the TARGET Module, providing command and monitoring interfaces, and facilitating raw data transfer to the backplane [29].

A picture of a full SST camera module is shown in Figure 3.7.

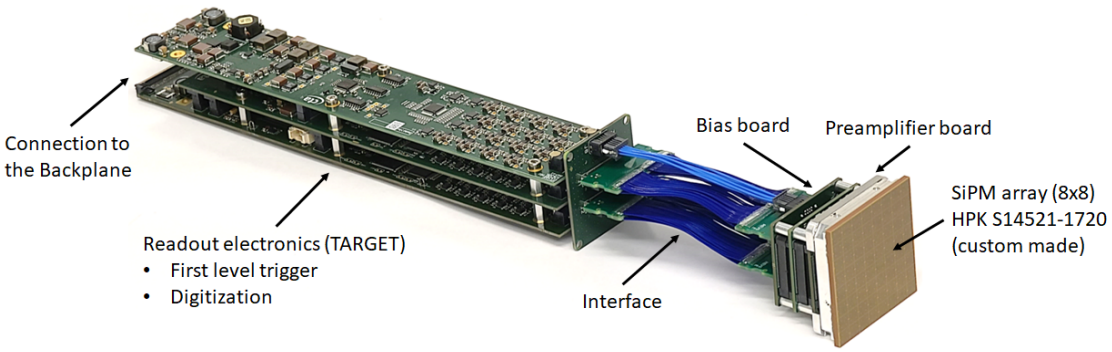

Figure 3.7: New camera module. From J. Lapington.

3.2 Silicon technology and Silicon Photomultipliers

As just seen, each Small-Sized Telescope will be equipped with a camera made of an array of 2048 silicon photomultipliers: before moving forward, we shall describe the Silicon technology, starting from semiconductors.

Semiconductors are fundamental materials in modern electronics, being the basis of essential devices like transistors, diodes, integrated circuits that are used not only in everyday appliances, but also in a great variety of experimental physics fields.

The band model Semiconductor materials typically have a crystalline structure and their electronic properties are usually described by the band model, where the allowed energy levels for electrons are organized into bands (see Figure 3.8 for a schematic representation). According to this model, there are two main relevant bands, the valence band, that contains the electrons that are bound to atoms, and the conduction band, that contains higher energy levels and allows electrons to move more freely. The boundary levels between these two bands are separated by an energy gap, which is defined as the difference between the first (lowest) energy level of the conduction band and the last (highest) energy level of the valence band. The value of E_{gap} varies depending on the type of material: for insulating materials $E_{gap} \geq 6\,\text{eV}$, for conductive materials $E_{gap} \sim 0\,\text{eV}$, while semiconductors have $E_{gap} \simeq 1\,\text{eV}$. For example, silicon has an energy gap of $\approx 1.1\,\text{eV}$ at room temperature ($\approx 300\,\text{K}$), while Germanium has $E_{gap} \approx 0.7\,\text{eV}$.

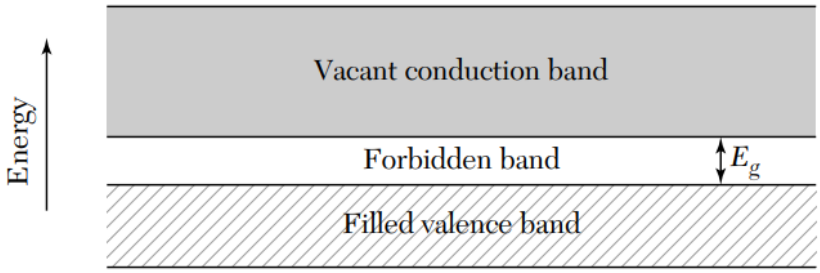

Figure 3.8: Band scheme for an intrinsic semiconductor [32].

According to the band model, when atoms are in their ground state electrons fill the lowest possible energy levels in the material's hierarchy: the material has electrons occupying the valence energy levels. However, when the material is heated - but even if it is just at room temperature - electrons have a certain probability of moving to higher energy levels, transitioning to the conduction band: here, electrons are no longer bound to the atom of origin, instead they exist in an energy level shared by the entire crystal. If an external electric field is applied, electrons in the conduction band can move within the crystal, while electrons in the valence band remain bound to individual atoms. Depending on the type of material, i.e. on the energy gap value, electrons will have a higher or lower probability to "jump" from one band to the other; for example, conductors have the valence and conduction bands very close to each other and are, indeed, conductive. In the next section we will focus on semiconductors, more specifically on silicon.

3.2.1 Intrinsic silicon

As mentioned, silicon has an energy gap of approximately 1.1 eV: with the goal of detecting particles using such a material, we must first see what happens in a silicon substrate.

A particle traversing a silicon substrate loses energy in it, potentially leading to the creation of an electron-hole pair: this means that the energy transferred from the particle to the lattice causes one electron to jump to the conduction band, leaving behind a ionized atom attached to the crystal lattice. The electron's original position is then an empty space, a "hole" or vacancy. The energy loss needed in order to ionize silicon in such a way is 3.6 eV, an amount that is approximately three times the energy gap. Note that in the case of gas detectors, the energy required would be around 30 eV: a particle in silicon generates approximately ten times the amount of charge compared to a gas detector.

Out of the provided 3.6 eV, 1/3 is used to promote the electron to the conduction band, while the remaining 2/3 of this energy go into lattice vibrations (phonons).

Density Silicon is a solid material with a density $\rho \simeq 2.3$ gcm^{-3}; due to its high density, the multiplication process, which is required for example in gas detectors, is not necessary for silicon, because a particle's energy loss can cause a significant number of electron-hole pairs to be produced in relatively small thicknesses. Typically, in silicon, a minimum ionizing particle (MIP) loses about 390 eV/μm, resulting in the creation of approximately 108 electron-hole pairs per μm. The typical thickness used is around 300 μm, in which about 32000 electron-hole pairs can be generated.

Resistivity The resistivity ρ is the inverse of the conductivity σ and is defined as

$$\rho = \frac{1}{\sigma} = \frac{1}{en_i(\mu_e + \mu_h)}$$

where en_i quantifies the charge present in the material and μ_e, μ_h are the mobilities of electrons and holes respectively. The value of ρ determines the current that will flow through the semiconductor: in pure silicon $n_i \sim 1.5 \cdot 10^{10}$ cm^{-3}, which gives a resistivity of $\rho \simeq 235$ kΩcm.

Thermal noise As described, a MIP can typically induce the generation of 32000 $e^- - h$ pairs in silicon. However, there's another factor to consider: this ionization competes with the charge present in the conduction band due to thermal effects. As already mentioned, the probability of having some charge in the conduction band even in the absence of an ionizing particle is not zero, because the material exists at a certain temperature. This is known as thermal noise and constitutes a background noise that generates an electrical signal as well.

In order to quantify this background noise, the Fermi theory comes to help. The intrinsic concentration of electrons is

$$n_i = N_C \cdot e^{-\frac{E_C - E_F}{k_B T}}$$

while the concentration of the holes that remain in the valence band when electrons jump to the conduction band is

$$p_i = N_V \cdot e^{-\frac{E_F - E_V}{k_B T}}$$

where $N_C \sim 2.8 \cdot 10^{19}$ cm^{-3} and $N_V \sim 1.0 \cdot 10^{19}$ cm^{-3} are the numerical densities of the energy levels in the conduction and valence bands, respectively. In intrinsic Silicon, every electron that goes into the conduction band leaves a hole in the valence band: this means that $n_i = n = p_i = p$. Also, this holds always true due to charge conservation. By multiplying the two concentrations we obtain the equation

$$n \cdot p = n_i^2 = Ae^{-\frac{E_{gap}}{k_B T}} = constant$$

which states that this product is a constant value at given temperature and material. The energy level E_F represents the Fermi level and is approximately located at the middle of the energy gap. The energy difference that an electron must overcome in order to transition to the conduction band is evaluated with respect to the energy difference between the conduction or valence band level and this Fermi level.

The numerical charge density in the conduction band at room temperature in intrinsic silicon is, as seen, $n_i \sim 1.5 \cdot 10^{10}$ cm^{-3}, which is a small number compared to the number of atoms present (about $N_A = 10^{23}$ atoms/cm^3), but not so small when compared to the 32000 electrons produced by the ionizing particle. Considering the typical dimensions of a detector, with surface $S = 1 \times 1$ cm^2 and thickness $W = 300$ μm, the number of charges produced solely due to temperature effects, i.e. the thermal noise, is

$$n_i = p_i = 4.5 \cdot 10^8$$

This is much greater than the 32000 $e^- - h$ pairs produced via ionization.

3.2.2 Doped silicon

How can we then use semiconductor materials for particle detection? With Germanium, working at low temperatures could be a good practice, but it is not sufficient for Silicon: the solution is joining two types of differently *doped* silicon, creating a P-N junction.

Doping a material means adding *impurities*, which are atoms of other specific elements that create an excess of positively charged carriers (holes) in the first case and an excess of negatively charged carriers (electrons) in the latter. Such carriers allow to lower the electrical resistivity of the material: pure or intrinsic silicon, in fact, maintains a stable equilibrium between negative and positive charge carriers, which results in an absence of net charge, gives rise to a relatively high resistance and is, therefore, not well-suited for charge collection. In order to make charge collection more effective, *doped* silicon is needed.

Consider pure silicon: it is an element of the IV-a group of the periodic table and has an atomic number of 14. It has four valence electrons in its outermost electron shell

and can therefore form up to four covalent bonds with other atoms in order to complete its octet and achieve a stable electron configuration. Depending on the type of impurity introduced in the silicon lattice, the number of bonds can vary: by adding elements of the V group (donors), which have five valence electrons, an excess of one electron is created, which will act as a mobile charge carrier while the other four will be involved in the covalent bonds. Specifically, the introduced impurity will donate its excess electron to the conduction band. On the other hand, by adding elements of the III group (acceptors), which have three valence electrons, a "hole" will remain in the valence band. Here a hole can move from one atom to another in the lattice and will therefore act as a positive charge carrier. This is how N-type and P-type silicon is made; typically, elements like Phosphorus or Arsenic are used for the first type and elements like Boron or Aluminum for the latter. A schematic example of the basics of the doping process is pictured in Figure 3.9.

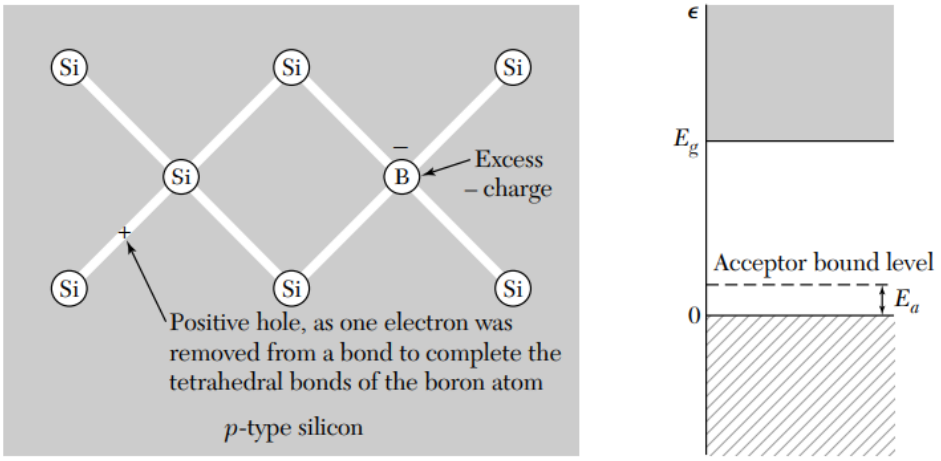

(a) Charges associated with a boron impurity atom in silicon. Boron has only three valence electrons, while silicon has four valence electrons: thus, the positive hole leaved behind is available for conduction.

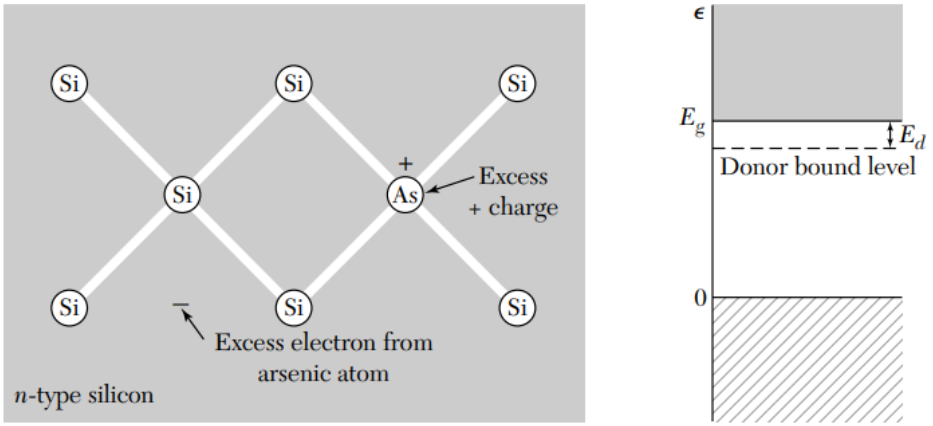

(b) Charges associated with an arsenic impurity atom in silicon. Arsenic has five valence electrons: thus, the fifth electron is available for conduction.

Figure 3.9: P-type and N-type silicon [32].

Doping can be more or less intense: as seen, there can be approximately 10^{10} electron-hole pairs due to thermal effects. Therefore, the starting point for doping concentration is around $10^{13}\,\mathrm{cm}^{-3}$, enhancing either n-type or p-type conduction. This quantity is not sufficient to change the overall nature of silicon: it locally modifies its conduction properties without transforming the material and this is why we refer to it as doped silicon. Also, we must keep in mind that $10^{13}\,\mathrm{cm}^{-3}$ is greater than the number of thermal electron-hole pairs, but less than the number of atoms in silicon ($\approx 10^{22}\,\mathrm{cm}^{-3}$).

A high doping level involves adding a concentration of up to $10^{20}\,\mathrm{cm}^{-3}$, which is kind of an upper limit; in this case, we refer to it as n^+ or p^+ doping, which results in highly conductive elements.

P-N junction The importance of the presence of excess holes and electrons becomes evident when joining together a P-type silicon region and a N-type one, creating what is called a P-N junction. Here, there will firstly be a higher concentration of electrons on one side and of holes on the other side, which will lead to a diffusion process. Indeed, electrons from the n-side will diffuse towards the p-side, leaving positively charged atoms behind, and holes from the p-side will diffuse towards the n-side, leaving negatively charged atoms behind. When electrons and holes encounter each other, they recombine, neutralizing their charges, which results in the creation of a depletion layer near the junction, where there are no free charges. This charge distribution creates an electric field across the depletion layer, reaching its peak at the P-N junction where opposing charges are closest. This electric field "counteracts" the diffusion of carriers by pushing electrons away from the p-side and holes away from the n-side. This process opposes the carrier movement that initially established the electric field and ultimately leads to an equilibrium state.

A schematics of such process is pictured in Figure 3.10.

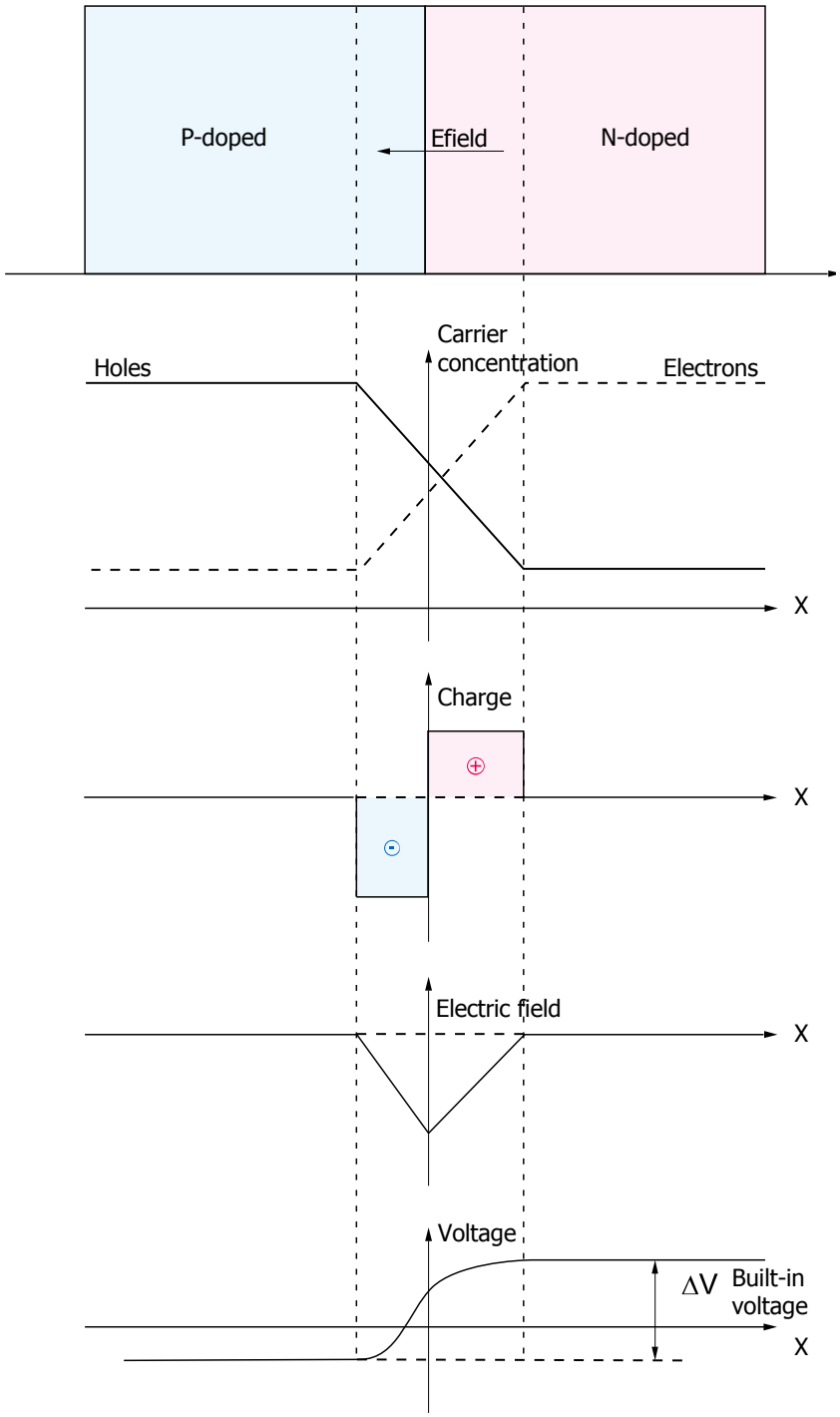

Figure 3.10: P-N junction at equilibrium [33].

Polarized P-N junction When an external voltage source is applied to a P-N junction, the electrical characteristics of the device can be modified and the application of such voltage is called *bias*; a junction can be in a *forward bias* configuration or in a *reverse bias* configuration. The first can be achieved by connecting the negative terminal to the n-type region and the positive terminal to the p-type region: when voltage is applied in this way, it drives forward electrons within the n-type material and defects electrons in the p-type material towards the junction. As a consequence, the size of the depletion zone reduces and if the applied voltage is sufficiently high, it counteracts the internal electric field formed by the diffusion process. As a result, electrons from the n-type region and defect electrons from the p-type region can traverse the junction.

The reverse bias configuration is achieved by connecting the negative terminal to the p-type region and the positive terminal to the n-type region. In such situation, the holes within the p-type region are drawn away, resulting in the accumulation of charged ions, which contributes to the expansion of the depletion region. An analogous process takes place in the n-type region. The widening of the depletion region leads to an increase in the electric field within the junction, consequently intensifying the electric force exerted on charge carriers; such force moves the carriers, causing an increase in their speed and kinetic energy, which will result in interactions between the carriers and the atoms of the material. During these interactions energy is dissipated through the thermal vibrations of the crystal lattice, commonly referred to as phonon vibration.

Avalanche Photodiodes When the applied voltage exceeds a threshold value called *breakdown voltage*, a substantial current flows in the device. Under such circumstances, when an electron-hole pair forms, each charge carrier experiences a high electric field: between successive collisions, these carriers can accumulate sufficient energy to exceed the silicon band gap, which can result in the ionization of lattice atoms upon impact, generating at least one more electron-hole pair in the conduction and valence bands, respectively. This process is exponential, leading to the phenomenon known as *avalanche breakdown*; this is indeed the working mode of an Avalanche Photodiode.

The value of the breakdown voltage depends mainly on the width of the depleted region and, in general, on the diode's structure. Assuming a constant electric field within the depleted region, an increase of the width of the depleted region corresponds to an increase in potential collisions, with the consequence of having a lower critical electric field at breakdown. At the same time, the breakdown voltage is the integral of the electric field over the entire region: a wider region will then give a higher electric field.

The avalanche gain process just described is extremely important, since it can amplify a small initial signal and make it detectable; of course, this applies also to any thermal noise in the device, but given that the avalanche multiplication is intrinsically random, this can be quantified by an additional noise factor when evaluating the internal gain of such a device.

A very peculiar feature of APDs is that their gain depends on the wavelength of incoming light. A photon can, indeed, induce the generation of an electron-hole pair in the material via photoelectric effect, and both carriers can trigger an avalanche; however,

electrons in silicon have higher ionization efficiency, leading to a greater probability of inducing an avalanche compared to holes. Hence, the difference in photo-sensitivity of the device arises from the distance an electron will travel within the depletion layer before being collected. Devices can be structured as N-on-P or P-on-N: the N-on-P configuration is sensitive to longer wavelengths in the UV/blue spectrum, while P-on-N is more responsive to the red/NIR spectrum. This is important to keep in mind since our focus is on detecting γ-rays through Cherenkov light.

Another trait of APDs is their gain's dependence on reverse voltage, which can be considered linear in first approximation.

3.2.3 Silicon Photomultipliers

Silicon Photomultipliers (SiPMs) are semiconductor devices made of an array of APDs; one single SiPM, that will mostly be referred to as *pixel* here, will contain several thousands of APDs, called microcells, each of a size of a few tens of µm. Such array of APDs has a common bias and a common output (Figure 3.11) and the photodiodes are connected in parallel and fabricated on the same monolithic silicon crystal. As previously mentioned, a photon or thermal excitation can generate an electron-hole pair in the depleted region; this pair may subsequently trigger an avalanche in the microcell, amplifying the initial signal. Additionally, a quenching resistor is employed to limit the current and restore the microcell to its quiet state, making it photosensitive again. Hence, one avalanche is proportional to a single electron-hole pair, also called photo-electron (p.e.), and generates a certain amount of charge. The signal of one SiPM pixel is then the sum of the signal of all microcells, read out over their quenching resistor via the common output.

Being an array of individual digital photodetectors, SiPMs can precisely measure the number of incident photons on their surface.

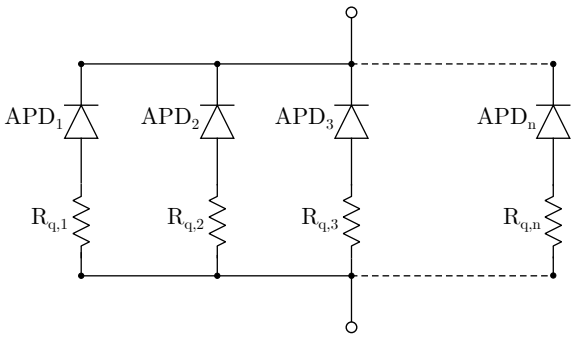

Figure 3.11: Schematic circuit of a SiPM as an array of APDs connected in parallel [34].

Breakdown voltage

The electrical properties of SiPMs are intricately tied to the SiPM overvoltage, which is the difference between the bias voltage and the breakdown voltage. However, the breakdown voltage's sensitivity to temperature cannot be overlooked: comprehending how this value varies with temperature is crucial for an optimal sensor operation.

Under bias, each charge carrier — whether an electron or a hole — is accelerated by the electric field while traversing the depleted region. When a carrier encounters an atom in the lattice or a phonon, a certain minimum energy, referred to as the threshold energy, is necessary to trigger the generation of another electron-hole pair. If a collision occurs where the energy of the accelerated carrier falls below this threshold, it will lose energy without producing an additional electron-hole pair. As temperature rises, collisions become more probable, causing the average energy of carriers to decrease. Consequently, the minimum electric field required for initiating a self-sustained avalanche increases with temperature.

This explains the observed correlation between an increase in breakdown voltage and a rise in temperature. This dependence closely associates with the sensor's internal structure: the wider the depleted region, the greater the breakdown voltage's sensitivity to temperature.

Photon Detection Efficiency

Photon detection efficiency (PDE) measures the capability of a single-photon detector to detect photons; it is the ratio between the number of detected photons and of incoming photons. The PDE is computed as

$$PDE = QE \cdot P_T \cdot FF_{eff}$$

Where QE is the device's quantum efficiency, P_T the probability to trigger an avalanche and FF_{eff} the effective geometrical fill factor, i.e. the ratio of active to inactive area on the SiPM, which needs to be considered when evaluating the PDE of a SiPM's photodiodes. It is important to note that the quantum efficiency QE, the avalanche triggering probability P_T and the fill factor depend on the incoming photon's wavelength λ; P_T also depends on the overvoltage V_{OV}. The PDE then depends on λ and V_{OV}. Quantum Efficiency is evaluated taking into account the probability of a photon to enter the detector without being reflected and subsequently being absorbed in the functional region of the device, where the carriers have a possibility to reach the active region before being re-absorbed.

The probability of triggering an avalanche, P_T, depends on the electric field and thus by the overvoltage and the location where carriers are created.

The effective fill factor is tied to the design and internal structure of the photodiode, particularly influenced by the uniformity of electric fields, for example [35].

Dark Count Rate

Similarly to Avalanche Photodiodes, in SiPMs thermal energy can provide enough energy to an electron in the depletion layer, causing it to transition from the valence band to the conduction band and resulting in a hole in the valence band. If this electron-hole pair initiates an avalanche, it produces a signal that is indistinguishable from a signal generated by a photon.

These events caused by thermal energy are commonly known as *dark counts*. The **D**ark **C**ount **R**ate (DCR) is defined as the number of dark counts occurring in a given time interval.

Being so strongly related to thermal motion, the Dark Count Rate increases together with temperature and constitutes one of the most significant limits of SiPMs. Also, at a given temperature, the dark count rate increases with increasing overvoltage.

Optical Crosstalk

During an avalanche process, secondary photons can be emitted by accelerated carriers the high-field region: these additional photons typically amount to $3 \cdot 10^{-5}$ photons per avalanche carrier [36], resulting in approximately 30 photons when assuming a typical SiPM gain of 10^6; these photons have wavelengths in the near-infrared range and can propagate considerable distances through the silicon material. This emission is isotropic and gives rise to absorption and generation of new carriers in the neighboring cells. Photons can reach the adjacent microcells through various paths: for example, via direct transmission to a neighboring microcell, or by reflection from the upper window material that shields the sensor, which is usually epoxy or glass, or by reflection from the lower surface of the silicon substrate. Optical Photon Crossover Talk, typically referred to just as Optical Crosstalk (OCT or CT), represents the probability that these secondary photons not only get emitted, but also trigger a secondary avalanche within a neighboring microcell. This can lead to situations where a single incoming photon might occasionally produce signals equivalent to two or three photons or more: OCT is therefore a peculiar feature of devices like SiPMs and, actually, a disadvantage.

Furthermore, OCT can be distinguished in *prompt* or *delayed* crosstalk, with the first being the phenomenon we just described. Delayed crosstalk, on the other hand, arises from the generation of electron-hole pairs by secondary photons within the bulk or adjacent neutral regions close to the depleted region. These charge carriers diffuse and a portion of them may reach the active region, initiating an avalanche with a delay ranging from several ns to µs.

A high OCT negatively impacts various performance aspects of the sensor, such as charge resolution and trigger efficiency. Consequently, it is good practice aiming for a low OCT by lowering the overvoltage; however opting for a lower overvoltage also leads to reduced PDE and gain. Therefore, a compromise between these conditions must be made.

Afterpulsing

During an avalanche process, a small fraction of the carriers can be trapped in the intermediate energy levels introduced by impurities. They can be released after a short delay upon acquiring sufficient energy to return to the conduction or valence band. These released carriers can trigger another avalanche, resulting in a detectable signal, which occurs delayed with respect to the original one and is called an "afterpulse".

If an afterpulse occurs before the microcell has fully recovered, its pulse amplitude will be lower than the one of a normal signal, allowing it to be distinguished from real events. Conversely, if an afterpulse occurs after the microcell recovery time, it will exhibit the same shape and amplitude as a regular one-photoelectron signal.

An example of output signals containing different kinds of noise is pictured in Figure 3.12.

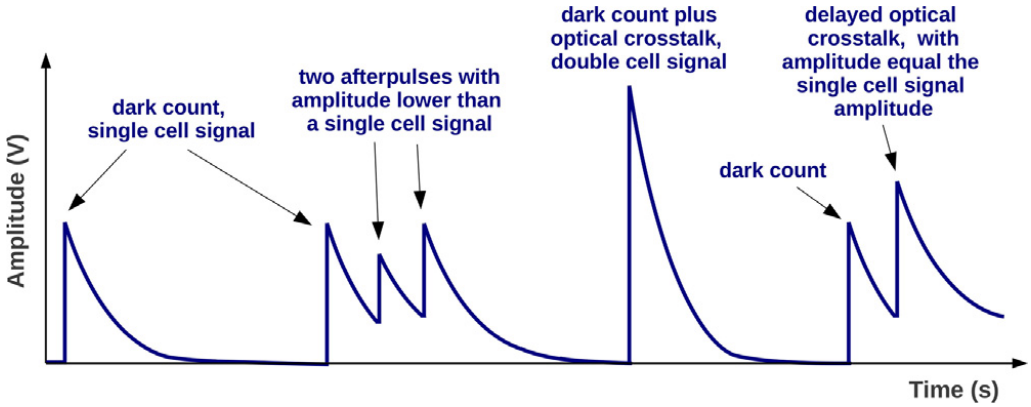

Figure 3.12: Representation of the output signal of different kinds of noise observable: primary events, prompt crosstalk, afterpulsing and delayed crosstalk events [35].

Advantages and limits of SiPMs

Silicon Photomultipliers are very promising devices that are increasingly being employed in many experimental physics fields, at the expense of, as far as it regards IACTs for example, Photomultipliers Tubes (PMTs).

Indeed, SiPMs can reach very high peak quantum efficiencies and PDEs and require lower operating voltages. Also, they are independent from electromagnetic fields and they are quite robust to high illumination levels: this is important not only when referring to the handling process of these devices, but also when thinking of a IACT operating under high-background illumination, such as under the moonlight or in situations where the moon passes across the field of view during a change in the telescopes' position.

Furthermore, the manufacture of SiPMs is simpler and more cost-efficient with the price per mm^2 steadily decreasing: this trend is expected to continue, making SiPMs a more viable choice than other photomultiplier technologies. Additionally, the current development of SiPMs is greatly active, being a relatively new technology and having applications in various fields, especially the medical one.

Of course, as we already grasped, SiPMs are not perfect: they present several technical challenges, such as Optical Crosstalk and temperature dependence of many parameters, like the Dark Count Rate and the gain. This requires a precise monitoring of the SiPMs temperature, which allows to perform temperature corrections of such parameters.

Furthermore, although SiPMs allow to reach a higher peak sensitivity with respect to other devices, this sensitivity extends also to higher wavelengths, for example in the red, making SiPMs more sensitive to the Night Sky Background photons.

3.3 CHEC-S: a prototype for SST

Since it is designed for dual-mirror, Schwarzschild-Couder telescope optics, CHEC has a compact size (approximately 0.5 m in diameter) and light weight (around 50 kg).

The focal plane of CHEC-S is curved and equipped with 32 Hamamatsu S12642-1616PA-50 photosensors, each housing 64 6 x 6 mm^2 pixels, where every pixel is composed of four SiPMs measuring 3 x 3 mm^2 that are connected in parallel. The camera therefore has a total of 2048 pixels. The photosensitive area of each pixel is covered by a thin-film coating, approximately 20 μm thick, with a refractive index of 1.55.

The SiPMs constituting CHEC-S feature an OCT of approximately 33% and a PDE of $\sim$ 31% [37]. Their gain changes by 3.7% $°C^{-1}$ [22], showing quite a strong temperature dependence, which stresses the need of an accurate monitoring and stabilization of the temperature. The SiPMs' dark count rate also increases with temperature, and can be suppressed by operating the SiPMs at reasonably low temperatures, i.e. below 20 °C.

To address the temperature dependence of SiPM performances, each SiPM tile in CHEC-S is bonded to a copper heat sink that connects to a water-cooled focal plane plate. For temperature monitoring, a temperature sensor is affixed to each SiPM.

In terms of **F**ront-**E**nd **E**lectronics (FEE), CHEC employs 32 FEE modules with custom TARGET ASICs. These modules continuously sample and digitize the incoming signals at a rate of 1 GSa/s, while also performing a preliminary trigger by discriminating the analog sum of four adjacent pixels (called *superpixels*).

The back-end electronics consists of two data acquisition boards for off-camera data transfer, along with a backplane that delivers power, clock, and trigger connectivity to the FEE modules [38].

A schematic representation of the hardware components of CHEC-S is shown in Figure 3.13.

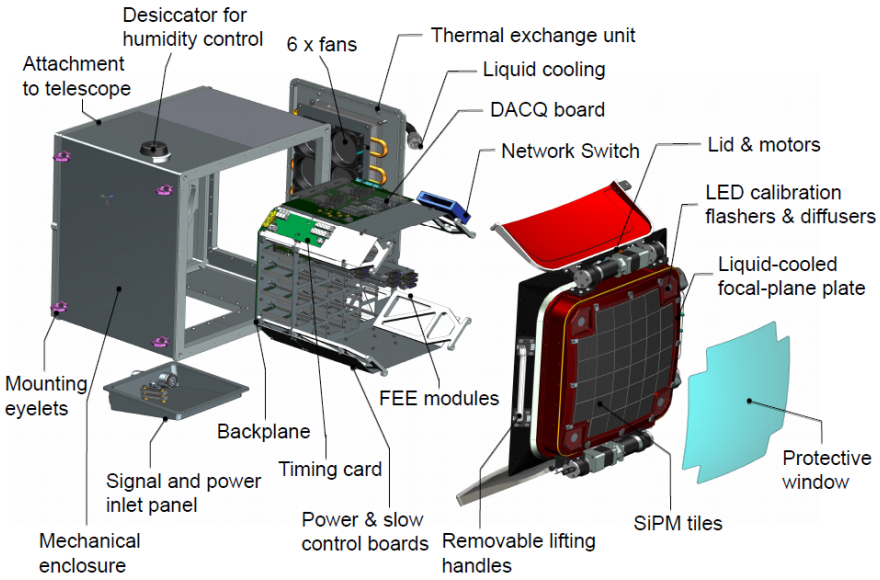

Figure 3.13: Hardware components of the CHEC-S camera [38].

Chapter 4

The Commissioning Facility

As anticipated in Chapter 2, several SST Cameras will be manufactured for the CTA observatory: after the completion of the entire camera **A**ssembly, **I**ntegration, and **T**esting (AIT) process, a series of pre-shipment verification tests will be performed for each camera at the Max Planck Institute for Nuclear Physics (MPIK) in a designated facility. These verification tests will comprehensively evaluate all essential functional and performance aspects of the camera system.

The aim of this process is to systematically evaluate the operational characteristics of the camera and its ability to meet the specified performance criteria [39].

Some of the pre-shipment verification procedure steps consist in the following:

1. Calibration of the facility to ensure a well understood and reliable setup
2. Basic tests
   (a) Camera state-transition tests, including warm-up and stabilisation
   (b) Door functionality tests
   (c) Pixel functionality via uniform illumination
   (d) Pixel functionality via internal illumination system, i.e. a flasher LED connected to leaky fibre
   (e) Data acquisition and dead time tests
3. High-level calibration tests
   (a) Single photoelectron (p.e.) spectrum calibration
   (b) Gain-matching
   (c) Flat fielding
   (d) Trigger calibration
   (e) Time correction
   (f) Slow signal calibration
4. Performance tests

   (a) Charge resolution
   (b) Time resolution
   (c) Trigger efficiency
   (d) High NSB tests

5. Calibration parameters stability tests
   (a) Daily tests
   (b) Long-term over-weekend cycling tests

In order to carry out these verification tests effectively, a well-calibrated illumination setup installed in a completely dark environment is essential: such setup should ensure a correct and accurate measurement of the camera's response without any interference from external light sources.

For the reliability of such an environment, the setup has to be stable, therefore it must be fully remotely controllable from the outside.

For this purpose, a commissioning facility - here also referred to as DarkBox - was designed and built in the experimental halls at MPIK. The work presented in this chapter has been carried out both in person at the Max Planck Institute and remotely from Turin.

The commissioning facility consists of a dark room with black inner walls containing the experimental setup required to perform the pre-shipment verification tests for all the SST cameras; a picture of such a DarkBox is shown in Figure 4.1.

The facility measures approximately 6 m in length and 3 m in height and width, being indeed quite huge. Such dimensions have been chosen in order to be able to completely illuminate the cameras while avoiding the dependence of the SiPMs response on the angle of incidence of the light.

In fact, placing the camera under test, which has a diameter of 0.57 m, at a 3 m distance from the light source, gives a maximum angle of incidence of $\arctan(0.285\ \text{m}/3\ \text{m}) = 5.43°$.

As mentioned above, a well-calibrated illumination setup is needed: in particular, it must mimic the background light that a detector is exposed to during an observation - the aforementioned Night Sky Background - and the Cherenkov light. Therefore, the work described here has focused on assembling and characterising such a setup in order to meet the specific requirements of the CTA collaboration and to provide a stable and well-known experimental environment.

Figure 4.1: The Commissioning Facility at MPIK Laboratories: it measures approximately 6 m in length, 3 m in height and width.

4.1 Experimental setup

The experimental setup can be divided into two main parts: the light source board, where all the optical components needed to simulate the light signals are mounted, and the rotating stage, where the detectors will be placed. The light source board is located at one end of the DarkBox and all its components are mounted on a black Thorlabs board; this contains all the devices needed to simulate the desired light, both for the NSB and the Cherenkov light. A picture of the optical setup is shown in Figure 4.2.

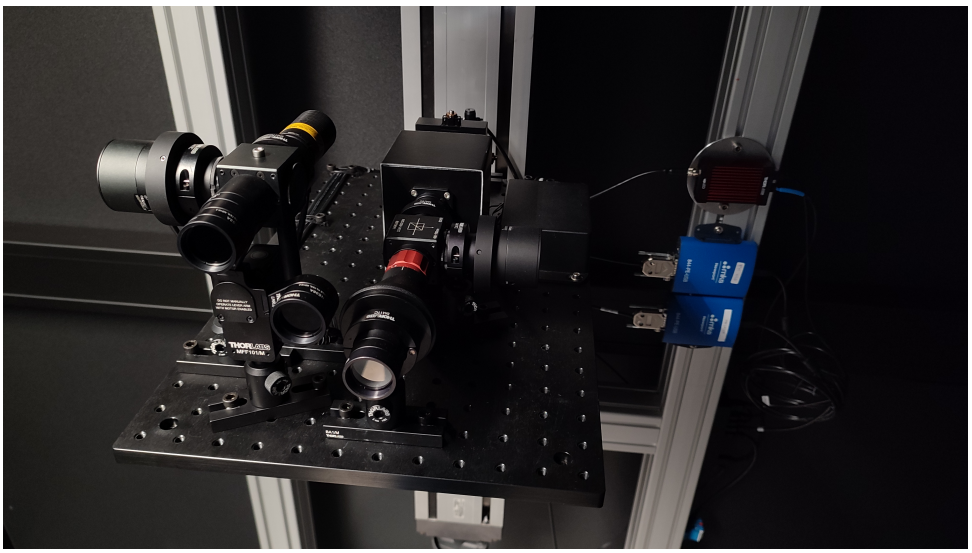

Figure 4.2: Light source setup.

Such a setup is further divided into two different subsystems: the NSB and the Cherenkov sources. In both subsystems, the device chosen to monitor the light emission is a Newport 918D-UV-OD3R High Performance Photodiode, or "powermeter" for

short.

A third powermeter is placed on the rotational stage in order to monitor the emitted light at 3 m distance from the sources.

Additionally, a UR5 Robot Arm is placed between the light sources and the rotational stage, with the purpose to periodically study the light beams.

4.1.1 Powermeters

The Newport 918D-UV-OD3R High Performance Photodiodes (Figure 4.3) are highly sensitive, low noise semiconductor photodiodes that allow measurements in the ≈ pW - mW range; the built-in attenuator extends this range up to the ≈ mW - W range. Their spectral range lies between 200 and 1100 nm.

These detectors are calibrated instruments and calibration data is provided with and without the optical attenuator. To obtain accurate power measurements, the user must "manually" set the optical meter to the correct wavelength for the light source that is being measured; such setting is implemented in the facility software (briefly described in Section 4.1.5).

Figure 4.3: Newport 918D-UV-OD3R High Performance Photodiode.

During data acquisition in the commissioning facility, the *relative* quantum efficiency and responsivity of the powermeters were measured as a function of the light's wavelength. The data provided by the manufacturer allowed such measurements to be compared and validated (Figure 4.4).

Responsivity and Quantum Efficiency Quantum efficiency QE is defined by the number of electrons generated for every incoming photon; we can express it by

$$QE = \frac{R_{pe}}{R_{ph}} \tag{4.1}$$

where R_{pe} and R_{ph} are the rates of incoming photoelectrons and photons, respectively. Quantum efficiency is a consequence of both the semiconductor material and the structure of the photodiode.

On the other hand, responsivity ρ is a measure of the performance of the photodiode, which tells how many mA of photocurrent can be generated for every mW of input signal optical power. If the photodiode receives N photons in a time window Δt, the optical power is $P = N \cdot h\nu/\Delta t = R_{ph} \cdot h\nu$, where $h\nu$ is the photon energy. If the quantum efficiency is equal to 1 - that is, if each photon generates an electron - the photocurrent will be $I = N \cdot e/\Delta t$, so that the responsivity is $\rho = I/P = e/h\nu$ [40].

Considering that usually the quantum efficiency is non-ideal, i.e. it differs from 1, the photodiode responsivity will be

$$\rho = QE \cdot \frac{e}{h\nu} \tag{4.2}$$

The responsivity and quantum efficiency of a photodetector are, then, closely related quantities.

The use of powermeters as photodetectors allows to measure the power emitted by the source, which is the amount of energy emitted in a given time interval, $P = E/t$; the energy E can be expressed as the energy of a single photon $h\nu$ multiplied by the number of photons N_{ph}. Then we obtain

$$P = \frac{N_{ph} \cdot h\nu}{t} = R_{ph} \cdot h\nu$$

Obtaining the expression of R_{ph} using Eq. 4.1, the measured power is

$$P = \frac{R_{pe}}{QE} \cdot h\nu$$

So far, we have talked about *absolute* quantities; however, there was no direct way to measure the rate R_{pe} with the current setup of the commissioning facility.

Then we measured only *relative* quantities while ensuring a constant rate of photoelectrons during data acquisition. In order to do so, we supplied the device under test with a constant light from the laser source.

Then, it has been possible to obtain the relative quantum efficiency of the powermeter (Figure 4.5), together with its relative responsivity, by measuring the emitted power at different set wavelengths.

Such a measure was carried out using an implemented Python script that looped over a wavelength range between 200 and 1100 nm (the optical range of powermeters) and set the "observed" wavelength at each step.

The relative QE is then evaluated as

$$QE_{rel} = \frac{QE_i}{QE_{ref}} = \frac{P_{ref}}{P_i} \cdot \frac{\nu_i}{\nu_{ref}} = \frac{P_{ref}}{P_i} \cdot \frac{\lambda_{ref}}{\lambda_i}$$

With reference value $\lambda_{ref} = 405\,\text{nm}$, which is the wavelength of the laser source.

Relative responsivity is analogously obtained as

$$\frac{\rho_i}{\rho_{ref}} = \frac{QE_i}{QE_{ref}} \cdot \frac{\nu_{ref}}{\nu_i} = \frac{QE_i}{QE_{ref}} \cdot \frac{\lambda_i}{\lambda_{ref}}$$

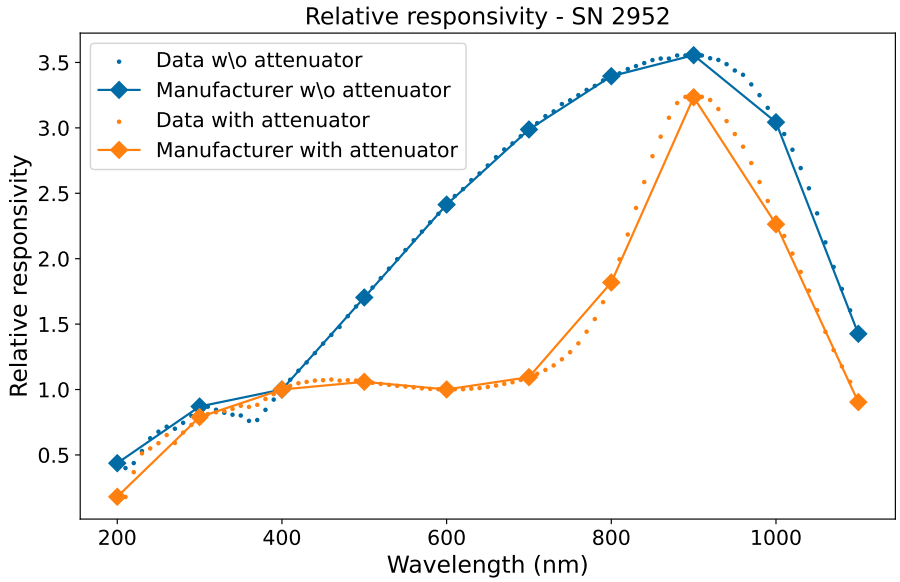

Figure 4.4: Relative responsivity for the Newport 918D-UV-OD3R powermeter, serial number 2952; reference wavelength of 405 nm.

And its values are shown in Figure 4.4 (with and without the attenuator). Here, data provided by the manufacturer are also pictured: as we can observe, these are quite scarce in quantity, as many intermediate points are missing. Since the manufacturer did not provide the interpolating function used to determine the other values, our independent measurement of the relative responsivity could compensate for this.

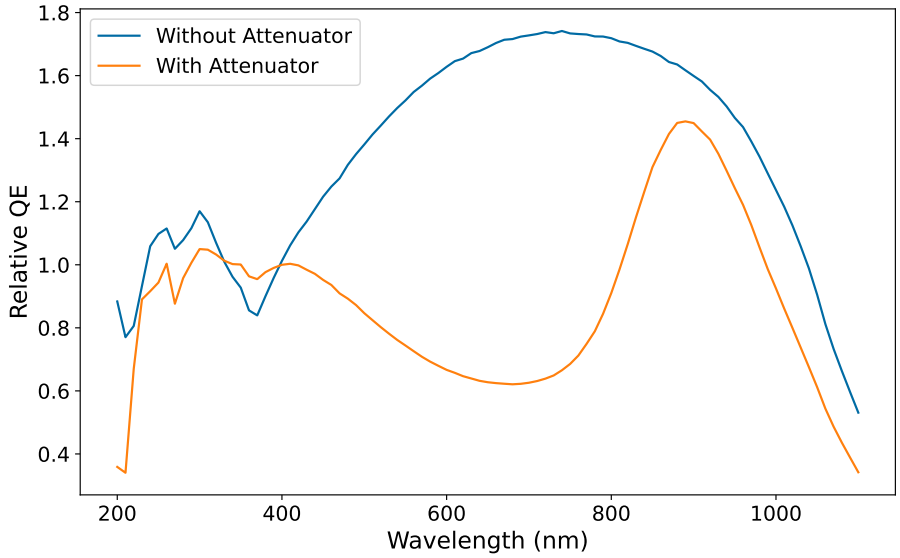

Figure 4.5: Relative quantum efficiency for the Newport 918D-UV-OD3R powermeter, serial number 2952; reference wavelength of 405 nm.

4.1.2 The Night Sky Background

The NSB subsystem consists of a Thorlabs 405 nm DC LED, a beam splitter, a powermeter, a circular top-hat diffuser of 20° and two sets of neutral density (ND) filters (Figure 4.6).

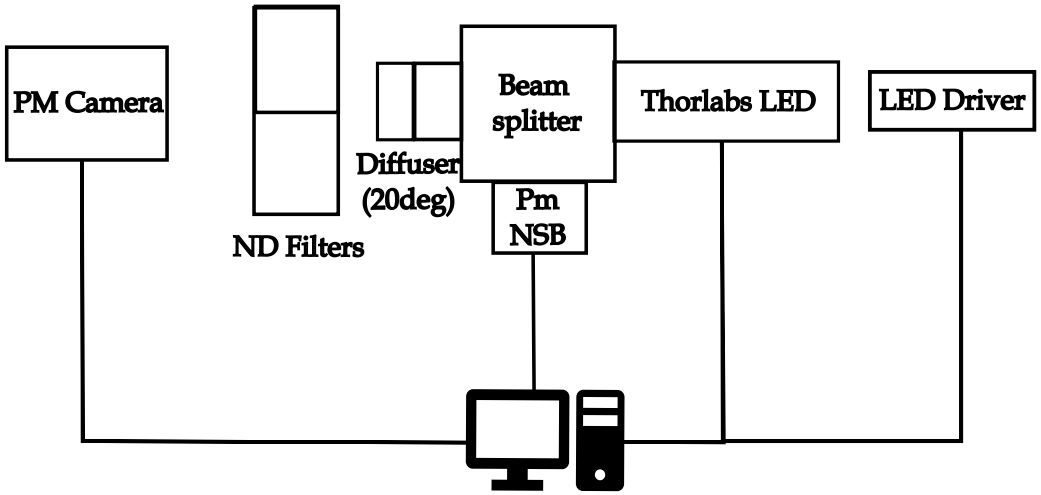

Figure 4.6: Optical set-up that mimics the Night Sky Background.

The 20° diffuser ensures that the emitted light gets diffused and uniformly illuminates the camera at 3 m distance, but it also could provide a complete illumination at closer distances, if needed.

The beam splitter directs part of the beam to the rest of the optical setup and to the detectors, while the other part goes to the powermeter. The ND filters can absorb light without changing its wavelenght and properties; here the two sets of filters provide an optical density of 2.6 and 1.3 and are called “maximum” and ”minimum” filter respectively. They can be individually applied to the output continuous light coming from the LED thanks to a motorized filter flip.

A recap of all the NSB components is reported in Table 4.1.

NSB optical setup	
LED Driver	upLED
LED Head	Thorlabs M405L4
Beam splitter	Thorlabs CCM1-BS013/M
Circular diffuser (20°)	Thorlabs ED1-C20-MD
MIN ND filter	Thorlabs NE06A + NE20A
MAX ND filter	Thorlabs NE03A + NE10A
Motorized filter flip	Thorlabs MFF101

Table 4.1: NSB optical subsystem components.

Providing a wide rate range

Since the illumination rates provided by the LED were too high, the use of the two sets of neutral density filters was required; also, the emitted light coming from the LED was continuous, while we would've liked to simulate a certain rate of NSB photons hitting the camera's SiPMs.

Then the two neutral density filters - briefly called "max" and "min" filters - are used to provide a wide range of photon rates: attenuating the photon intensity, this allows to cover a range between tens of MHz and tens of GHz, which is an interval of interest (Figure 4.7).

Indeed, for an operating SST camera, the NSB level on the CTA site is expected to be around 40 MHz photoelectrons per pixel in dark conditions [29].

An even wider range of simulated NSB signal can be exploited to observe the performance of the detector under higher NSB conditions, for example under the moonlight or when observing a brighter patch of the sky.

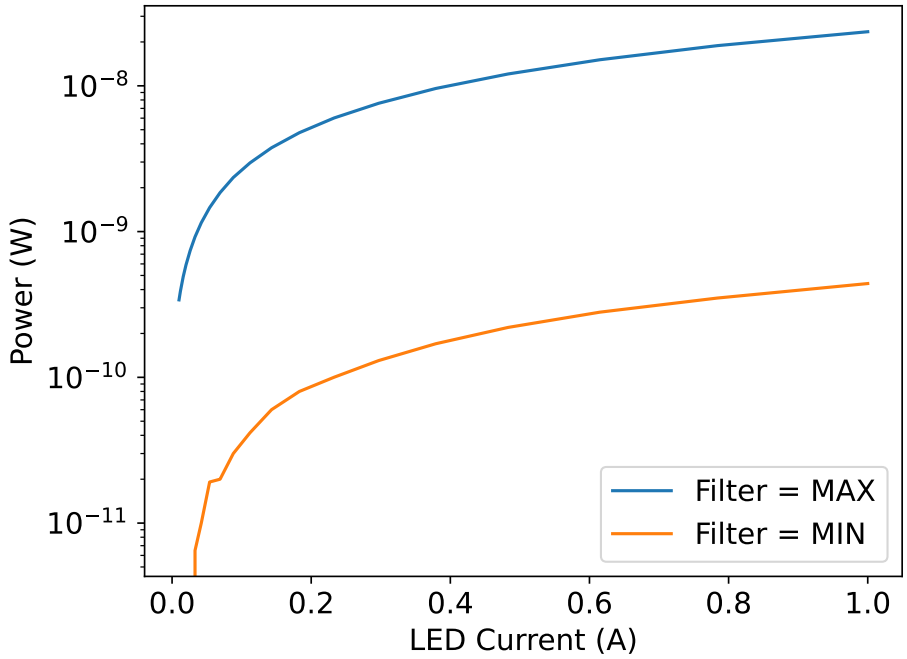

Figure 4.7: Measured power (at camera) versus current relation (semi-log scale) obtained using the 2.6 and 1.3 Neutral Density filters - called "MAX" and "MIN" respectively.

Calibration

To establish the desired NSB rate on an under-test detector, we must study the connection between the input current applied to the LED and the optical power gauged by the two powermeters, the one located at the source and the other at the camera position. Since we know how to convert the measured power in rate of photons, this would allow us to know what current value must be set in order to reach a certain goal NSB level.

This task has been achieved by performing an "intensity scan", i.e. by supplying the LED with different current values between a specific range and measuring the emitted optical power at both the source and camera positions.

The data collected was subsequently processed by converting the power measured at the camera position to a photon rate using the relation

$$R_{ph} = \frac{P}{hc} \cdot \lambda \cdot \frac{A_{\text{SiPM}}}{A_{\text{PM}}}$$

where R_{ph} is the rate of photons hitting a SiPM, P the measured power, λ the light's wavelength and A_{SiPM} and A_{PM} refer to the areas of the SiPM and a powermeter, respectively.

A linear fit can be performed on the data to determine the calibration parameters m and q required to automate the rate adjustment. In the DarkBox Manager Software, in fact, the user can set the desired NSB rate R: thanks to this calibration, the software will automatically evaluate the goal power value P needed to achieve such rate as $P = (R - q)/m$. Such power level is then obtained thanks to a feedback loop that adjusts the supplied current value until the goal power is achieved.

This calibration for the NSB source has been evaluated with the use of both sets of filters and the current results are illustrated in Figure 4.8 for the minimum and maximum filters.

We obtained the following calibration lines

$$\begin{aligned} \text{Rate} &= 6.90 \cdot 10^3 \cdot \text{Power} - 0.02 \text{ GHz} && \text{Minimum filter} \\ \text{Rate} &= 1.33 \cdot 10^5 \cdot \text{Power} - 12.13 \text{ MHz} && \text{Maximum filter} \end{aligned}$$

Ensuring constant LED emission

The powermeter placed at source position not only allows a continuous monitoring of light emission, but also ensures a stable LED emission thanks to a feedback loop implemented in the managing software. Such a loop runs in a thread, constantly measuring the emitted power and comparing it with a predefined goal level; whenever the measured and goal levels differ by more than a set amount, the procedure iteratively adjusts the current supplied to the LED until the goal level is reached. This method is an indirect way of ensuring a stable LED emission without having to monitor the temperature in the facility, as the LED emission is sensitive to temperature variations.

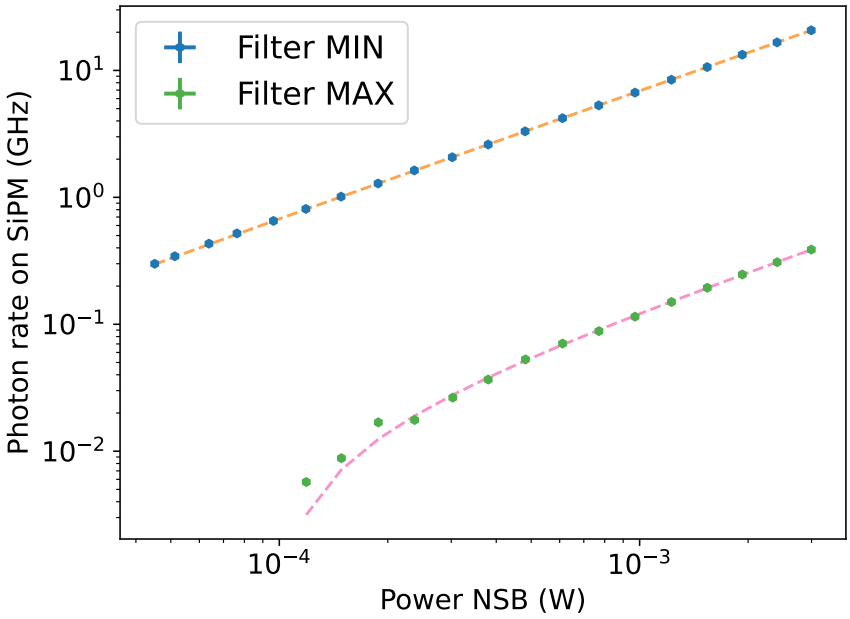

Figure 4.8: Photon rate as a function of the measured NSB power with the use of the MIN and MAX filters, together with the calibration lines (log-log scale).

4.1.3 Cherenkov light

The Cherenkov light signal is simulated by a UV Laser (PicoQuant LSH Laser head) of 405 nm of wavelength, controlled by a laser driver (PicoQuant PDL 800-D) which is externally triggered by a pulse generator.

The optical setup consists also of a filter wheel, a beam splitter, a beam expander and two circular diffusers and is summed up in Table 4.2.

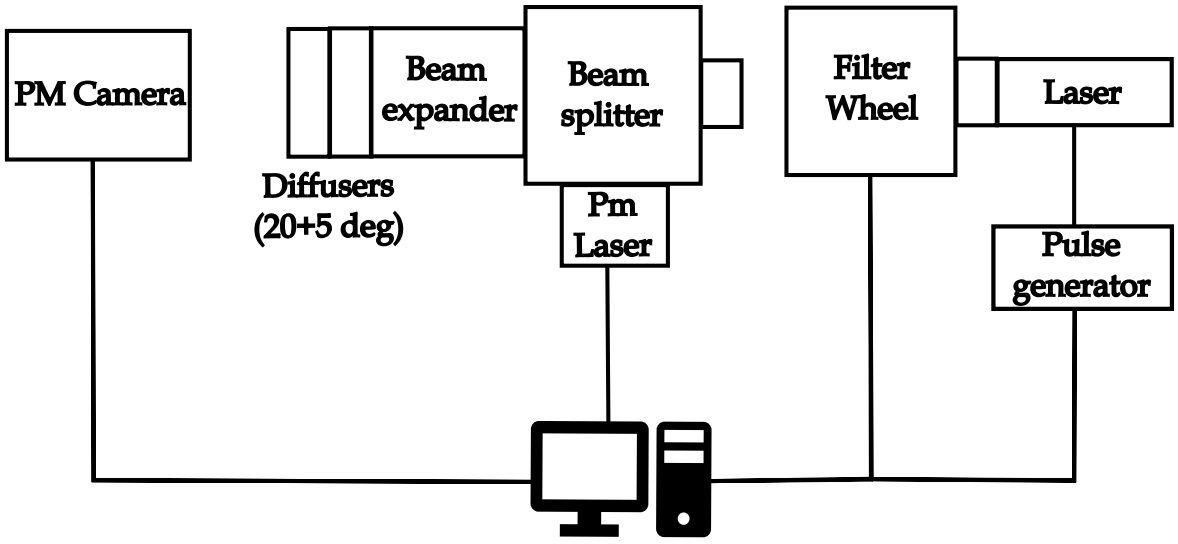

Figure 4.9: Schematics of the laser setup.

As previously mentioned, the goal of an SST - and of a IACT in general - is to capture Cherenkov light events generated by the particles of a γ-ray induced EAS: to do so, the chosen devices are SiPMs, which can count the incoming photons.

Then, the need to simulate our Cherenkov signal in terms of *how many* photons hit the device under test in the commissioning facility appears quite reasonable: to do so, we needed various optical filters that could allow us to attenuate the laser light and provide a certain range of photons, ideally between one single photon to several thousands.

This choice is based on the need to work at a fixed laser intensity: in fact, one could obtain different illumination levels simply by varying the latter. However, this is not possible, mainly for two reasons: firstly, the laser cannot be remotely controlled and, more importantly, changing the intensity would require a warm-up time for the laser at each adjustment. This would introduce an additional source of uncertainty in the experimental setup and prolong the timescales.

Then, the use of optical filters is necessary. Although it is possible to use a series of different single ND filters mounted on several wheels (as in the Calibration Box for the LSTs [41]), here we chose to use one single object, briefly called *filter wheel*.

Cherenkov optical setup	
Laser driver	PicoQuant PDL 800-D
Laser head	PicoQuant LDH-P-C-405M
Filter wheel	Thorlabs NDC-50C-4M
Beam splitter	Thorlabs CCM1-BS013/M
Beam expander	Thorlabs BE03-UVB - 3X UVFS
Circular diffusers (5°, 20°)	Thorlabs ED1-C20-MD

Table 4.2: Laser optical subsystem components.

Filter wheel

The filter wheel (Figure 4.10) is a circular, continuously variable Neutral Density filter that allows to attenuate light over four orders of magnitude [42]. Specifically, the optical density range (OD) lies between 0.04 and 4.0: optical density is strictly related to the attenuation of a filter and allows to quantify how much the filter reduces the optical power of an incident light; it is also related to the filter's *transmission* as

$$OD = \log\left(\frac{1}{T}\right) \quad \Rightarrow \quad T = 10^{-OD} \tag{4.3}$$

The values for the transmission T lie between 0 and 1; choosing a ND filter with a higher OD corresponds to reduced light transmission and increased reflection of incoming light, while a filter with a lower OD results in greater light transmission and reduced reflection.

The filter wheel, being a continuously variable filter, provides potentially infinite attenuation values, in contrast to the optical components selected for the previously mentioned LST Calibration Box.

The various levels of transmission are attained by rotating the device, which is remotely controlled through Ethernet. This rotation is carried out using a 12-bit motor step, which requires us to define 4096 DAC filter wheel positions that provide us 4096 levels of transmission across the filter wheel.

Furthermore, since the filter wheel attenuation varies over four orders of magnitude, the laser beam should hit the filter wheel in a reasonably small point, in order to obtain a uniform attenuation value within the beam.

Also, the communication with the device is implemented in the DarkBox Manager Software.

Figure 4.10: Thorlabs Filter Wheel.

The filter wheel has been studied in terms of transmission and number of photons hitting the camera pixels at certain pulse rates of interest for every different transmission value.

We are particularly interested in knowing very well the relationship between the transmission provided by the filter wheel and the number of photons hitting the camera at the working rate of 600 Hz.

The study of the filter wheel in this sense was carried out by measuring the power emitted by the source with the powermeters placed at two different positions, i.e. the laser position and the camera position, while setting the laser intensity at a fixed value via the laser driver.

Data taken at source position allowed us to evaluate the transmission as

$$T = \frac{P}{P_{max}}. \tag{4.4}$$

where P and P_{max} are the measured power and the maximum power values, respectively.

The variation of this quantity T is shown in Figure 4.11 for 600 Hz and 1 MHz: here we can observe that the transmission increases along with the position - i.e. with the filter wheel's rotation, and that it reaches a "saturation point" when the wheel is basically an open sector of transmission equal to 1.

The lowest position (0 DAC) has been chosen in order to lie in this saturation sector.

Additionally, we can observe that this filter wheel provides a minimum transmission of $1.86 \cdot 10^{-5}$ and a maximum of 1.

All data in this study have been measured at a pulse rate of 1 MHz: this choice is a consequence of the fact that with a pulse rate of 600 Hz, the optical power reaching the powermeter at 3 m of distance from the source goes below the minimum measurable power of the device, which is equal to 20 pW [43].

A pulse rate of 1 MHz is a good choice in order to obtain a reasonable quantity of points along the filter wheel's optical range at camera distance; much higher rates, in fact, are not suitable, even if it may first appear as a first natural solution to the issue. In fact, higher rates cause the powermeter at the laser position to saturate: this means that the

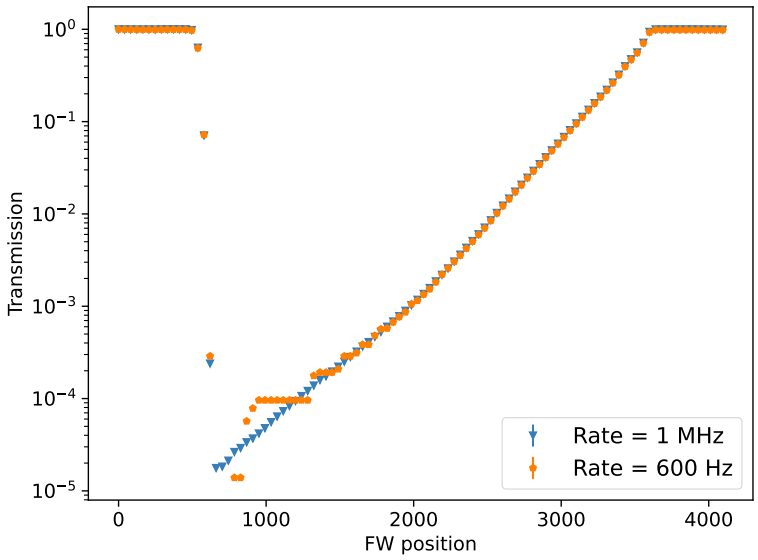

Figure 4.11: Filter wheel transmission evaluated at different pulse rates.

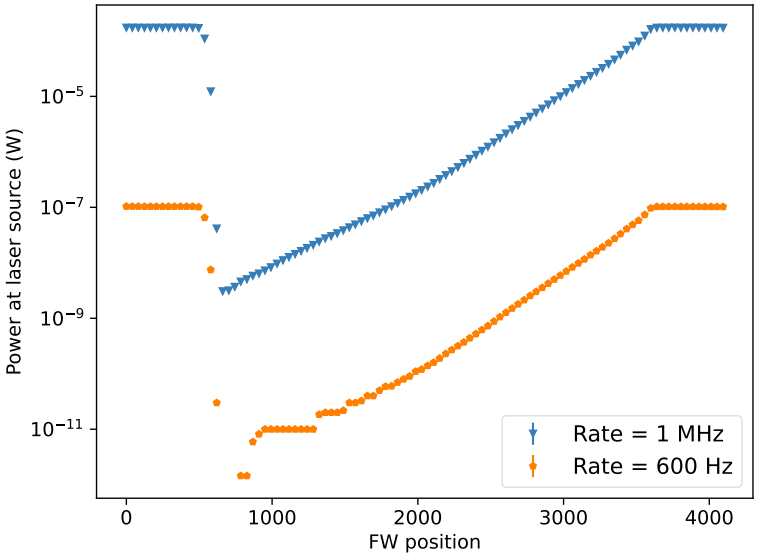

Figure 4.12: Measured power at source (laser) at different rates.

emitted power is greater than the maximum value measurable by the powermeter, which equals 0.3 mW.

Therefore, we chose to start our measurements with a pulse rate of 1 MHz and evaluated the filter wheel's transmission with those; the evaluated value are shown in Figure 4.13.

The basic idea of the analysis was then performing a *cross-calibration* using both data at 1 MHz and 600 Hz.

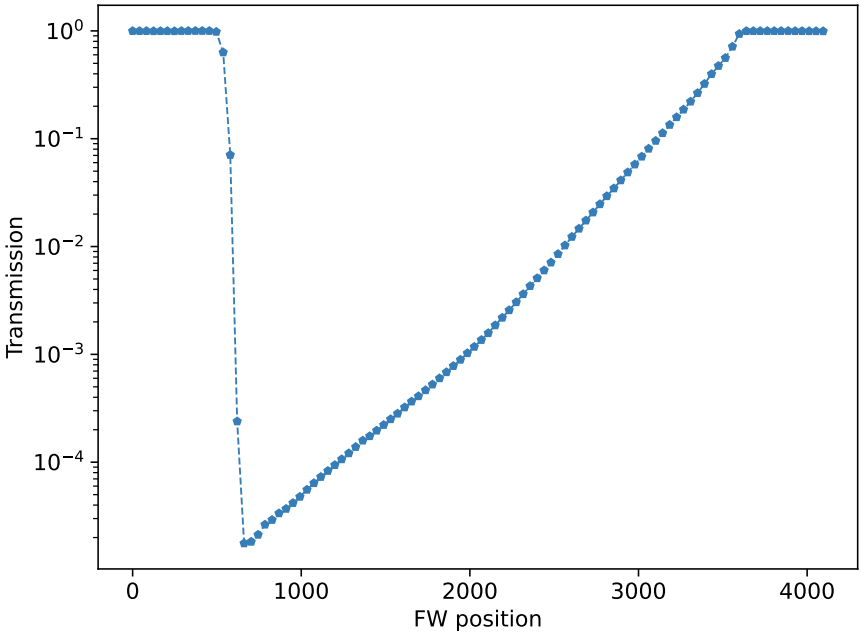

Figure 4.13: Transmission values evaluated with 1 MHz data.

The next step in finding the filter wheel calibration is to evaluate the expected number of photons via

$$n_{ph}^{expected} = \overline{k} \cdot T \tag{4.5}$$

where T is the transmission and $\overline{k}$ is a scaling factor obtained averaging the values k_i

$$k_i = \frac{n_{ph}^i}{T^i} \tag{4.6}$$

over the filter wheel positions (i) where both powermeters - at camera and source positions - are able to measure light, i.e. where the emitted power is greater than the sensitivity of the instrument (20 pW).

The number of photons n_{ph}^i hitting one SiPM for each filter wheel step is evaluated from the measured power through the relation

$$n_{ph}^i = \frac{P}{hc} \cdot \lambda \cdot \frac{1}{r} \cdot \frac{A_{SiPM}}{A_{PM}}$$

where P is the measure power, λ the wavelength of incoming light, r the rate and A_{SiPM}, A_{PM} are the areas of the Silicon Photomultiplier and the powermeter, respectively; the ratio between these two allows to compensate for the fact that our Silicon Photomultipliers and powermeters have a different sensitive area.

This relation then converts the power measured at the powermeter position to the number of photons hitting the SiPM of the camera for each laser pulse, if the powermeter and the camera are at the same distance from the uniform light source.

At this point, we would like to know the expected number of photons at 600 Hz: this can be done by taking the same data with a set pulse rate of 600 Hz and evaluating the

scaling factor between measurements at the two different rates made at the source position. Referring more generally and briefly to 1 MHz data as "high" rate data and to 600 Hz data as "low" rate data, we obtain

$$\left[n_{ph}^{low}\right]_{Camera} = \left[\frac{n_{ph}^{low}}{n_{ph}^{high}}\right]_{Laser} \cdot \left[n_{ph}^{high}\right]_{Camera}$$

Finally, by interpolating the data, we can determine the corresponding number of photons at camera position and rate 600 Hz over all the filter wheel positions that yield at least one single photon by interpolating the data.

The result is shown in Figure 4.14: the dynamic range provided by the filter wheel falls between 1 photons and 3100 photons, covering three orders of magnitude. If a broader range is required, we must move closer to the laser source.

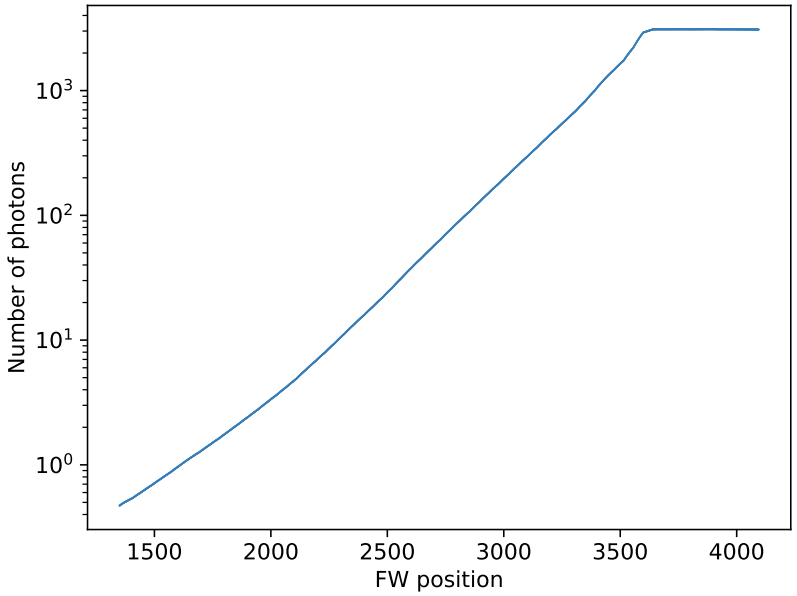

Figure 4.14: Final result of the filter wheel and laser calibration.

Procedure automation Over the next few years, 40 SST cameras will be assembled and successively tested and commissioned at MPIK. Thus, it is crucial that that the commissioning facility's performance and experimental conditions remain constant and consistently well known.

For this reason, such calibration procedure for the filter wheel had to be automated, so that it could be regularly performed by any user of the facility; therefore, such procedure has been automated in the DarkBox Manager Software (briefly described in Section 4.1.5).

Calibration fast check and PDE estimate In order to quickly test the calibration just obtained, a Silicon Photomultiplier (Onsemi's J-Series 60035) was positioned at the camera location. Measurements were taken at random filter wheel positions using a laser pulse rate of 600 Hz, evaluating the corresponding number of photons both for the SiPM and for the powermeter at camera position.

Such measurements were performed by externally triggering the sensor, i.e. connecting the second channel of the pulse generator that triggers the laser source to the device, and reading its output with an oscilloscope, therefore measuring the peak amplitude of the signal.

The corresponding measured number of photons can be evaluated as

$$n_{photons} = \frac{\text{Amplitude (mV)}}{\text{SPE (mV)} \cdot \text{PDE}} \cdot (1 - \text{CT})$$

where SPE is the signal amplitude corresponding to one photoelectron, PDE is the photodetection efficiency and CT is the crosstalk. These parameters were previously obtained as PDE $= 0.5$, SPE $= 0.19\ mV$, CT $= 0.25$.

Given that the two measures were very similar, this quick measurement allowed us to also test the possibility to evaluate the PDE of a SiPM in the facility, knowing its crosstalk and SPE and measuring the signal amplitudes when illuminating the sensor with a certain level of light.

In fact, from the amplitude values we can evaluate the measured number of photoelectrons as

$$n_{pe,measured} = \frac{\text{Amplitude (mV)}}{\text{SPE (mV)}} \cdot (1 - \text{CT})$$

This value can be used to find the expected number of photoelectrons in the following equation

$$n_{pe,expected} = n_{photons} \cdot \text{PDE} = n_{cells,tot} \cdot \ln\left(1 - \frac{n_{pe,measured}}{n_{cells,tot}}\right)$$

which also takes into account potential saturation effects [35].

The PDE is then given by

$$\text{PDE} = \frac{n_{pe,expected}}{n_{photons}}$$

where $n_{photons}$ is the number of photons supplied by the laser source, which we know thanks to the filter wheel calibration.

The values obtained are shown in Figure 4.15 and have a mean PDE of (48.13 ± 0.4) %, which is very close to the value obtained during previous measurements. Indeed, it is worth keeping in mind that the PDE of a SiPM can vary in time due to prolonged use and handling of the device.

Hence, this quick evaluation, although it is only an estimate, shows that the commissioning facility can be used to quickly evaluate the PDE of a device, for example for all 2048 SiPMs of an SST camera. In this case, such evaluation could be performed for all pixels at once, thanks to the uniform laser beam in the facility.

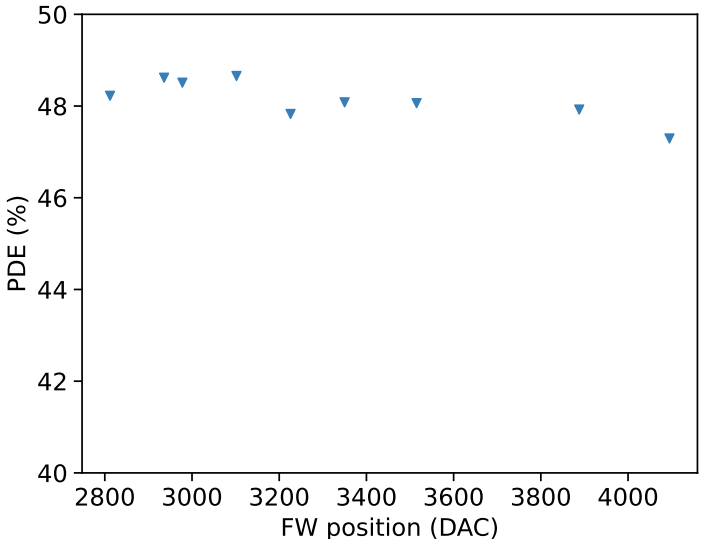

Figure 4.15: Photon Detection Efficiency values obtained.

4.1.4 Study of the laser beam

As mentioned above, the laser beam must meet certain uniformity requirements: in fact, while for many measurements it is possible to apply corrections *a posteriori* in case of a non-uniform beam (e.g. for a dynamic range measurement), for some tests it is crucial to have a uniform light incident on the camera; for example, in order to test the trigger performance of the whole camera, it is necessary to have an incoming signal that is the same for each pixel. Having a uniform beam is then essential to ensure this.

Figure 4.16: UR5 robot arm in the DarkBox.

To verify this uniformity requirements, we used a UR5 robot arm (Figure 4.16) with a powermeter installed on its tip to perform two-dimensional scans of the laser beam.

In order to achieve the uniformity goal, many different optical combinations were tried and each one of them has been tested at several distances from the laser source, mainly at 1 m, 2 m and 3 m. The main scenarios tried in order to reach the required uniformity at 3 m are summarised in Table 4.3.

Many other trials at different distances were also attempted to eliminate undesired reflections of light in the setup; for example, we tried inserting different apertures of varying diameter on some optical components, like the beam splitter, or also covered the Robot Arm and its support with black cloth to avoid possible reflections (however these were not actually detected).

Diffusers (circular top-hat)	Beam expander	Additional components	Beam uniformity
20°	No	Aperture at beam splitter (7 mm diameter)	92.6%
20°	Yes	No	95.1%
10° + 5°	Yes	No	96.3%
20° + 5°	Yes	No	98.8%

Table 4.3: Robot Arm scans performed at 3 m distance from the laser source.

Finally, the chosen combination consisted of the following components: one beam expander and two circular top-hat diffusers (20° + 5°). This combination gives a beam uniformity of 98.8% at a distance of 3 m from the source.

Considering a region of 0.15 m, at a distance of 2 m, the beam's uniformity is 97.5%, decreasing to 97.4% at 1 m; this uniformity, which doesn't meet the collaboration's requirements, has raised the possibility of trying to describe the laser beam at 1 m in some

way. In fact, there might be some measurements and tests that could be carried out at such a short distance from the source: then we would like to know if it is possible to describe the beam, in order to have a useful tool for offline corrections on data.

Figure 4.17 shows the scans performed with the Robot Arm at three different distances from the source.

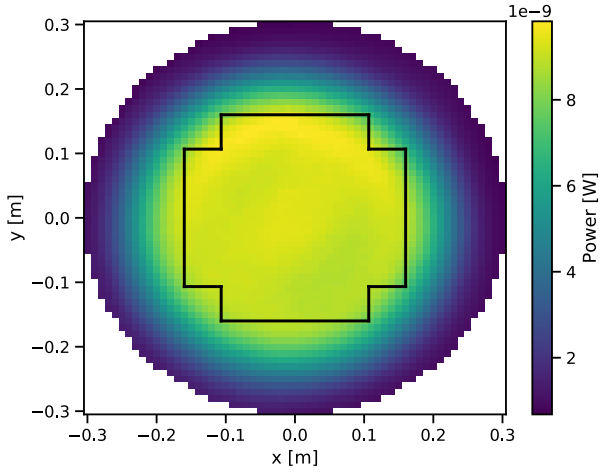

(a) 2D scan at 1 m from source.

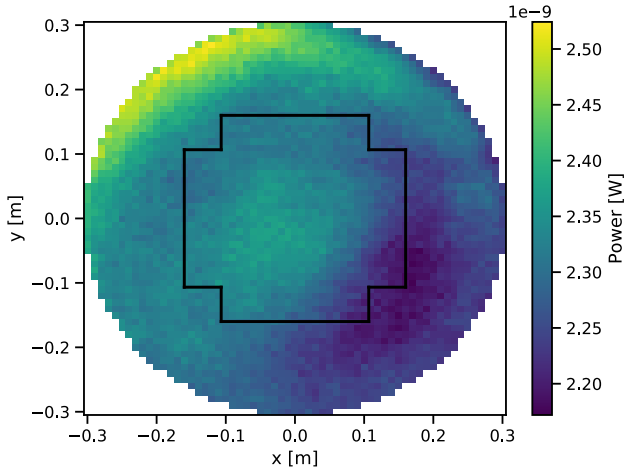

(b) 2D scan at 2 m from source.

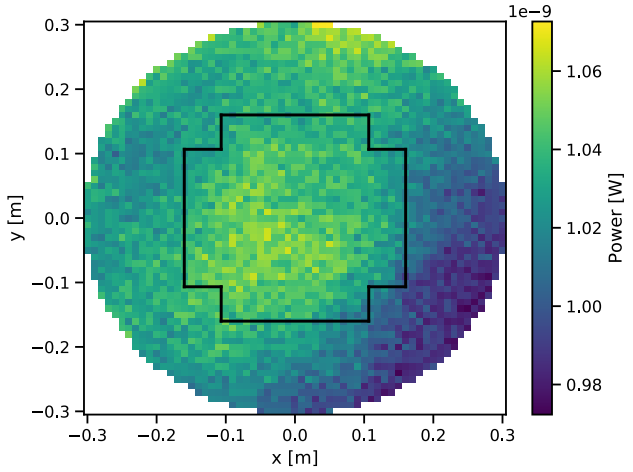

(c) 2D scan at 3 m from source.

Figure 4.17: Robot arm scans of laser beam; the SST camera outline is also depicted.

Spherical correction In order to carry out the beam model analysis, all power measurements taken during the 2D scans with the Robot Arm have been corrected offline to compensate for the fact that such scans were performed on a plane rather than a sphere. In fact, the resulting light beam emitted by the optical setup should be uniform *along the sphere*.

Such correction has been evaluated as a geometrical factor, as the ratio between the actual sensor size - 10.3 mm - and the size the sensor should have in order to measure an equal amount of light subtended by the same arc of circumference.

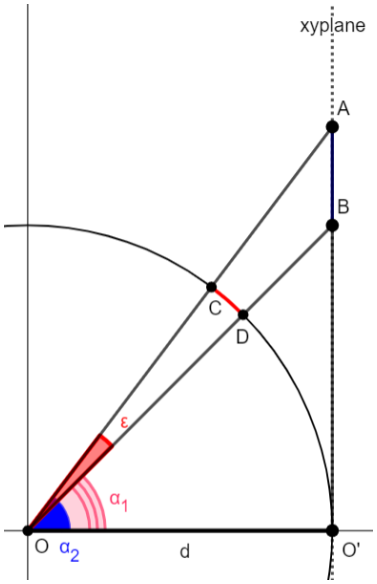

Figure 4.18: Schematics of spherical correction.

Using Figure 4.18 as a reference, such correction is represented by two factors that take into account the correction along the x and y axis respectively, evaluated as

$$R_{x,y} = \frac{d[\tan(\alpha_{1x,y} + \epsilon) - \tan(\alpha_{1x,y})]}{10.3 \text{ mm}}$$

with ϵ and $\alpha_{1x,y}$ evaluated as

$$\epsilon = \alpha_2 - \alpha_1 = (10.3 \cdot 10^{-3} \text{ m})/d$$

$$\alpha_{1x} = \arctan\left[\frac{x - x_0}{d}\right], \qquad \alpha_{1y} = \arctan\left[\frac{y - y_0}{d}\right]$$

where x and y are the sensor position coordinates at each scan step.

The correction factor values are shown in Figure 4.19: as we can observe, the variation between the values for the measured power before and after applying this correction goes from a minimum of 0.005% to a maximum of 10.4%.

Particularly, we have bigger variation values in the peripheral areas of the scanned region.

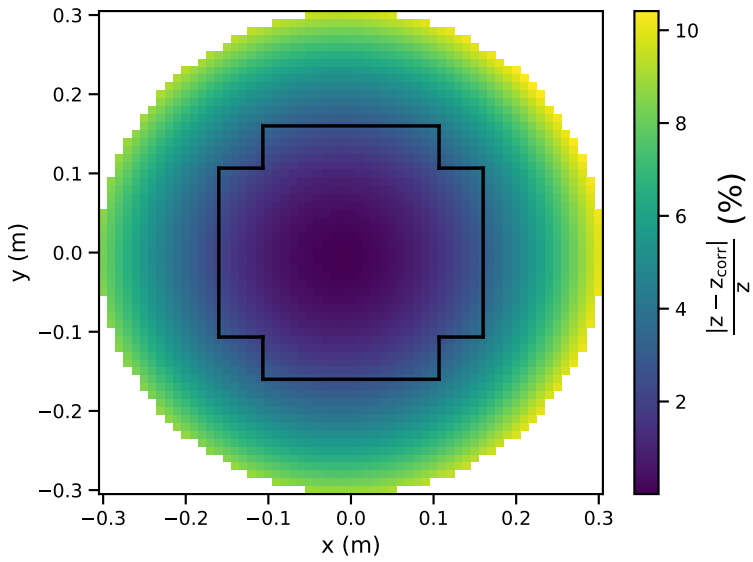

Figure 4.19: Variation between the measured and corrected power values as percentage, along the scanned region.

Beam model

The laser used in the facility is expected to have a circular and Gaussian-shaped beam profile according to the manufacturer's specifications.

Hence, when going to take a "slice" of the data along the x and y axis, we expected a Gaussian distribution, at first thought; here, by "taking a slice of data" we imply plotting the power's distribution along a particular x or y value.

For instance, the slices along $x = 0$ and $y = 0$ are shown in Figure 4.20: it is very clear that the distributions are not Gaussian at all, or rather, they seem to present a Gaussian fall but a flat top.

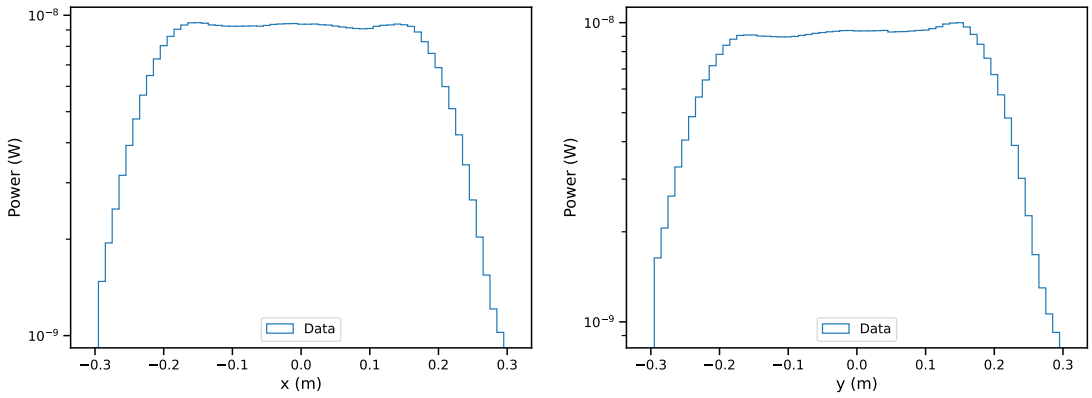

(a) (b)

Figure 4.20: Slices of the measured power along the x (a) and y axis (b).

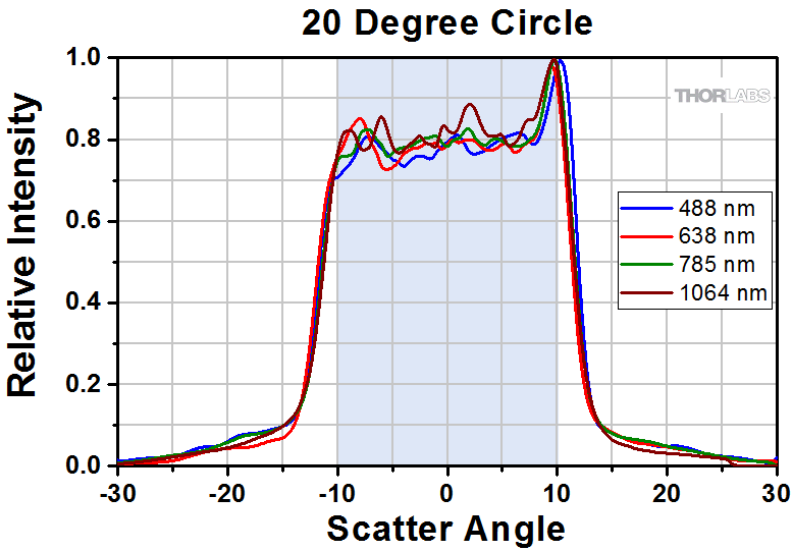

Figure 4.21: Intensity through the center of the beam profile when illuminating the diffuser with a collimated beam of different wavelengths [42].

Indeed, as we have previously seen in Section 4.1.3, the laser setup is made of several different optical components: particularly, we used two diffusers whose are *circular top-hat* diffusers, i.e. they should apply a top-hat function to the beam profile while shaping it as a circle. While at 2 m and 3 m distance this effect is not visible, it gets significant when getting closer to the source.

Additionally, the distributions in Figure 4.20 also appear slightly asymmetrical: this can be explained by the fact that the employed optical components do not uniformly diffuse the incident beam, but have an angular dependence, as shown in Figure 4.21.

Then, our aim was to describe a flat Gaussian-like beam profile: there exists a higher order gaussian distribution, called a *supergaussian*, which fits the described experimental case [44]. This particular function is described in one dimension by

$$f(x) = A \cdot exp\left[-\left[\frac{1}{2}\left(\frac{x - x_0}{\sigma}\right)^2\right]^n\right] \tag{4.7}$$

It is easily extended to the two-dimensional domain

$$f(x,y) = A \cdot exp\left[-\left[\frac{1}{2}\left(\frac{x - x_0}{\sigma_x}\right)^2 + \frac{1}{2}\left(\frac{y - y_0}{\sigma_y}\right)^2\right]^n\right] \tag{4.8}$$

and reduces to a standard gaussian distribution for n = 1. The distribution with different parameter values is shown in Figure 4.22, together with the x and y slices of data already shown.

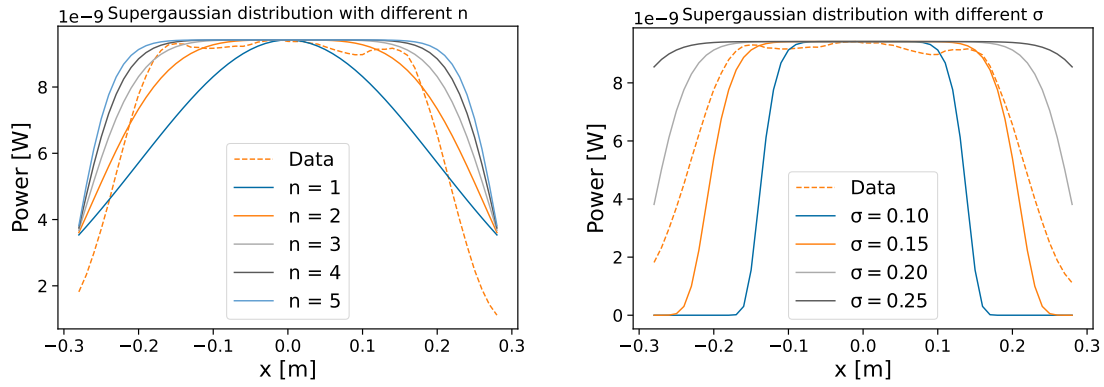

Figure 4.22: Example of a supergaussian function with varying order **n** and standard deviation σ. Different functions are compared to a slice of data from a two-dimensional scan of the laser beam.

Here, we are particularly interested in studying the distribution of the emitted power along the y = 0 and x = 0 slices respectively, because by observing and fitting on these slices we can also immediately see if the laser beam is no longer centered.

Therefore, a first fit on one-dimensional data distributions has been performed: data consisted in the (x,y) and power values, while the function's parameters A, σ_x, σ_y and n were left free. Results are shown in Figure 4.23 and are described by the following distributions

$$P(x) = 9.371 \cdot 10^{-9}\ [\mathrm{W}]\ \cdot\ exp\left[-\left[\frac{1}{2}\left(\frac{x - 0.500 \cdot 10^{-9}\ [\mathrm{m}]}{0.175\ [\mathrm{m}]}\right)^2\right]^{3.101}\right]$$

$$P(y) = 9.372 \cdot 10^{-9}\ [\mathrm{W}]\ \cdot\ exp\left[-\left[\frac{1}{2}\left(\frac{y - 0.\ [\mathrm{m}]}{0.174\ [\mathrm{m}]}\right)^2\right]^{3.040}\right]$$

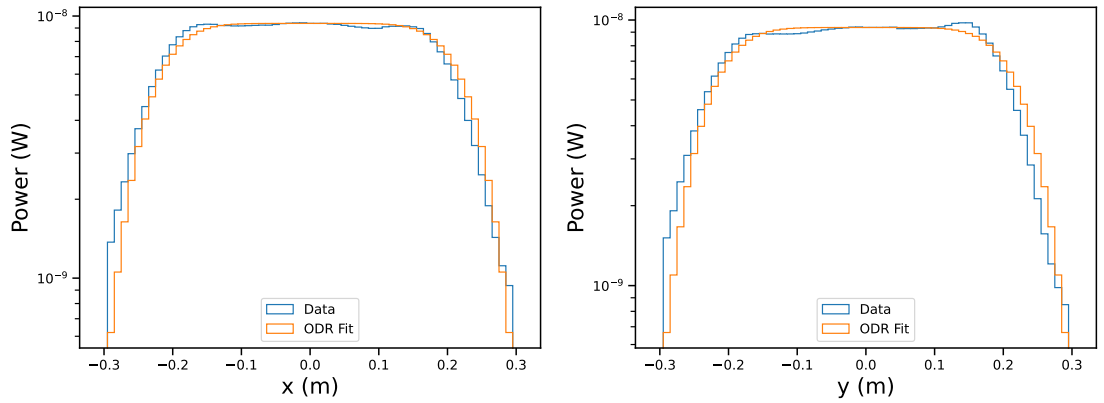

(a) (b)

Figure 4.23: First fit with a supergaussian on the one-dimensional power distribution (x and y slices, (a) and (b).

Since the result of this first fit looked very promising, we proceeded with a two-dimensional fit using the supergaussian distribution defined above (Equation 4.8), leaving the same free parameters and setting as initial parameters the values from the one dimensional fits just obtained;

The result is shown in Figure 4.24, with a distribution described as the following

$$P(x,y) = 1.010 \cdot 10^{-8}\ [\mathrm{W}]\ \cdot\ exp\left[-\left[\frac{1}{2}\left(\frac{x+0.008\ [\mathrm{m}]}{0.174\ [\mathrm{m}]}\right)^2 + \frac{1}{2}\left(\frac{y+0.102\ [\mathrm{m}]}{0.173\ [\mathrm{m}]}\right)^2\right]^{2.17}\right]$$

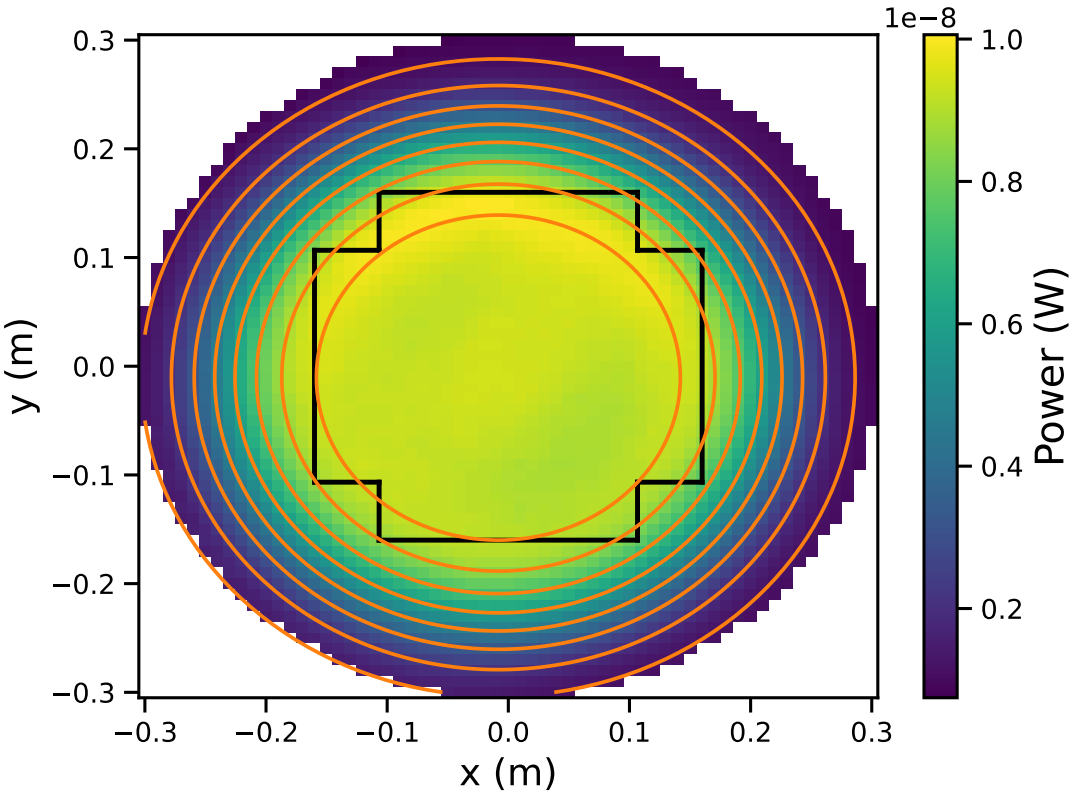

Figure 4.24: Fit with a supergaussian on the two-dimensional power distribution.

This fit was also satisfactory, and the parameters obtained ensure us that the laser beam is reasonably centered with respect to the center of the detector: in fact we have $x_0 = -8.19 \pm 0.18$ mm and $y_0 = -10.2 \pm 0.17$ mm.

To ensure that the fit performed well over the entire scanned area and that there were no "problematic" spots or regions, we evaluated the ratio between the measured power over the reconstructed one via the fit parameters and function, as

$$\eta = \frac{z_{true}}{z_{rec}}$$

Its values in the x-y plane are shown in Figure 4.25: we can see that there are values very close to unity in the whole area, while there are no values too high - or too low - in the region of interest.

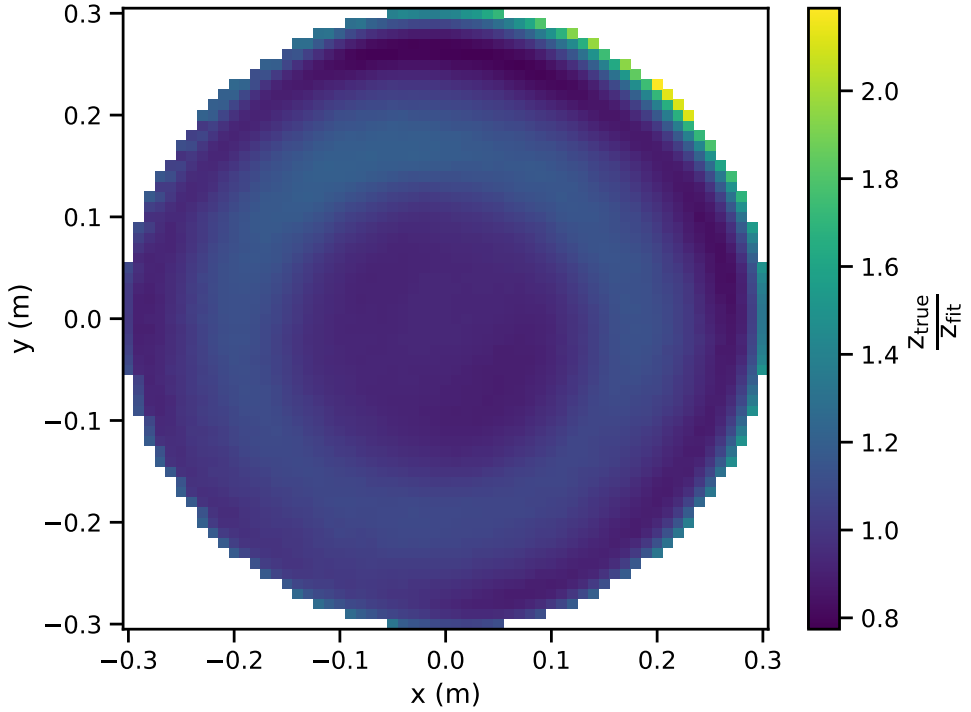

Figure 4.25: Map of $\eta = z_{true}/z_{fit}$.

4.1.5 DarkBox Manager

The facility is completely remotely controlled by an implemented software, called DarkBox Manager (DBM), that handles the communication with all devices and components. Particularly, each experimental sub-setup is managed by a DBM subsystem.

For example, the NSB, the laser source, the pulse generator (trigger), the powermeter placed at camera position, the rotational stage and the Robot Arm are all different subsystems. The laser subsystem, for instance, handles the powermeter at laser position, the filter wheel and its calibration; the trigger subsystem sets the pulse rate and trigger delay, while the Robot Arm subsystem allows to perform the beam scans with the desired parameters, such as the size and step of the scan.

An "environment" subsystem is also implemented, in order to monitor the temperature and relative humidity in the facility.

4.2 CHEC-S in the Commissioning Facility

Once the optical setup in the validation facility had been fully characterized, we would've liked to "test" it with a device different from the powermeters.

Of course, a detector similar to the next SST Cameras would've been preferable: for this purpose we had CHEC-S, the SST camera prototype, at MPIK laboratories; this prototype was first commissioned in 2019 on Mount Etna, Sicily [27]. Employing such a device, although it hadn't been used since its commissioning, allows to try out the DarkBox and to test working with a full SST camera inside the facility.

4.2.1 Experimental set-up

CHEC-S was then placed inside the facility on the rotational stage, along with its external power supply, as shown in Figure 4.26.

It was connected to an external chiller via two cables and to the pulse generator that manages the laser source for external triggering. Data are transferred to the DarkBox computer via an optical fibre.

The work on CHEC-S was based on fundamental small tasks, such as:

A. Adjusting the trigger delay by identifying the signal peak in each camera pixel

B. Taking pedestal data

C. Taking data, for example conducting a dynamic range scan using the filter wheel, i.e. illuminating the camera with different light levels

D. Updating the HV settings by running a gain matching script and evaluating the current "camera status".

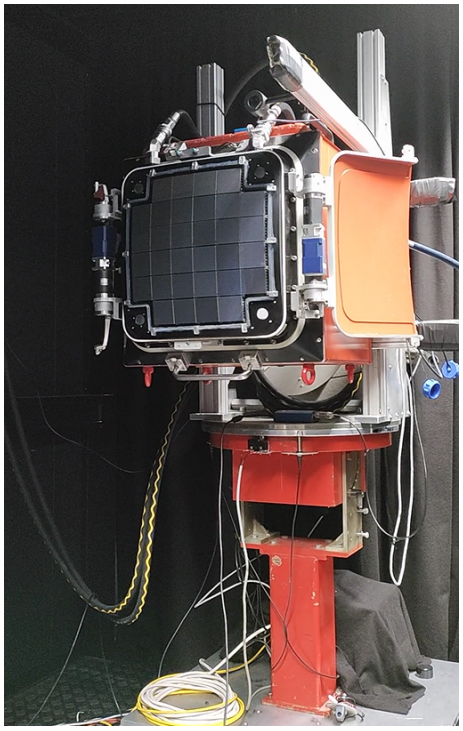

Figure 4.26: CHEC-S in the facility.

4.2.2 Trigger delay study

A crucial initial step in working with a detector is ensuring that the signal of interest is contained within the acquisition window of the device.

For CHEC-S specifically, connecting the device to the experimental apparatus alone did not guarantee the desired outcome. In fact, the pulse generator controls the laser source, meaning that the emission of light is triggered by the generator. Additionally, a second channel of the generator is used to trigger the camera. As time delays given by the cables and the response times differ between the laser and camera systems, we need

to scan over a range of time delays between the two pulse generator channels in order to find the correct value required for the signal to be within the acquisition window.

Hence, one of the first steps in working with CHEC-S was determining the optimal time delay between the two channels. This was achieved through a "delay scan", where the camera recorded data multiple times, each time with a different delay between the channel triggering the laser and the one triggering the camera.

Such scan was implemented via a python script and managed all the required experimental setup, i.e. the pulse generator, the laser and the camera, and then executed a brief data analysis on the raw files applying the pedestal calibration.

Pedestal data represents the electronic background noise present in a detector even in the absence of physical signals; such run was taken as a normal data run, but with the camera lids completely closed and no light sources inside the facility.

With the calibrated data, the python script then proceeded to plot one signal for each run. Potentially, this could be done for any pixel of the camera.

By displaying the obtained plots at each trigger delay, we were able to effectively see the signal coming into the acquisition window as the right delay value approached. Particularly, our acquisition window extends from 0 ns to 128 ns.

An example of the obtained signal waveform is shown in Figure 4.27, with a trigger delay of 320 ns.

This procedure can be easily repeated using the same script whenever the experimental setup is modified.

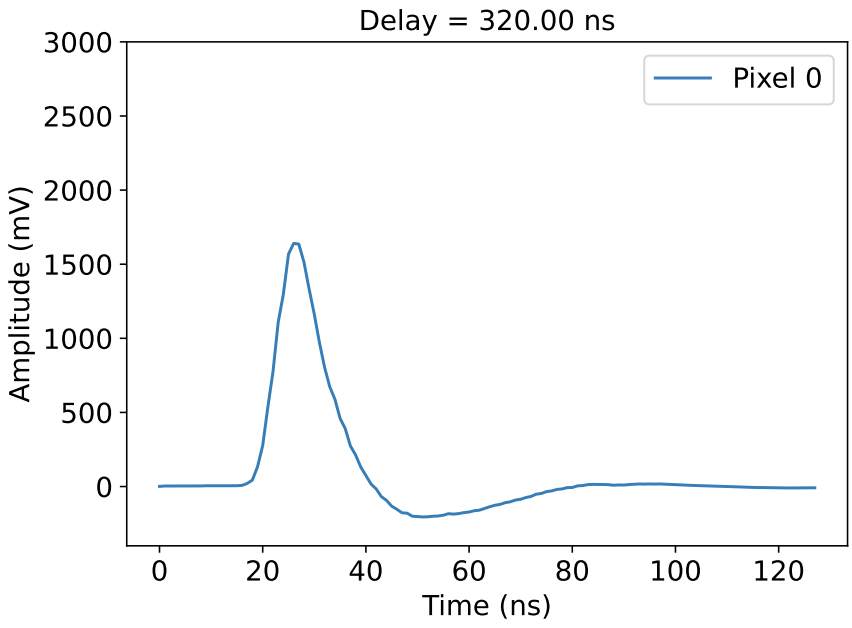

Figure 4.27: Waveform signal in pixel n. 0 with a set trigger delay of 320 ns.

To gain insight into the overall performance of the camera at the set trigger delay, a brief "waveform analysis" was conducted.

The aim was to examine the peak signal time and identify any anomalies within the pixels, including those with delayed or early peak signals in comparison to the average time.

Figure 4.28 shows the peak signal time of all 2048 pixels, divided into the 32 modules; the same values are displayed as a map in Figure 4.29. As we can observe, the camera seems to be clearly divided in half, with one half (modules 16-31) slightly faster than the other one (modules 0-15). Furthermore, there is also a difference in the peak time values between the ASICs in the single camera modules.

While the latter was already known during CHEC-S' commissioning, the difference between one half of the camera and the other is quite new, indicating some potential damage occurring after 2019.

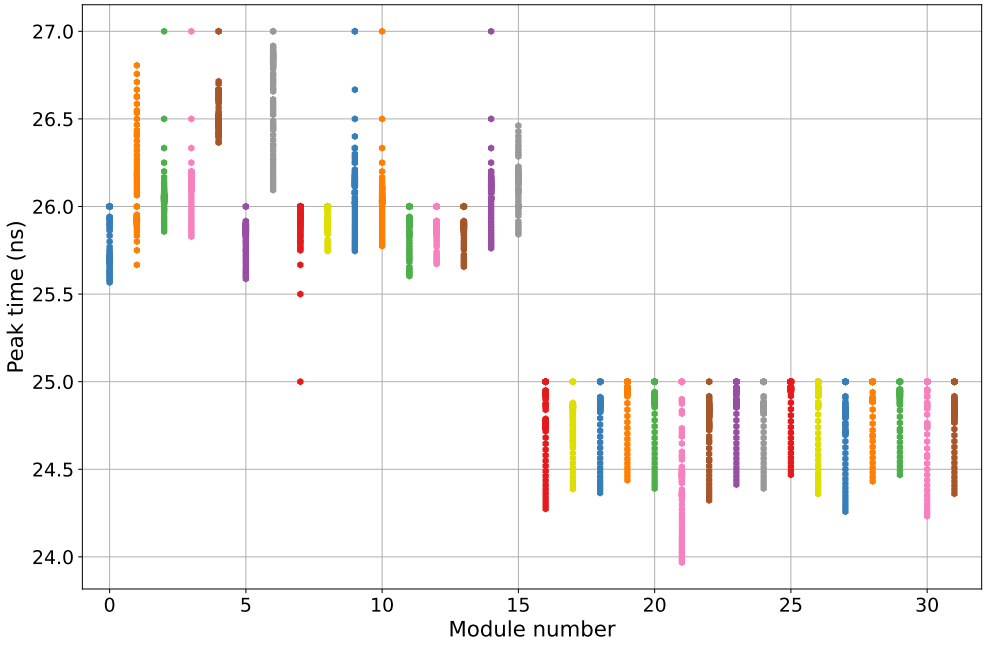

Figure 4.28: Peak time values for all pixels, divided by module.

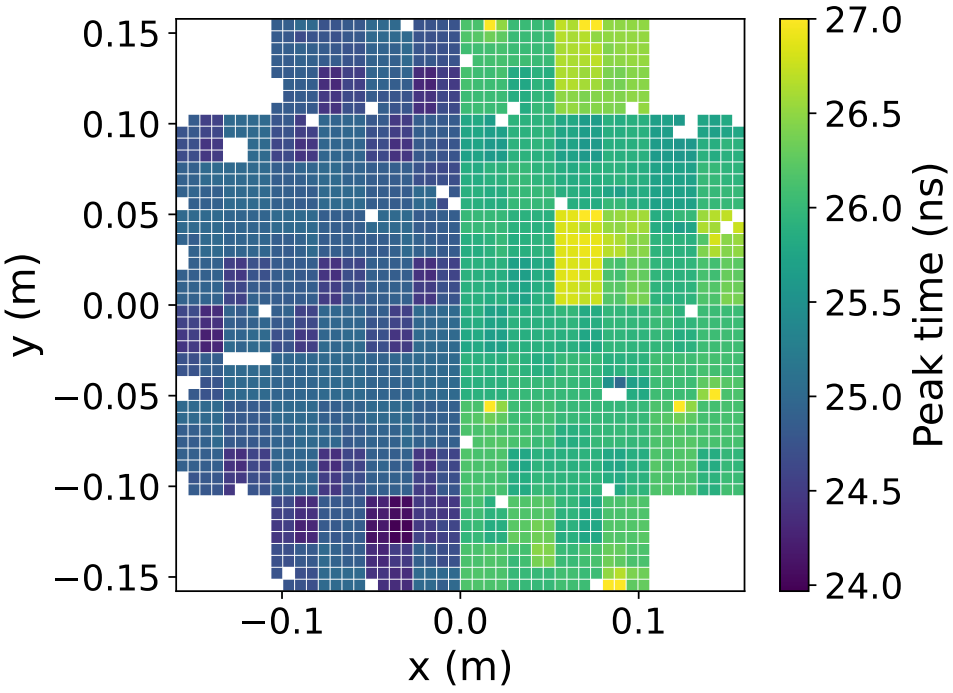

Figure 4.29: Map of the peak time values within the camera.

4.2.3 Amplitude matching and camera status

One of the next steps within the work with CHEC-S has been running an HV amplitude matching script. This serves the purpose of equalizing the response to a Cherenkov or laser signal of same intensity between all pixels. The procedure works iteratively, adjusting the over voltage of each superpixel at each iteration until the predetermined signal amplitude is reached. The result is a new HV configuration file with 512 individual values - one for each superpixel.

Figure 4.30 and Figure 4.31 show a map of the extracted charge within the camera before and after applying this procedure, when illuminating CHEC-S with 2000 photons.

As we can observe, the charge uniformity improves significantly, increasing from 82.8% to 89.8%; moreover, it is also possible to detect some “bad” or “dead” pixels or superpixels.

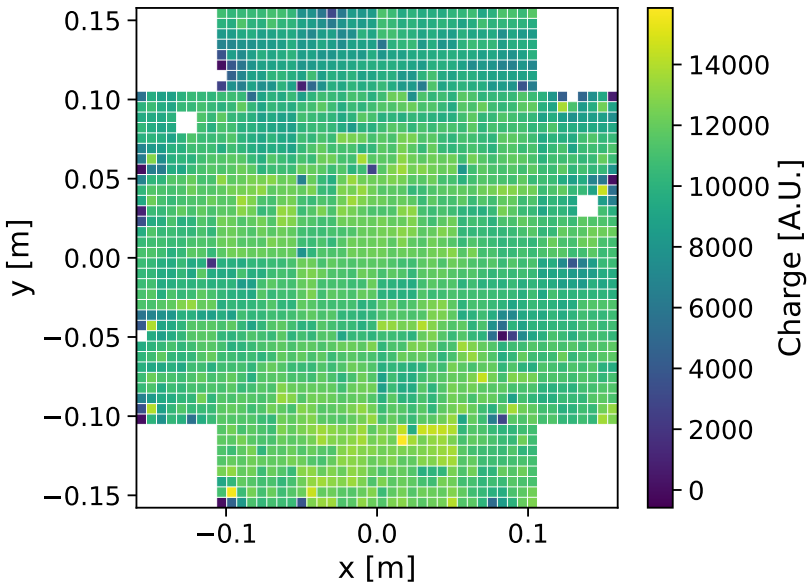

Figure 4.30: Map of the extracted charge before the HV amplitude matching procedure.

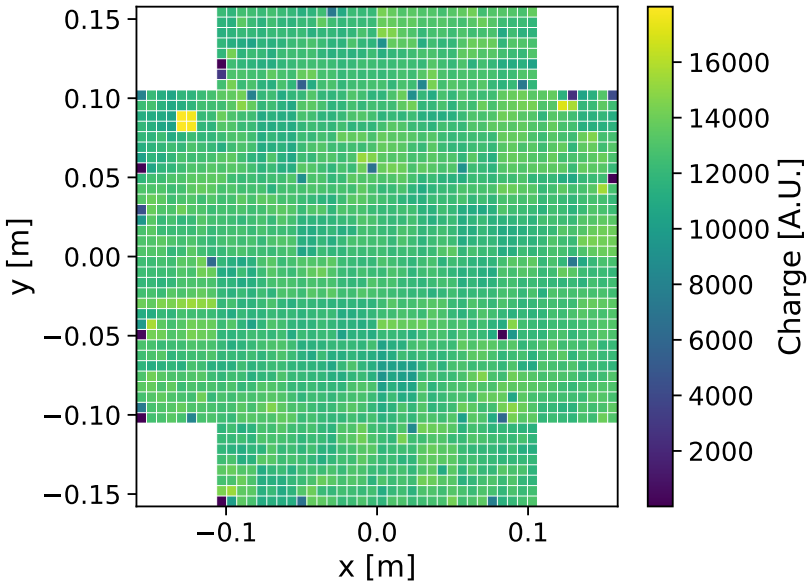

Figure 4.31: Map of the extracted charge after the HV amplitude matching procedure.

Based on the acquired data, it has been possible to briefly study the condition of the camera - specifically, the number of malfunctioning pixels. This is achievable by comparing the average collected charge of each pixel to the mean charge of the entire camera. Through this method, it is possible to pinpoint the problematic pixels.

To develop a general idea while not being too strict, we identified the "dead" pixels as the ones whose average charge lies outside the interval $\mu \pm 2\sigma$. Figure 4.32 shows the map of the malfunctioning pixels for this scenario.

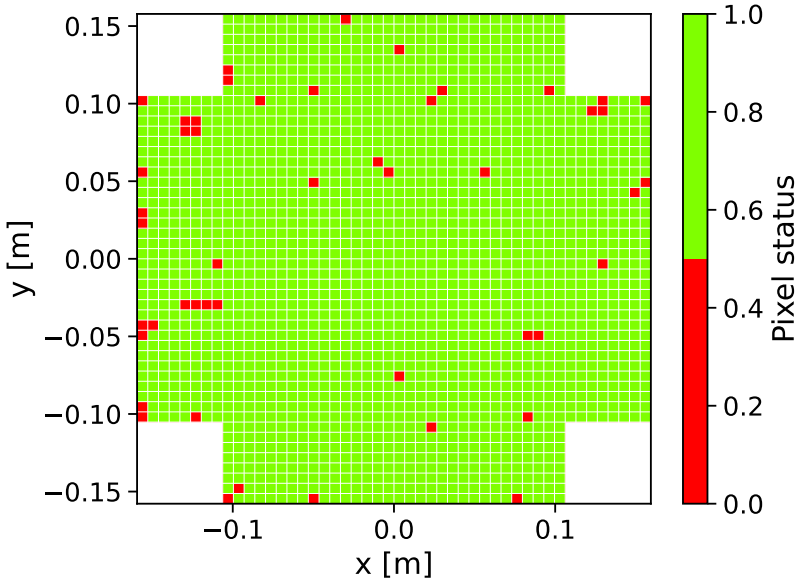

Figure 4.32: Pixels with an average charge that lies outside the $\mu \pm 2\sigma$ interval, after the HV matching procedure. The malfunctioning pixels constitute the 2.3% of the total number of pixels.

As we can observe, a majority of these pixels are corner pixels of their respective module, with also one entire malfunctioning superpixel.

Indeed, it is worth remembering that the camera had not been properly calibrated nor recently used, so the aim of this study was to make sure that the majority of the camera was functioning.

The percentage of malfunctioning pixels is 2.3% after the HV matching process was implemented.

If we discard the malfunctioning pixels and display again the extracted charge distribution, we obtain Figure 4.33.

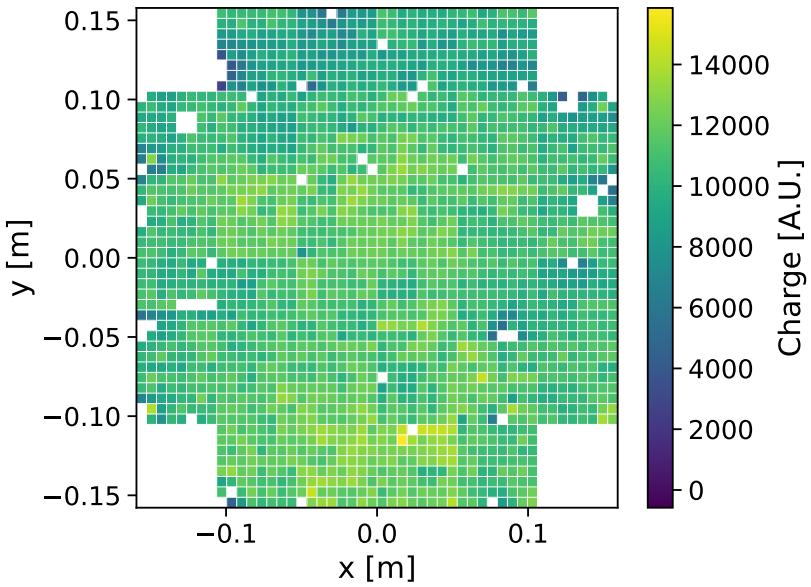

(a) 83.3% uniformity

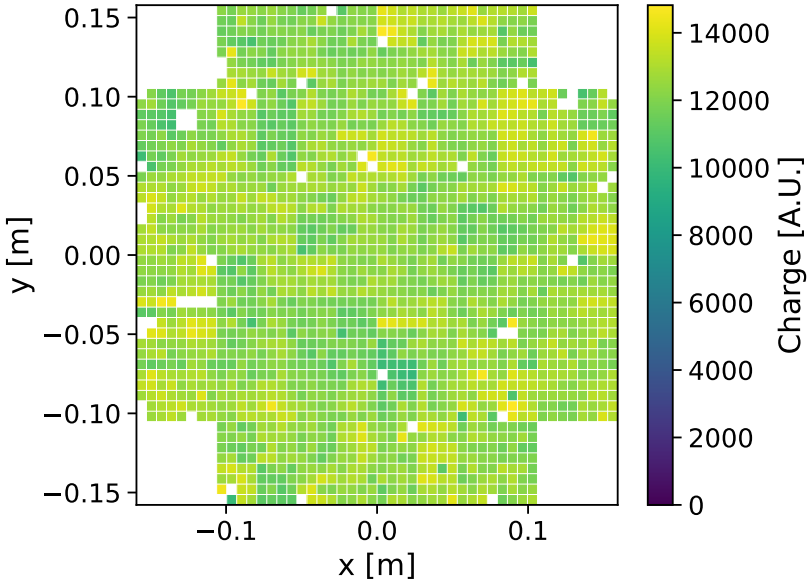

(b) 93.9% uniformity

Figure 4.33: Map of the extracted charge before (a) and after (b) the HV amplitude matching procedure, after eliminating the malfunctioning pixels. The charge uniformity within the camera improves in both cases.

4.2.4 Dynamic range

One of the final steps in working with CHEC-S was taking data at different illumination levels, i.e. running a *dynamic range scan*: this has been possible thanks to the filter wheel calibration already implemented in the facility (described in Section 4.1.3).

We then developed a python script to manage the experimental setup for subsequent data runs, each with varying photon levels, at a frequency of 600 Hz: particularly, the

chosen interval lied between 1 photons to 2000 photons. The pedestal was applied to each run.

Data were then fed to a calibration and analysis pipeline, which gave us several useful values, for example the mean waveform and its standard deviation, the collected charge and the signal height.

Among these, we are interested in the extracted charge, because it is strictly and directly related to the number of photoelectrons, hence to the number of observed photons. In order to extract these numbers, it is necessary to know the Single Photo-Electron (SPE) value, i.e. the amount of charge corresponding to one photoelectron, and the PDE of the devices.

Then, the number of photons is evaluated as [22]

$$n_{ph} = \frac{n_{pe}}{\text{PDE}} = \frac{Q}{\text{SPE} \cdot \text{PDE}}$$

With respect to CHEC-S, an updated measure of the SPE is currently unavailable, and its evaluation was not included in the goals of this project. Therefore, it is not possible to precisely convert the observed charge into an actual number of photons.

Hence, the main goal of this part was purely to observe a linear response among the dynamic range before reaching the saturation point, similar to the one obtained during the calibration of the filter wheel. This is shown in Figure 4.34.

Unfortunately, we were unable to conduct a more detailed investigation of the upper section of the range where saturation is expected, due to time constraints.

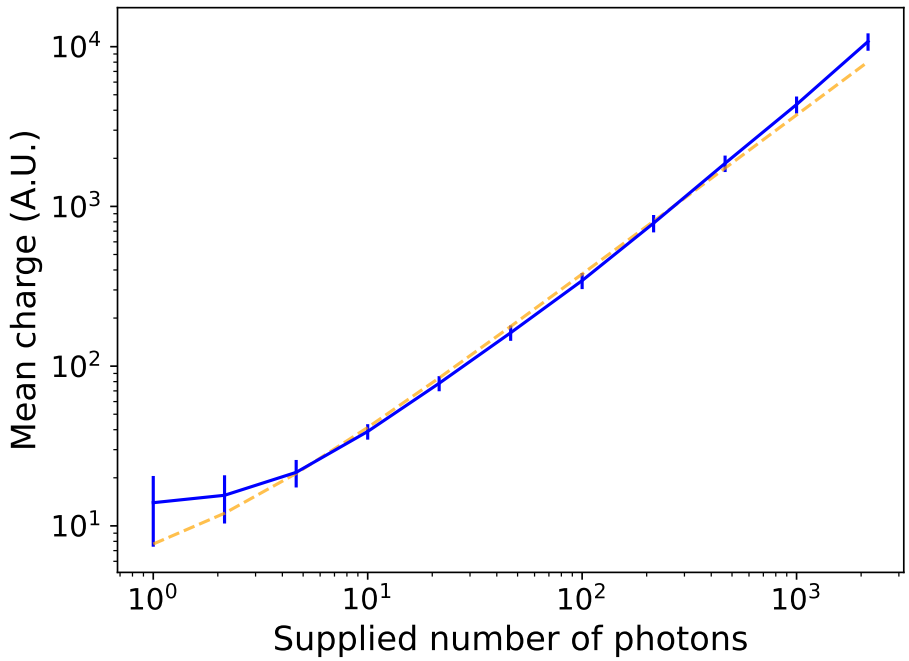

Figure 4.34: Average extracted charge and standard deviation as a function of the different supplied light levels, log-log scale.

Chapter 5

Preliminary measurements on the SST Camera

5.1 The first SST module

The initial modules for the SST camera have already been assembled: they include TARGET modules, Focal Plane Electronics and Silicon Photomultipliers, and they are currently undergoing testing.

In this section, some preliminary measurements on the first SST Camera Module - both on the TARGET module alone and with the 64-SiPMs - are presented.

5.1.1 TARGET Modules

As outlined in Chapter 3, the readout electronics of an SST camera consists of three boards - Primary, Power, and Auxiliary - per module, where the **T**eV **A**rray **R**eadout Electronics with **G**Sa/s sampling and **E**vent **T**rigger (TARGET) **A**pplication **S**pecific **I**ntegrated **C**ircuits (ASICs) are assembled. This system's primary functions are to trigger at an initial level and digitise the signals [31].

Pedestal measurement

As we have already seen, the term "pedestal" refers to the electronic background noise that exists in a detector even in the absence of a physical signal. Since it contributes to the device's total noise, it is important to quantify it in order to have a good estimate of the noise inside the detector.

In complex read-out systems such as the one of the SST Camera, the pedestal level may originate from various system components.

Here, we present a measurement of the pedestal for the TARGET module. The measurement was conducted at Max Planck Institut für Kernphysik, with a setup consisting in the following: a 24 V power supply, the Target Module, an adapter board that allows to connect the TM to the DarkBox PC via optical fibre.

Figure 5.1 illustrates the mean pedestal distribution over all events for the first pixel of the TM, that has a mean value of 0.23 ADC and a standard deviation of 0.22 ADC.

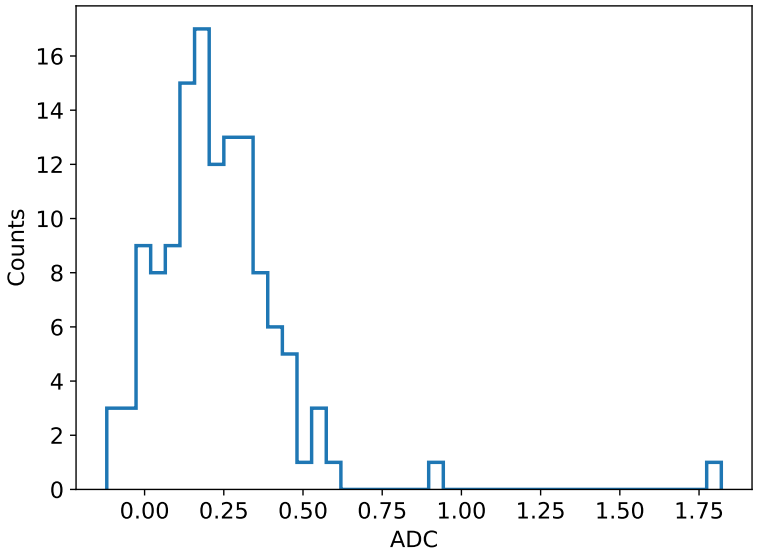

Figure 5.1: Mean pedestal distribution for pixel n. 0.

Evaluating the mean pedestal and standard deviation for all pixels, we obtain a 2D histogram, shown in Figure 5.2 and Figure 5.3: pedestal values are moderate and not worrying.

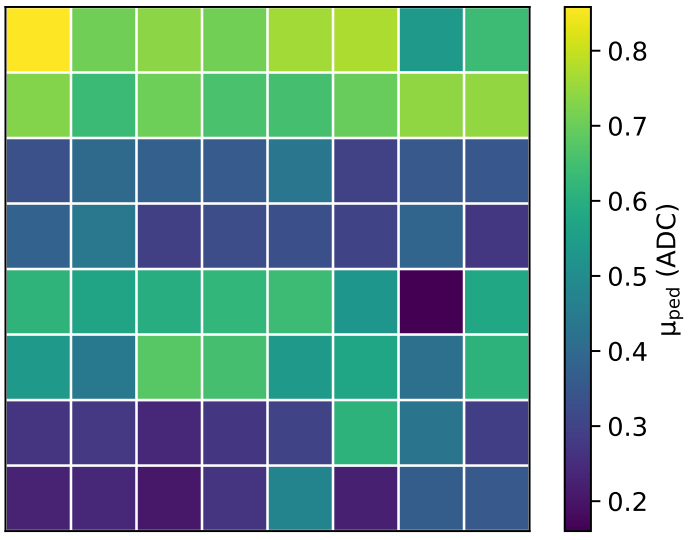

Figure 5.2: Map of μ_{ped} within the TM.

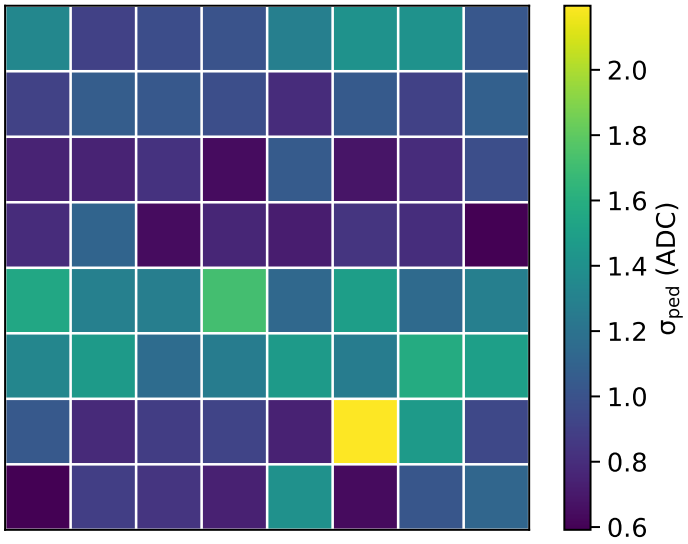

Figure 5.3: Map of σ_{ped} within the TM.

The mean pedestal values, presented as a function of the pixel channel, are depicted in Figure 5.4, along with their standard deviation. The four ASICs are separated by a dashed line.

There is no noticeable difference in the pedestal values from one ASIC to another: this means that there is no ASIC noisier than another, which is of course what one wishes for.

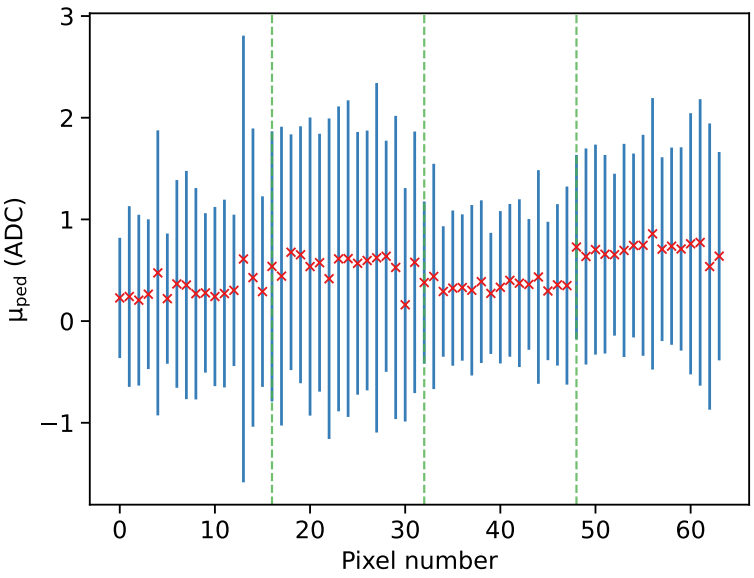

Figure 5.4: Values of $\mu_{ped} \pm \sigma_{ped}$ for all 64 pixels of the TM.

Further tests will be conducted in the coming months to study the electronic noise of the modules after the addition of the other components. In particular, it will be studied how the noise increases when the bias board, preamplifier board and SiPMs are added to the module, with each contribution studied separately.

In addition, other modules will be tested, in order to observe if and how the electronic noise varies, since the boards are produced in the same batch. All these modules will then be assembled in the first quarter of the camera (QCAM).

5.1.2 64-SiPMs module

The measurements presented in this section were taken in Leicester, United Kingdom, with an experimental setup very similar to the one of the validation facility at MPIK.

The setup included an NSB source and a laser source; a picture of the SST module under test is shown in Figure 5.5. The silicon photomultipliers tile is enclosed in a box to keep the sensors at the proper temperature and humidity levels.

The NSB source was developed by replicating the concept proven in the MPIK commissioning facility: thus, it consists of a constant LED, a beam splitter and a powermeter.

In the laser source the beam, instead of being uniformly diffused as in the MPIK commissioning facility, is focused to fire only one SiPM at a time in the tile. An X-Y stage allows to scan all 64 pixels.

The decision to focus the laser beam on one pixel at a time, rather than using a diffused one, served the purpose of being able to perform also crosstalk measurements.

Despite this, the measurements presented here can be entirely replicated in the commissioning facility.

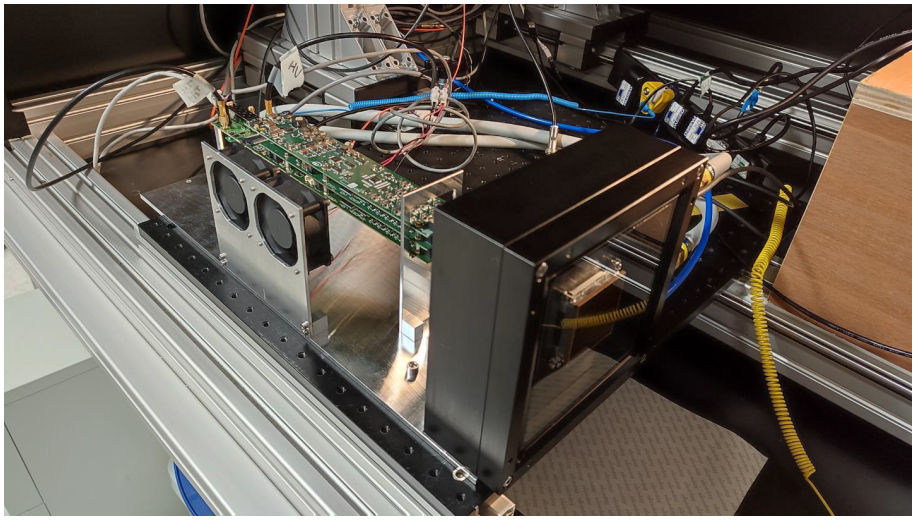

Figure 5.5: The SST Module in Leicester.

Signal study

In this section, we present an analysis of the data collected regarding the shape and timing of SiPM signal. The data were collected by externally triggering the sensors of the module with a pulse generator.

It is worth noting that all measurements were performed on an *uncalibrated* module, meaning that no gain matching had been applied yet. Gain matching is a standard practice wherein high voltage values are adjusted iteratively for each pixel to achieve uniform gain across the entire array, while illuminating the module with a uniform light. This process will be conducted in the commissioning facility at MPIK (described in Chapter 4).

In order to achieve at least a similar gain among the sensors, all 64 silicon photomultipliers were supplied an overvoltage of 5.9 V, according to the specifications provided by the manufacturer. In fact, each SiPM has a different breakdown voltage; the gain is given by the product of the overvoltage, i.e. the difference between the bias and breakdown voltages, and the cell capacitance of the SiPM. Under the (unrealistic) assumption that the capacitance is the same for all SiPMs and that the breakdown voltage is perfectly known, the SiPMs would have the same gain.

For the reasons just described, the measurements outlined here are considered *preliminary*.

The goal of these measurements was then to check the functionality of the whole module and a few signal characteristics, in order to compare them to the ones expected by design.

The analysis focuses on four primary aspects of the signal:

A. Full Width Half Maximum (FWHM)

B. Rise time

C. Pulse time

D. Pulse height

Since each ASIC is responsible for 16 sensors (Figure 5.6), the analysis also aimed to assess whether there is any noticeable difference between each of the four ASICs assigned to manage the 64-SiPMs tile.

Ideally, there should be no observable differences, as the aim is to maintain consistent behaviour across all tiles in the module.

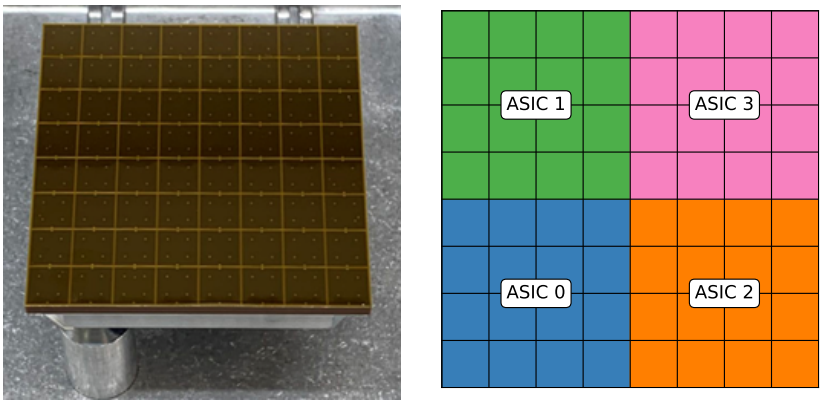

(a) (b)

Figure 5.6: Picture of the SiPM tile and schematics of the four ASICs of the SST module.

FWHM The Full Width Half Maximum is a measure of the width of a signal at half of its maximum amplitude and is usually defined to quantify the spread of a signal.

From Monte Carlo simulations, FWHM values for this module are expected to lie between 5 ns and 10 ns: indeed, below 5 ns there is not enough pile up of the signals to activate the camera trigger, while above 10 ns a lot of background noise gets integrated together with the real signal, degrading the performance.

As we can see in Figure 5.7, FWHM values lie between 7.86 ns and 8.75 ns, which are completely included in the expected range.

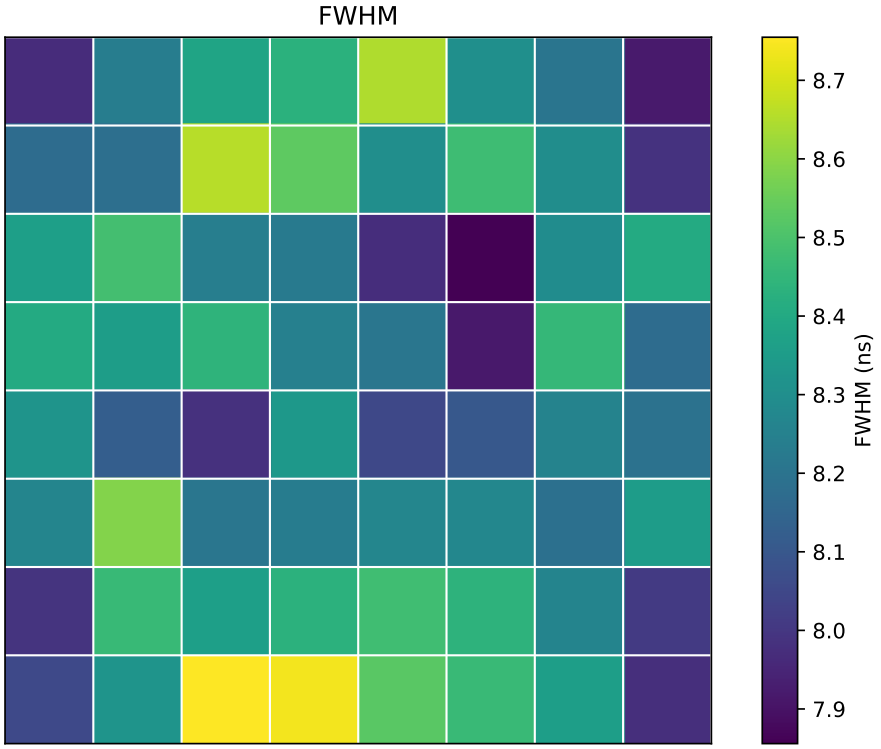

Figure 5.7: Map of Full Width Half Maximum values along the SiPM tile.

Additionally, Figure 5.8 shows the mean FWHM for each digital channel, differentiated by ASIC number, while Figure 5.9 depicts the mean value and standard deviation for each individual ASIC.

It appears that there is no discernible difference among the four ASICs, as the Full Width Half Maximum across the module uniformly reaches 97.6%, evaluated as $(1-\sigma/\mu)$, with a mean value μ of 8.28 ns and a standard deviation σ of 0.20 ns.

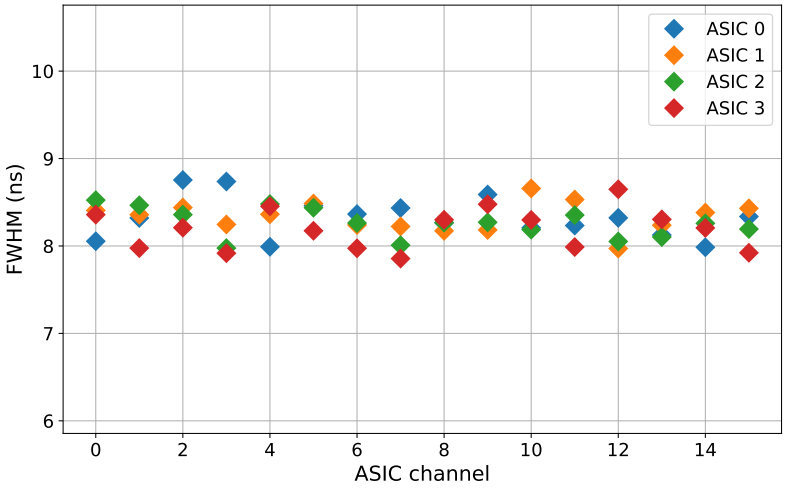

Figure 5.8: Full Width Half Maximum values for the four ASICs of the SST Module: values per channel.

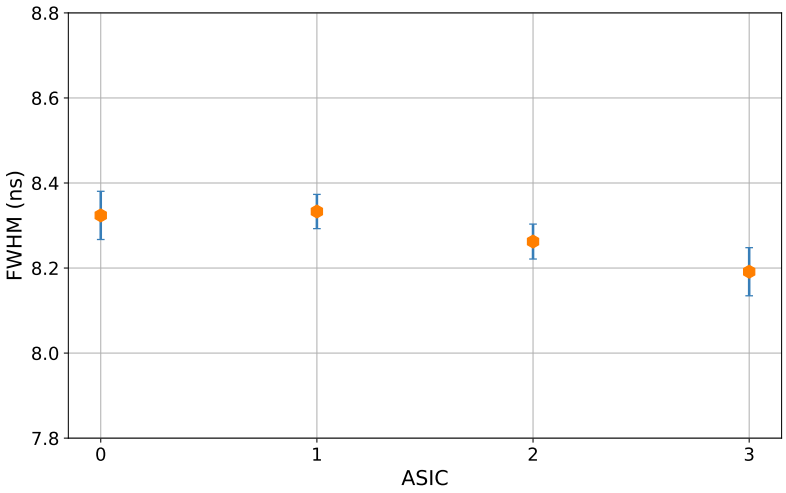

Figure 5.9: Full Width Half Maximum values for the four ASICs of the SST Module: mean values per ASIC.

Rise time Rise time is determined by the time it takes for the amplitude of the signal to go from 10% to 90% of its maximum.

In Figure 5.10 the rise time values for all the 64 pixels are shown: with a mean value of 4.19 ns and a standard deviation of 0.08 ns, the rise time happens to be 98.17% uniform.

Indeed, there seems to be no evident difference between the four subsets of pixels: this can be further investigated by displaying the mean rise time for each channel while differentiating between the four ASICs, like in Figure 5.11a. Here we have a quite uniform distribution where no set of values consistently differs from the other.

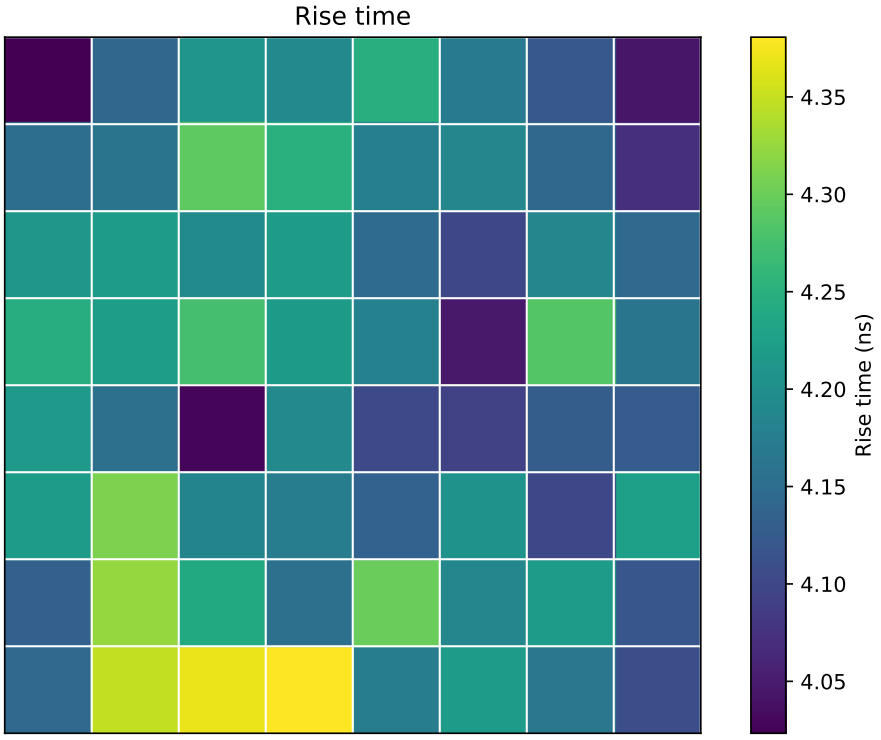

Figure 5.10: Map of rise time values along the SiPM tile.

This can be further confirmed by Figure 5.11b, where the mean rise time for each ASIC, together with its standard deviation, is shown.

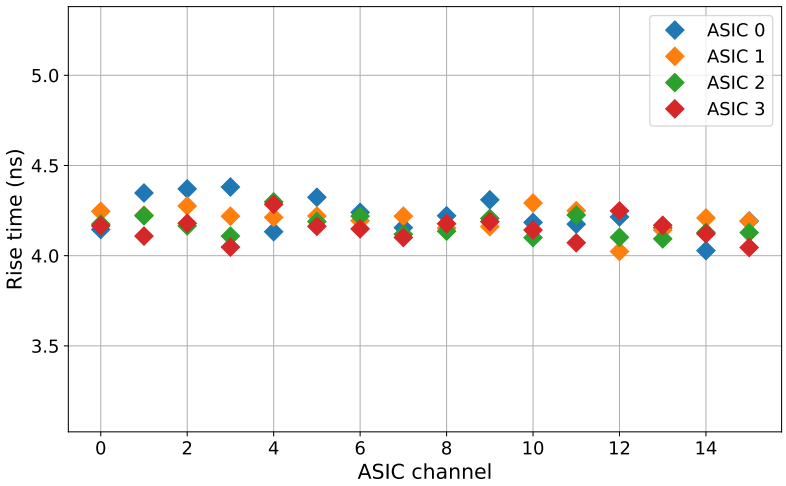

(a)

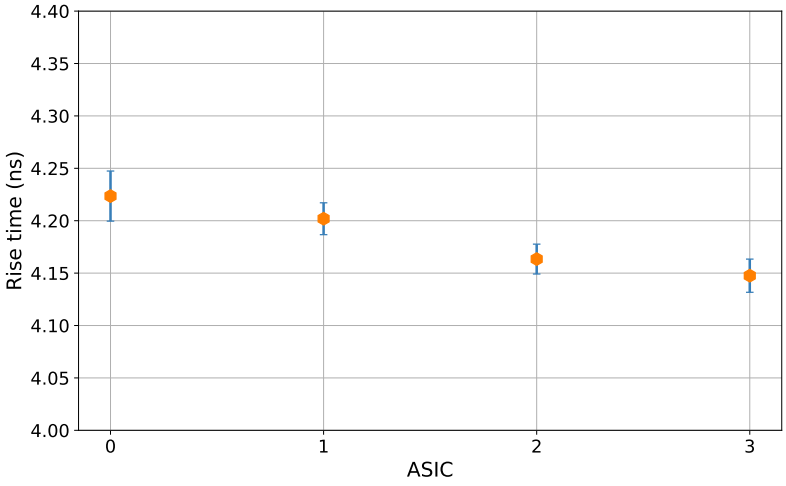

(b)

Figure 5.11: Rise time values for the four ASICs of the SST Module: values per ASIC channel (a) and mean values per ASIC (b).

Pulse time Pulse time is defined as the time interval during which the amplitude of a signal remains above a certain threshold or within a certain range.

Looking at Figure 5.12 and Figure 5.13, it is clear that ASIC n. 3 has much lower pulse time values compared to the others, therefore being the faster ASIC of the set.

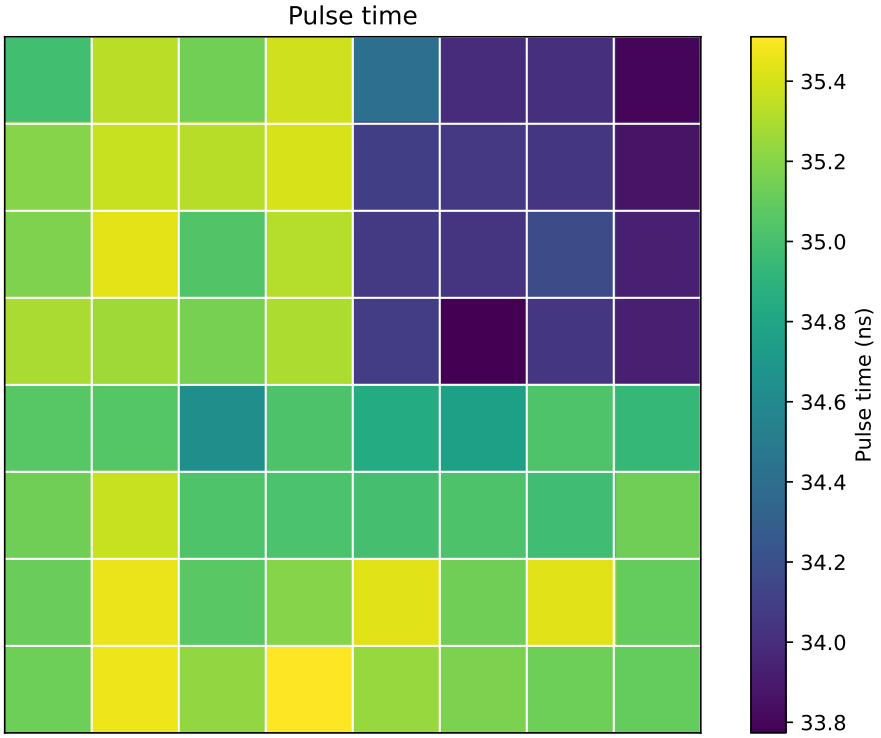

Figure 5.12: Map of pulse time values along the SiPM tile.

The problem was investigated and resulted in a difference between the pathways that connect the ASICs to the internal clock: this latter serves the purpose to manage all tasks, including sending the trigger and therefore starting the data collection. The pathway that connects ASIC n. 3 is longer than the other ones, causing it to start collecting the data with a certain delay. For this reason, it records the maximum pulse before the others.

This issue has already been taken into account and will be corrected in the software.

With a mean of 34.9 ns and a standard deviation of 0.53 ns, the whole module appears to be 98.5% uniform; if we remove the ASIC dependence by subtracting the mean of each ASIC from the data, we obtain 99.5% uniformity.

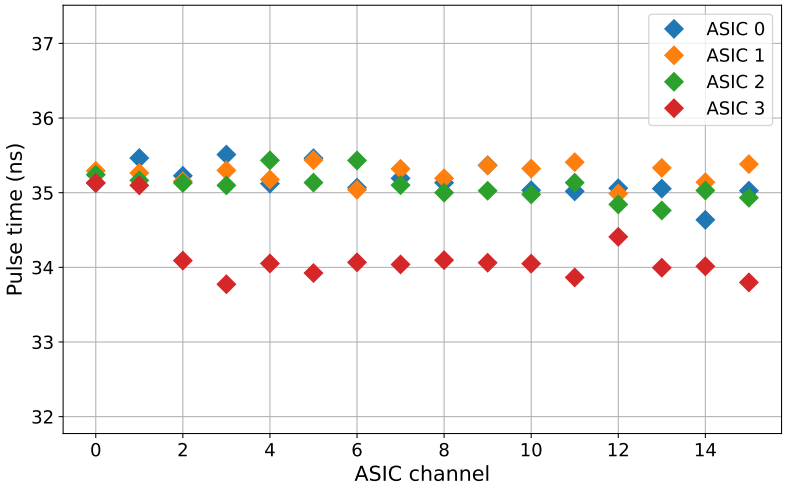

(a)

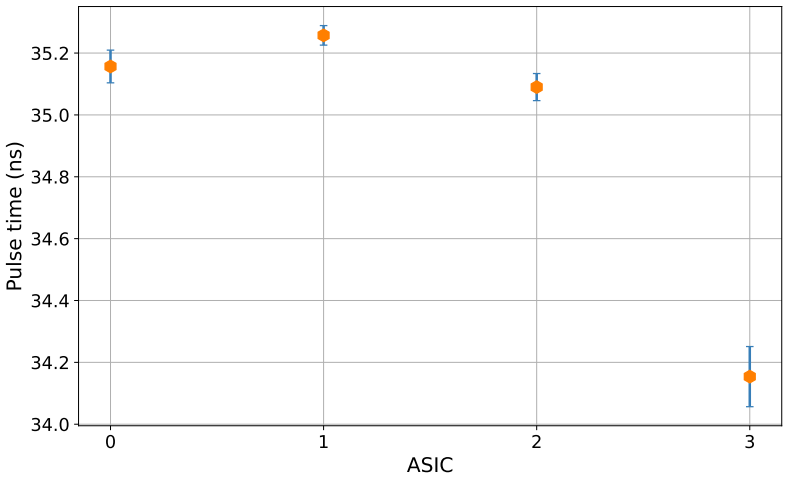

(b)

Figure 5.13: Pulse time values for the four ASICs of the SST Module: values per channel (a) and mean values per ASIC (b).

Pulse height Pulse height is defined as the maximum amplitude of the signal.

In Figure 5.14, a notable difference is instantly visible among the four ASICs. Specifically, ASIC n. 0 exhibits greater pulse heights than its counterparts, whereas ASIC n. 1 displays lower pulse height values.

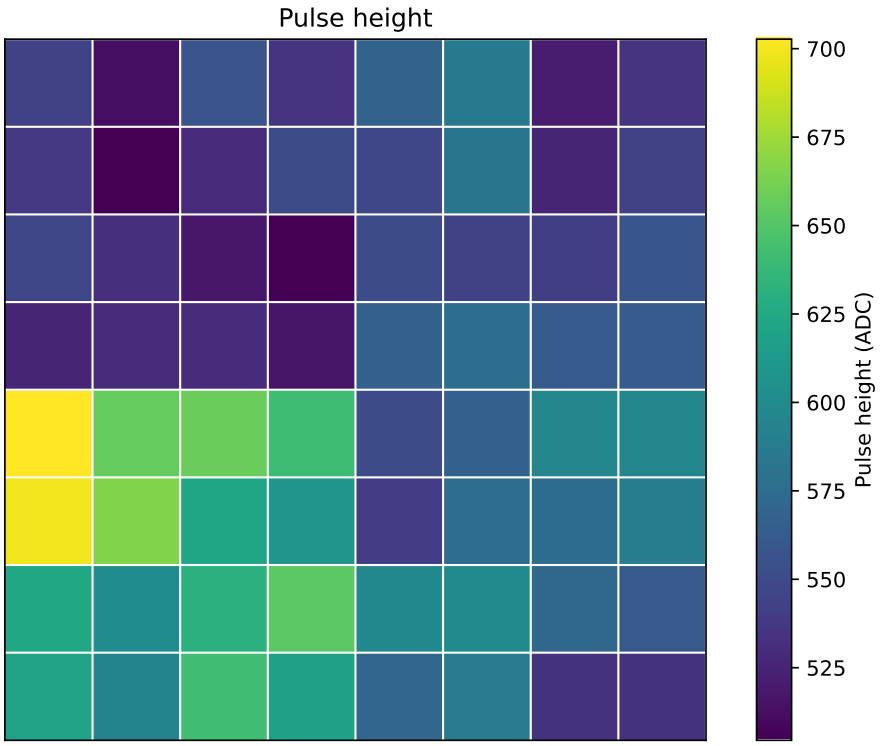

Figure 5.14: Map of pulse height values along the SiPM tile.

This contrast can be further observed in Figure 5.15a and Figure 5.15b.

This difference can be explained by the fact that the sensor and the module's electronic have not yet been calibrated, leading to different gain values between the four subsets of SiPMs; having uncalibrated devices also gives us rapidly varying pulse height values inside the same ASIC, as we can observe for ASIC n. 0 in Figure 5.15a, for instance.

With a mean of 573.3 ADC and a standard deviation of 46.6 ADC, the pulse height is now 91.87% uniform; a gain matching procedure will indeed improve this result.

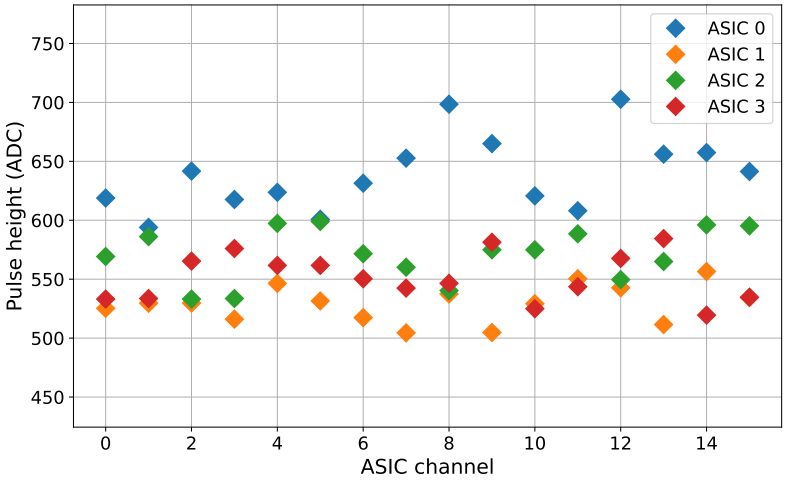

(a)

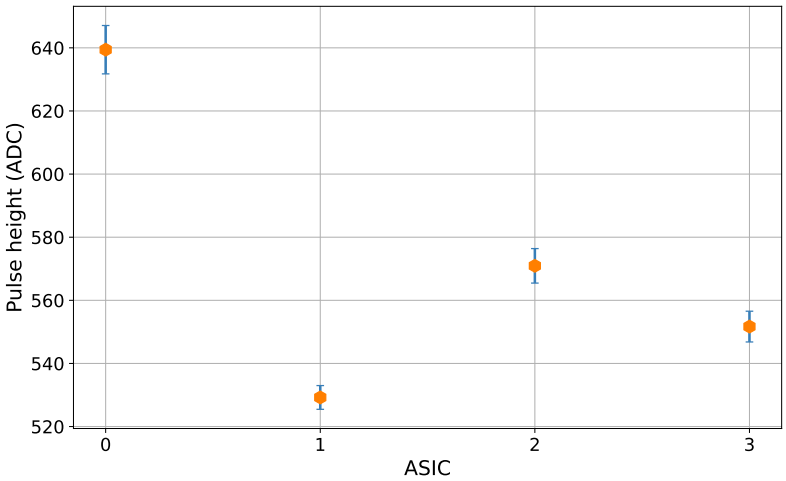

(b)

Figure 5.15: Pulse height values for the four ASICs of the SST Module: values per channel (a) and mean values per ASIC (b).

5.2 Power supply system testing

As mentioned in Chapter 3, in the new SST Camera design all power supplies will be mounted inside the camera on the bottom panel of the enclosure, in contrast to what was designed for the CHEC-S prototype, which had an external power supply. This choice was made in order to avoid the use of huge power cables plugged into the camera from the outside.

Of course, this choice arises the question of effectively dissipating the heat generated by the power supply system to prevent the electronics and silicon sensors from overheating. The latter, especially, must be maintained at specific temperatures to prevent changes to their characteristics, such as gain and dark count rate, among others.

5.2.1 Efficiency

A first evaluation of the Main PSU's efficiency was conducted using an Electronic Load (EA-EL 9080-170 B, Figure 5.16), which served to mimic the total output power load that a single camera would face on site.

Figure 5.16: Electronic power load.

The input power has been measured for different current values using a electrical power meter (Janitza B21 312-10J Electricity meter); both input and output measurements are shown in Figure 5.17.

By using the dissipated power values, i.e. $W_{in} - W_{out}$, we were able to determine the system's *inefficiency* as $\xi = W_{dissipated}/W_{out}$ and its efficiency as $1 - \xi$; we obtained a minimum efficiency value of 79.1 ± 1.0 % at 5 A and a maximum of 93.6 ± 0.9 % at 60 A, as shown in Figure 5.18, which indeed corresponds to the nominal value [29].

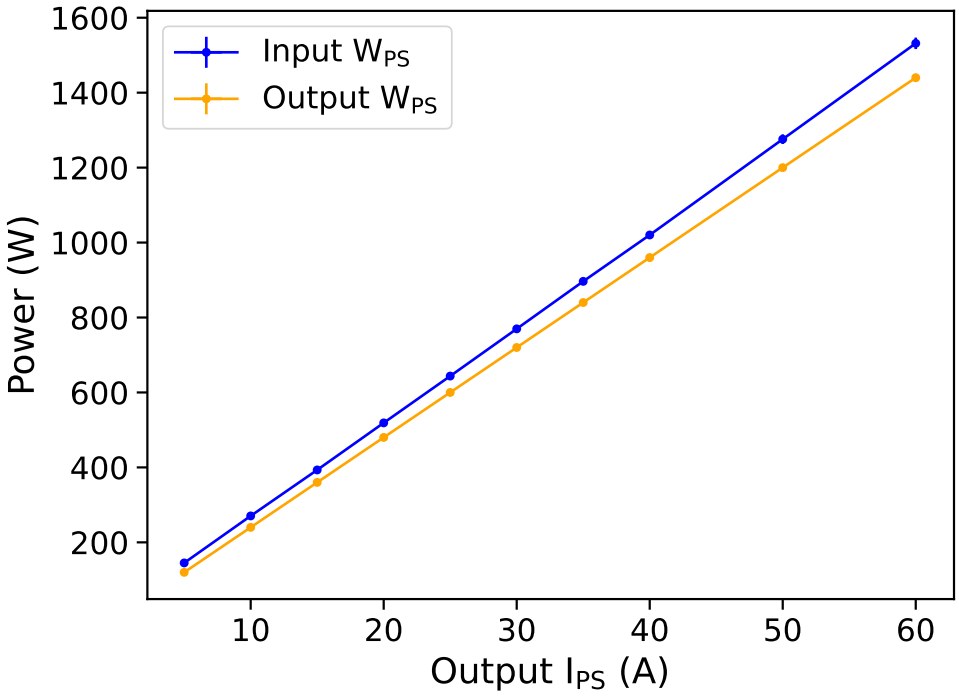

Figure 5.17: Measured input and output power for the Main PSU.

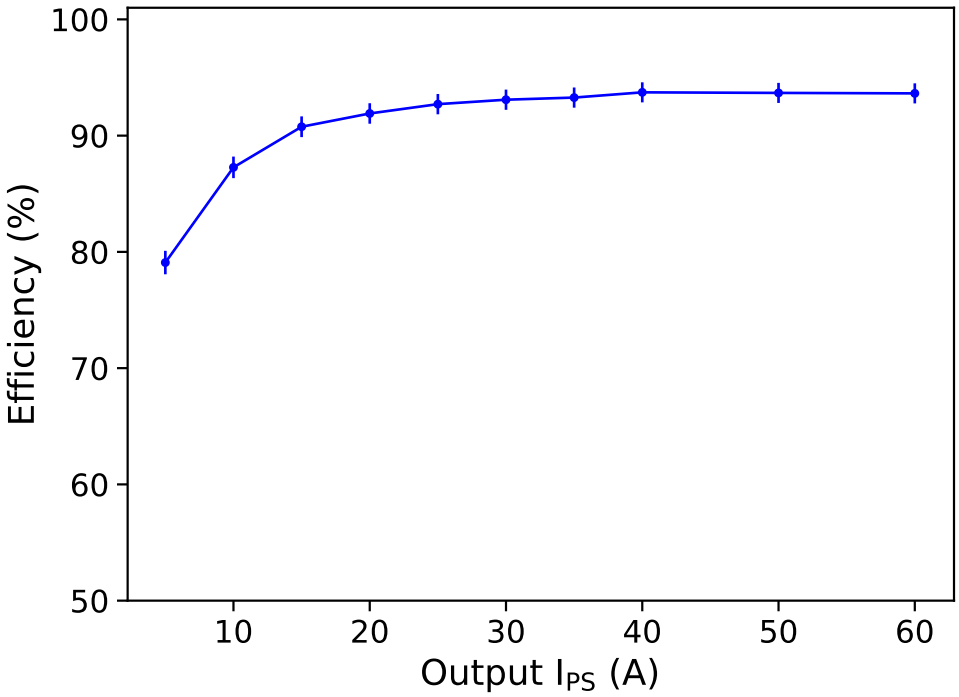

Figure 5.18: Evaluated efficiency for the Main PSU.

5.2.2 Heat dissipation test

Given that dispersed power mostly goes into heat, our next goal was to understand what temperatures the PSU panel could reach at different power loads in different situations; this would've allowed us to test the effectiveness of the environmental devices designed for the camera, as, for example, the use of conductive thermal paste and of the cooling system, consisting of sets of internal fans and an external chiller.

Seven type-T thermocouples ([45]) were positioned at different points of the PSU panel, including the Main PSU and the back of the aluminium board. We employed a data logger (TC-08 Data Logger by Pico Technology) to measure temperatures, while monitoring the room temperature T_{room} using another thermocouple placed in the air. Please refer to Figure 5.19 for a diagram outlining the placement scheme for the thermocouples on the power supply board.

We selected a standard current load of 50 A for our measurements, which corresponds to a power of 1.2 kW and is a typical expected load for a single observing SST camera; in each configuration, for safety reasons, we started with 20 A, which correspond to a power of 480 W, before going of 50 A.

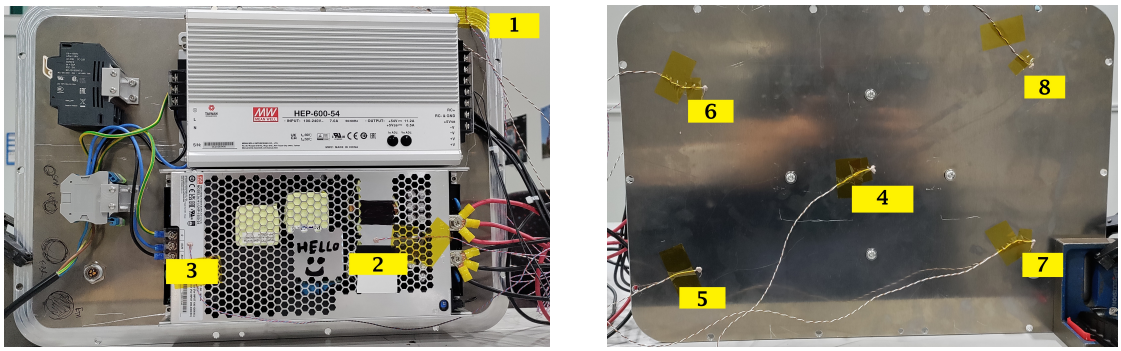

(a) (b)

Figure 5.19: Position of the eight thermocouples and the corresponding channels of the data logger.

Data taking

Data were then collected gradually, in order to highlight the improvement in heat dissipation brought by such precautions.

Measurements were performed with the following order:

A. On the PSU panel as it was, detached from the camera's enclosure, placed standalone on the table

B. With thermal paste (Kerafol KERATHERM KP12, thermal conductivity of 10 $\mathrm{W\,mK^{-1}}$) applied between the Main PSU and the aluminum board

C. Attaching the PSU panel to the camera enclosure (as in Figure 3.5)

D. Simulating the night wind with an external fan blowing on the camera enclosure

E. Turning on the internal fan trays and setting the external chiller to 15 °C (without external wind).

Additionally, two step scans have been performed, looping over different current load values: the first was performed while having the board inside the camera enclosure and the second with the cooling system turned on.

All measures shown in the following plots are evaluated as $\Delta T = T_{measured} - T_{room}$, unless specified otherwise.

Results

Figure 5.20 shows an increase in the heating of the whole panel when the current load increases: the point directly on the Main PSU (Channel n. 2), particularly, gets much hotter with respect to the other points, as we imagined, with a maximum variation of 15.2 °C with respect to room temperature, at a current load of 20 A, and of 26.1 °C at 50 A.

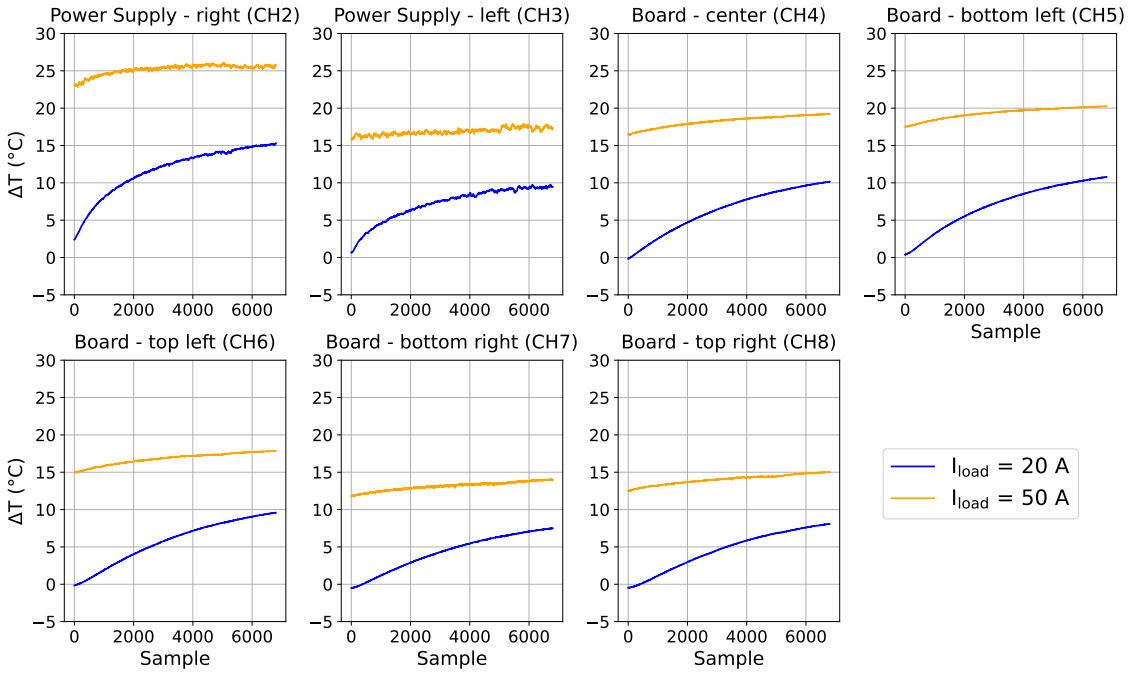

Figure 5.20: Temperature variation on the power supply panel with no thermal paste applied (measurement A.): comparison between two different loads of 20 A and 50 A.

By applying the thermal paste (Measure B., Figure 5.21), we can observe a decrease in the warming up of the two points on the power supply: channel 2 has a maximum increase of 23.1 °C, while channel 3 of 15.8 °C. Meanwhile, all the points on the back of the aluminum board get hotter: this indicates us that the thermal paste improves the thermal conduction towards the external panel. It would be interesting to observe the impact that other thermal greases could have and see if there is an even more effective one.

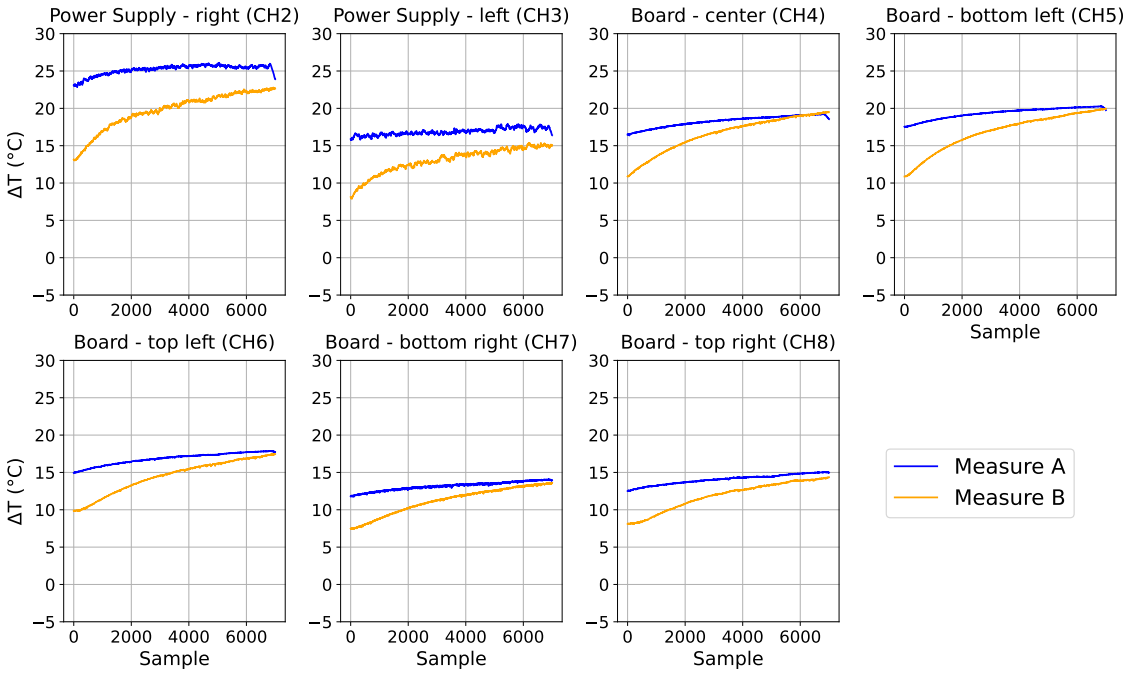

Figure 5.21: Temperature variation on the power supply panel with a current load of 50 A: comparison between having no thermal paste and having it applied (Measurement B.).

As we could suppose, by attaching the power supply panel into the camera enclosure (Measure C.), which is quite a closed space - despite still having some open holes, the temperature on the Main PSU increases again considerably (Figure 5.22), with a peak of $\Delta T = 27.2\,°C$ for channel 2.

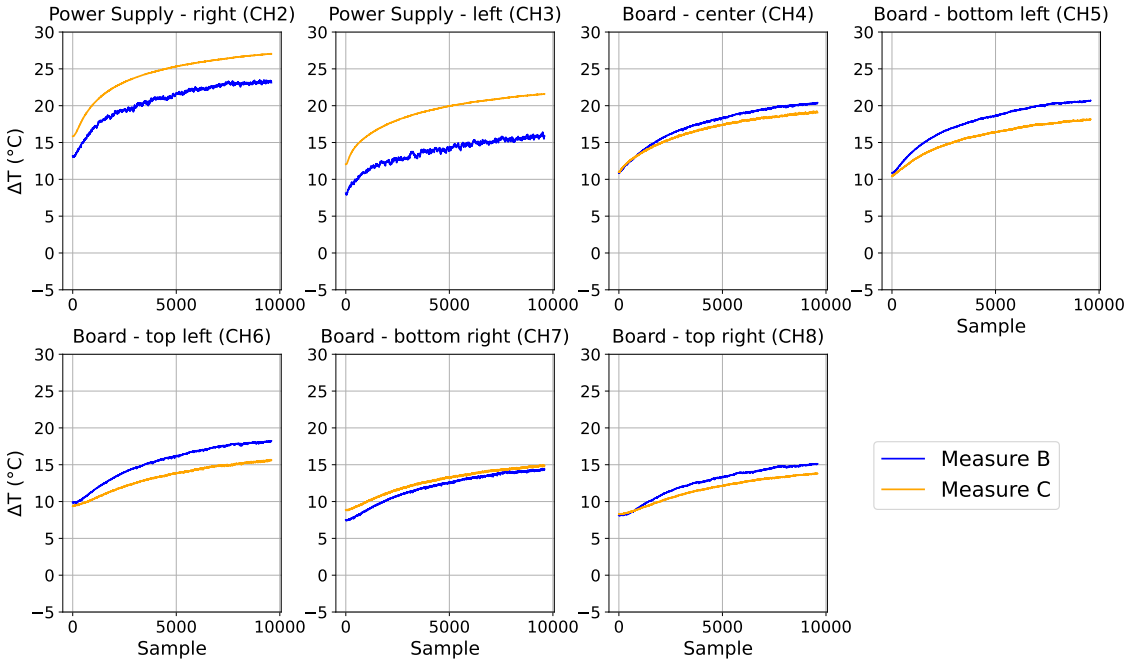

Figure 5.22: Temperature variation on the power supply panel with a current load of 50 A: comparison between having thermal paste applied and attaching the panel to the camera enclosure (Measurement C.).

If we try to simulate a quite strong night-time wind of $7.7\,\mathrm{m\,s^{-1}}$ (Measure D.), the panel cools down even being inside the camera enclosure (Figure 5.23): this can mean that even a "simple" movement of air around an operating camera can slightly condition its heating up - this, of course, with still no cooling system on.

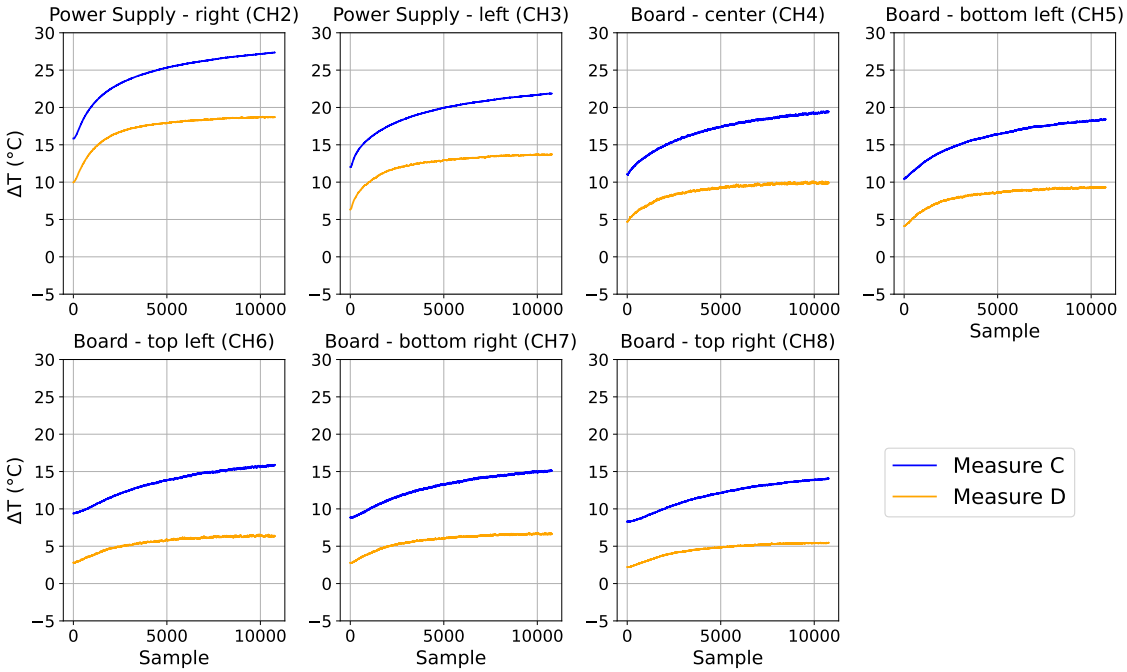

Figure 5.23: Temperature variation on the power supply panel with a current load of 50 A: comparison between having the panel inside the camera enclosure and simulating a wind of $7.7\,\mathrm{m\,s^{-1}}$ with an outer fan (Measurement D.).

Finally, by turning on the internal fans via the slow control board inside the camera and setting the external chiller on 15 °C (Measure E.), the variation of temperature generally drops (Figure 5.24). Channel 2 has now a maximum ΔT of 2.5 °C, while some channels even cool below room temperature: for example channel 3, which is still one of the two points on the Main PSU, gets cooled down quickly and has a maximum ΔT of -3.1 °C, meaning that it never gets hotter than the air. This is due to the fact that it is much closer to the fan trays with respect to channel 2.

Channels 4 and 5, on the other hand, have a maximum variation of 1.9 °C and 2.3 °C respectively: since they are the two points on the aluminum board directly on the other side of the PSU, this can again suggest that the designed enclosure has a good heat conduction.

Furthermore, we can also observe that the temperature gets stable more quickly when the cooling system is on, which is indeed a desirable feature for an operating camera.

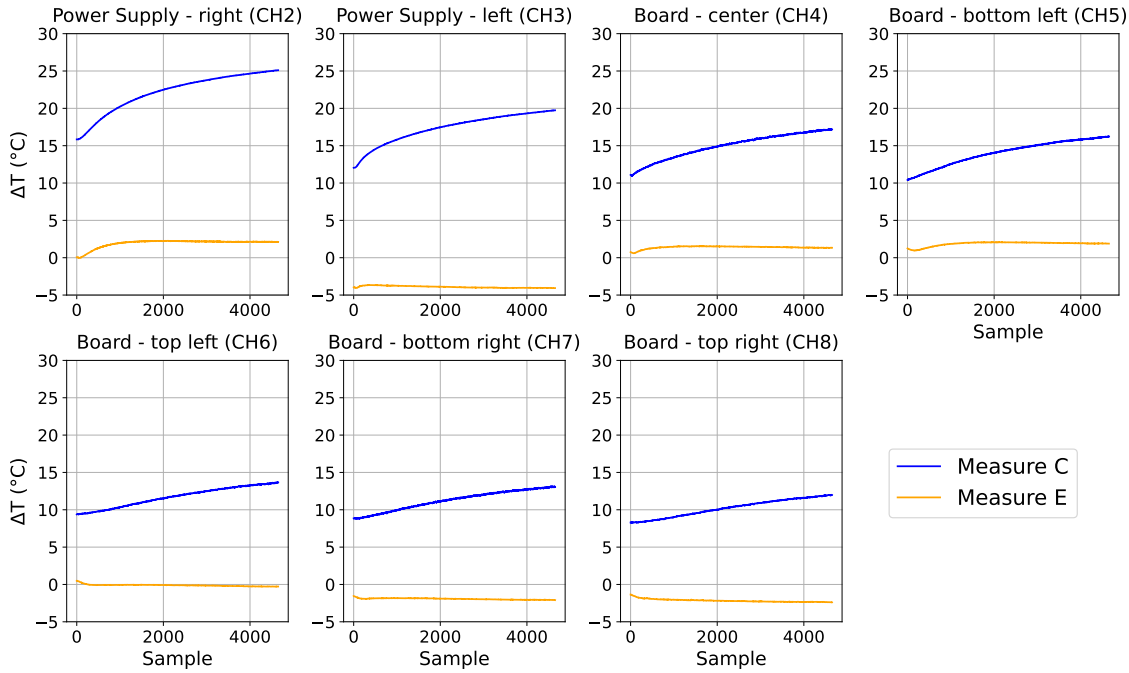

Figure 5.24: Temperature variation on the power supply panel with a current load of 50 A: comparison between having the panel inside the camera enclosure and turning on the internal fans and chiller, i.e. the camera cooling system (Measurement E.).

A general comparison between the different situations just discussed is shown in Figure 5.25: here, the values displayed are evaluated as the difference between the average temperature at stabilization and the average room temperature, i.e. cutting the temperature values of the initial rise.

As anticipated, the power supply board warms up considerably until we turn on the cooling system. Furthermore, the PSU itself (channel 2) is always the hottest point in all conditions, except for the last one where the heat gets better conducted to the external points (channels 4 and 5).

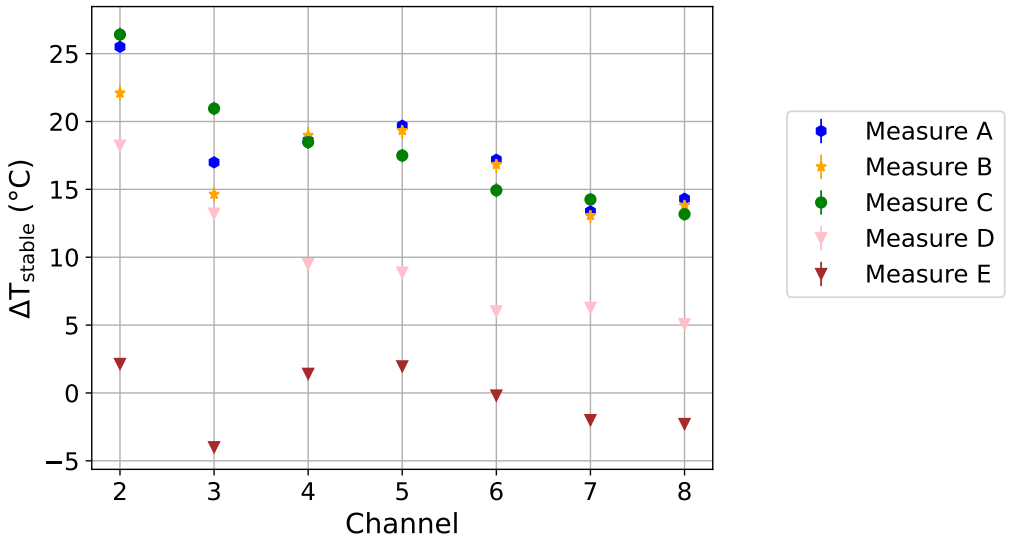

Figure 5.25: Comparison between different measurements; ΔT_{stable} is the difference between the average temperature at stabilization and the average room temperature.

Step scans Moreover, the two step tests (Figure 5.26 and Figure 5.27) show very clearly that the temperature increases as the current load increases and in both scenarios the temperature stabilizes at each current step during the acquisition time - 3 h in the first case and 2 h in the second.

However, data taken with the cooling system on show two distinct groups of channels: channels 2, 4 and 5 warm up more than channels 3, 6, 7 and 8. Again, this suggests that heat gets dissipated correctly towards the outside of the camera and that there is good thermal contact within the assembly.

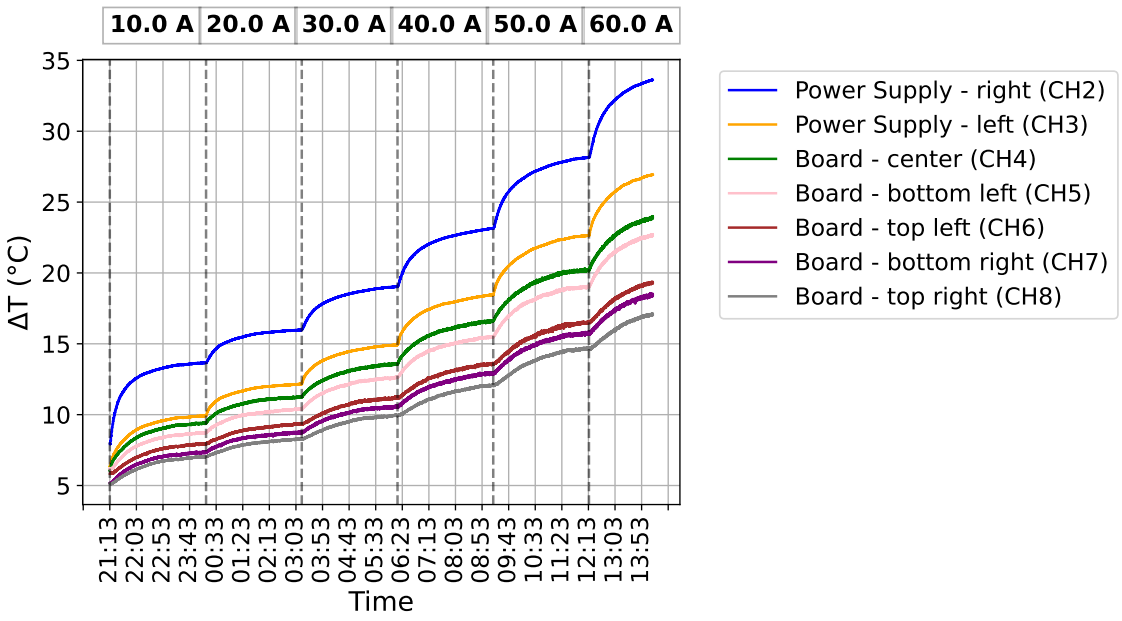

Figure 5.26: Temperature variation on the power supply panel with different current loads, with the panel attached to the camera enclosure; each step is a 3 h take. Data taken on 26-27/08/2023.

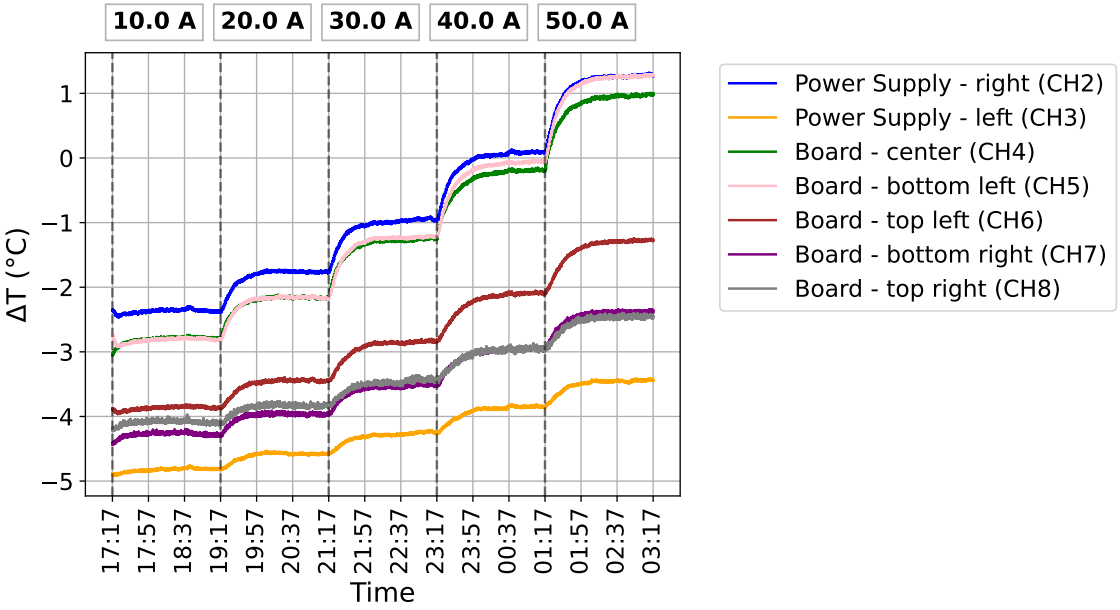

Figure 5.27: Temperature variation on the power supply panel with different current loads, with the cooling system running; each step is a 2 h take. Data taken on 29-30/08/2023.

Figure 5.28 shows again a comparison between having no cooling system at all and having it turned on: here we have the temperature variation as a function of the different current loads, displayed for every channel separately.

Here we can clearly observe that although the temperature increases as the current load increases, when the cooling system is working this variation is much smaller: if with no cooling ΔT goes from a minimum of 11.3 °C at 10 A to a maximum of 26.8 °C at 50 A for the "hottest" point on the panel (channel n. 2), with cooling it goes from −2.3 °C at 10 A to 0.04 °C at 50 A. The same behaviour can be observed for all the other points, suggesting that the cooling system indeed contributes to keeping the environmental conditions stable over the current load range, which is of course desirable for an operating SST camera.

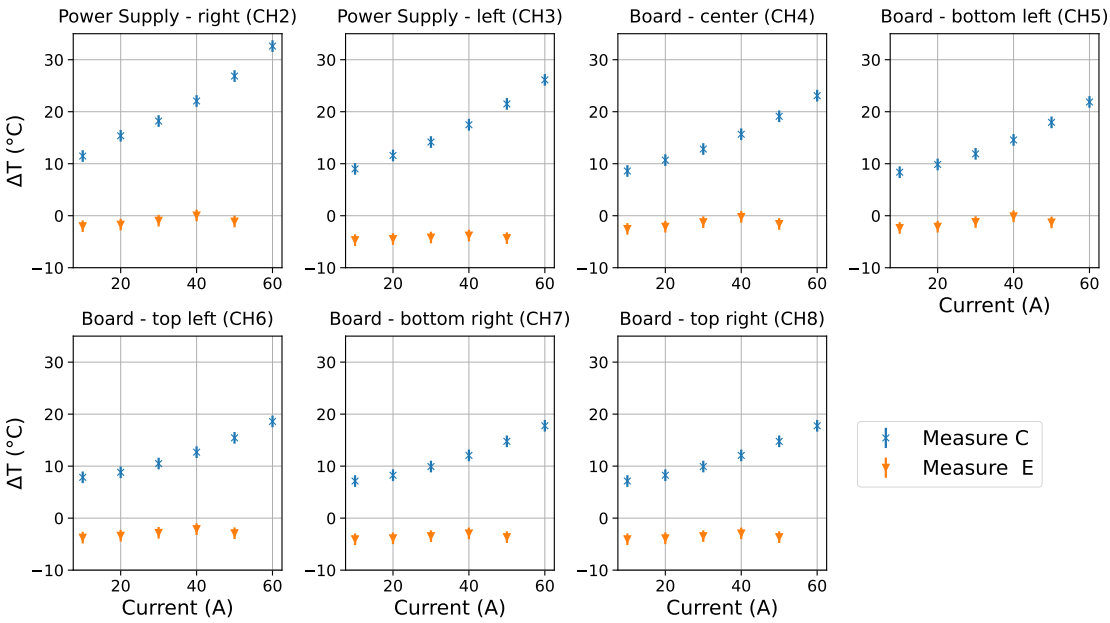

Figure 5.28: Variation of temperature on the eight thermocouples' positions as a function of different current loads: comparison between having the panel inside the enclosure with and without the cooling system turned on.

Preliminary considerations The tests and results presented in this section have been performed in order to assess the correct functionality of the cooling system and to confirm the absence of any critical issues at this stage. It is worth noting that these results are considered *preliminary* and require further testing under more realistic conditions. The tests were carried out on a partially assembled camera; therefore, similar measures should be repeated once the camera has been fully assembled.

Moreover, here we simulated the power load with an electronic device that was placed *outside* the camera: this allowed for the heat generated by the load to be dissipated outside of the instrument, as opposed to inside as it would in real-world conditions.

To further improve the accuracy of the heat generation simulation, additional testing could be conducted by incorporating resistances (such as RS PRO Wickel Lastwiderstand, 2.2 Ω) positioned within the camera enclosure and connected in parallel.

To replicate the standard power load of 1200 W at 24 V and 50 A, it is feasible to employ either 4 or 5 resistances of 2.2 Ω. Specifically, the usage of 4 resistances should generate 1047 W, while the use of 5 resistances should yield 1309 W.

Conclusions and outlooks

Throughout this thesis project many experimental steps towards the development of the cameras for the Small-Sized Telescopes of the Cherenkov Telescope Array have been faced.

As we have seen in Chapter 4, a fully characterized commissioning facility for the SST cameras has been developed: all of its components have been studied in order to meet specific collaboration requirements and suitable conditions for the calibration of the devices.

Particularly, the facility's setup is able to simulate the background noise coming from the night sky over a wide range, between tens of MHz and tens of GHz. Meanwhile, a laser source, along with several optical components, allows us to simulate the Cherenkov light coming from the γ-ray induced Extensive Air Showers in the atmosphere with a 98.8% uniform beam at 3 m distance from the source and a dynamic range going from one single photon to 3100 photons.

A beam model has also been developed and it could be used to test the cameras closer than 3 m.

The commissioning facility is then a fully operational and well known environment, completely remotely controlled; each step of its characterization is easily reproducible by the users in the facility. It is, therefore, ready to host the future SSTs' devices, to test and calibrate them.

Measurements on the CHEC-S prototype inside the commissioning facility have allowed us to work with a completed device inside the DarkBox; the results coming from such tests stress the need for a full re-calibration of the camera.

Then, Chapter 5 illustrated some preliminary measurements on the SST camera currently under assembly, particularly on the first uncalibrated module and on the heat dissipation within the camera.

The tests on the module showed a non worrying pedestal level and good signal parameters, with a Full Width Half Maximum within the expected range (average value of 8.28 ns) and a 98.17% uniform rise time. Analysis on the pulse time showed a clear ASIC-dependence in the module, an issue that has already been taken into account and will be corrected in the software. The pulse height values also showed a nonuniform behaviour, which again stressed the need for a gain matching procedure to be run on the module.

Indeed, the calibration of the device has to be continued: some of the next steps are the study of the gain, of the photon detection efficiency and of the single photoelectron spectrum.

The tests performed on the heat dissipation within the camera enclosure, although only

preliminary, showed that the cooling system is indeed quite effective and fully working; the use of thermal paste is also recommended. Also, additional tests on the fully assembled camera are needed, together with the use of an alternative power load simulation method.

Acknowledgements

I would like to thank my supervisor Prof. Andrea Chiavassa and my co-supervisor Dr. Davide Depaoli for their constant guidance and useful help during my thesis project; I would also like to thank Dr. Richard White for supervising my internship at Max Planck Institut für Kernphysik and always providing good scientific advice. Indeed, a special thanks goes to everyone in Jim Hinton's department at MPIK for the warm welcome I received in Heidelberg.

A special acknowledgement also goes to Jacopo, who lovingly supported me during most of my master studies, and to my journey companions Rebecca and Sofia.

Finally, but most importantly, a huge thank you to my parents and my sister Miriam for lovingly supporting all of my studies.

Bibliography

[1] F. A. Aharonian, A. M. Atoyan, and T. Kifune. "Inverse Compton gamma radiation of faint synchrotron X-ray nebulae around pulsars". In: *Monthly Notices of the Royal Astronomical Society* 291.1 (Oct. 1997), pp. 162–176. ISSN: 0035-8711. DOI: 10.1093/mnras/291.1.162. eprint: https://academic.oup.com/mnras/article-pdf/291/1/162/4082228/291-1-162.pdf. URL: https://doi.org/10.1093/mnras/291.1.162.

[2] Topchiev et al. "High-energy gamma-ray studying with GAMMA-400". In: (July 2017).

[3] A Hillas. "The Origin of Ultra-High-Energy Cosmic Rays". In: *Annual Review of Astronomy and Astrophysics* 22 (Nov. 2003), pp. 425–444. DOI: 10.1146/annurev.aa.22.090184.002233.

[4] Isabelle A. Grenier and Alice K. Harding. "Gamma-ray pulsars: A gold mine". In: *Comptes Rendus Physique* 16.6 (2015). Gamma-ray astronomy / Astronomie des rayons gamma, pp. 641–660. ISSN: 1631-0705. DOI: https://doi.org/10.1016/j.crhy.2015.08.013. URL: https://www.sciencedirect.com/science/article/pii/S1631070515001486.

[5] A. Hewish et al. "Observation of a Rapidly Pulsating Radio Source". In: *Nature* 217.5130 (Feb. 1968), pp. 709–713. DOI: 10.1038/217709a0.

[6] W. J. Cocke, M. J. Disney, and D. J. Taylor. "Discovery of Optical Signals from Pulsar NP 0532". In: *Nature* 221.5180 (Feb. 1969), pp. 525–527. DOI: 10.1038/221525a0.

[7] G. Fritz et al. "X-ray Pulsar in the Crab Nebula". In: *Science* 164.3880 (May 1969), pp. 709–712. DOI: 10.1126/science.164.3880.709.

[8] H. Bradt, S. Rappaport, and W. Mayer. "X-Ray and Optical Observations of the Pulsar NP 0532 in the Crab Nebula". In: *Nature* 222.5195 (May 1969), pp. 728–730. DOI: 10.1038/222728a0.

[9] D. A. Kniffen et al. "Gamma radiation from the Crab Nebula above 35 MeV". In: *Nature* 251.5474 (Oct. 1974), pp. 397–399. DOI: 10.1038/251397a0.

[10] "Teraelectronvolt emission from the γ-ray burst GRB 190114C". In: *Nature* 575.7783 (2019), pp. 455–458. DOI: 10.1038/s41586-019-1750-x. URL: https://doi.org/10.1038%2Fs41586-019-1750-x.

[11] P. Veres et al. "Observation of inverse Compton emission from a long γ-ray burst". In: *Nature* 575.7783 (2019), pp. 459–463. DOI: 10.1038/s41586-019-1754-6. URL: https://doi.org/10.1038%2Fs41586-019-1754-6.

[12] Noriyasu Kawai et al. "An optical spectrum of the afterglow of a -ray burst at a redshift of z = 6.295". In: *Nature* 440 (Apr. 2006), pp. 184–6. DOI: 10.1038/nature04498.

[13] Pierre Binétruy. "Particle Astrophysics and Cosmology". In: *Particle Physics Beyond the Standard Model*. Ed. by Dmitri Kazakov, Stéphane Lavignac, and Jean Dalibard. Vol. 84. Les Houches. Elsevier, 2006, pp. 457–536. DOI: https://doi.org/10.1016/S0924-8099(06)80029-6. URL: https://www.sciencedirect.com/science/article/pii/S0924809906800296.

[14] J.Gregory Stacy and W.Thomas Vestrand. "Gamma-Ray Astronomy". In: *Encyclopedia of Physical Science and Technology (Third Edition)*. Ed. by Robert A. Meyers. Third Edition. New York: Academic Press, 2003, pp. 397–432. ISBN: 978-0-12-227410-7. DOI: https://doi.org/10.1016/B0-12-227410-5/00274-X. URL: https://www.sciencedirect.com/science/article/pii/B012227410500274X.

[15] S. Abdollahi et al. "Fermi Large Area Telescope Fourth Source Catalog". In: *The Astrophysical Journal Supplement Series* 247.1 (2020), p. 33. DOI: 10.3847/1538-4365/ab6bcb. URL: https://doi.org/10.3847%2F1538-4365%2Fab6bcb.

[16] Cao, Zhen. "LHAASO Status and Physics Results". In: *EPJ Web Conf.* 280 (2023), p. 01003. DOI: 10.1051/epjconf/202328001003. URL: https://doi.org/10.1051/epjconf/202328001003.

[17] J. Matthews. "A Heitler model of extensive air showers". In: *Astroparticle Physics* 22.5 (2005), pp. 387–397. ISSN: 0927-6505. DOI: https://doi.org/10.1016/j.astropartphys.2004.09.003. URL: https://www.sciencedirect.com/science/article/pii/S0927650504001598.

[18] J. V. Jelley. "Čerenkov radiation and its applications. (Pergamon Press, London, 1958. x – 304 pages. 65s. net)." In: 1960. URL: https://api.semanticscholar.org/CorpusID:117240405.

[19] M. Doering et al. *Measurement of the Cherenkov light spectrum and of the polarization with the HEGRA-IACT-system*. 2001. arXiv: astro-ph/0107149 [astro-ph].

[20] *NASA public domain*. URL: https://commons.wikimedia.org/w/index.php?.

[21] *The CTA Consortium. CTA Website. Online*. https://www.cta-observatory.org/.

[22] Justus Zorn. "Development of a SiPM-based camera for the Large Size Telescope of CTA and study of its performance". PhD thesis. Ruperto-Carola-University of Heidelberg, 2019.

[23] Heinrich J. Völk and Konrad Bernlöhr. "Imaging Very High Energy Gamma-Ray Telescopes". In: *Exper. Astron.* 25 (2009), pp. 173–191. DOI: 10.1007/s10686-009-9151-z. arXiv: 0812.4198 [astro-ph].

[24] *Weather Spark*. URL: https://weatherspark.com/.

[25] B.S. Acharya et al. "Introducing the CTA concept". In: *Astroparticle Physics* 43 (2013). Seeing the High-Energy Universe with the Cherenkov Telescope Array - The Science Explored with the CTA, pp. 3–18. ISSN: 0927-6505. DOI: https://doi.org/10.1016/j.astropartphys.2013.01.007. URL: https://www.sciencedirect.com/science/article/pii/S0927650513000169.

[26] Richard White et al. "The Small-Sized Telescopes for the Southern Site of the Cherenkov Telescope Array". In: *Proceedings of 37th International Cosmic Ray Conference — PoS(ICRC2021)*. Sissa Medialab, 2021. DOI: 10.22323/1.395.0728. URL: https://doi.org/10.22323%2F1.395.0728.

[27] J.S. Lapington. "The silicon photomultiplier-based camera for the Cherenkov Telescope Array small-sized telescopes". In: *Nuclear Instruments and Methods in Physics Research Section A: Accelerators, Spectrometers, Detectors and Associated Equipment* 1055 (2023), p. 168433. ISSN: 0168-9002. DOI: https://doi.org/10.1016/j.nima.2023.168433. URL: https://www.sciencedirect.com/science/article/pii/S0168900223004230.

[28] G. Romeo et al. "Novel silicon photomultipliers suitable for dual-mirror small-sized telescopes of the Cherenkov telescope array". In: *Nuclear Instruments and Methods in Physics Research Section A: Accelerators, Spectrometers, Detectors and Associated Equipment* 908 (2018), pp. 117–127. DOI: 10.1016/j.nima.2018.08.035. URL: https://doi.org/10.1016%2Fj.nima.2018.08.035.

[29] R. White for the CTA Collaboration. *SST Camera Design Report*.

[30] Davide Depaoli. "Status of the SST Camera for the Cherenkov Telescope Array". In: *PoS* ICRC2023 (2023), p. 771. DOI: 10.22323/1.444.0771.

[31] "TARGET: A digitizing and trigger ASIC for the Cherenkov telescope array". In: *AIP Conference Proceedings*. Author(s), 2017. DOI: 10.1063/1.4969033. URL: https://doi.org/10.1063%2F1.4969033.

[32] Charles Kittel. *Introduction to solid state physics*. John Wiley & sons, inc, 2005.

[33] A Ghassemi, K Sato, and K Kobayashi. "Silicon as a Photodetector technology - HAMAMATSU - MPPC Technical notes". In: (2017).

[34] Davide Depaoli. "Cherenkov Camera and Analysis Development for Highest-Energy Gamma-Ray Astronomy". PhD thesis. University of Turin, 2022.

[35] Fabio Acerbi and Stefan Gundacker. "Understanding and simulating SiPMs". In: *Nuclear Instruments and Methods in Physics Research Section A: Accelerators, Spectrometers, Detectors and Associated Equipment* 926 (2019). Silicon Photomultipliers: Technology, Characterisation and Applications, pp. 16–35. ISSN: 0168-9002. DOI: https://doi.org/10.1016/j.nima.2018.11.118. URL: https://www.sciencedirect.com/science/article/pii/S0168900218317704.

[36] A.L. Lacaita et al. "On the bremsstrahlung origin of hot-carrier-induced photons in silicon devices". In: *IEEE Transactions on Electron Devices* 40.3 (1993), pp. 577–582. DOI: 10.1109/16.199363.

[37] *Hamamatsu Photonics, Hamamatsu S12642-1616PA-50 SiPM data sheet.* URL: https://www.hamamatsu.com/jp/en.html.

[38] J. Zorn. "CHEC—A compact high energy camera for the Cherenkov Telescope Array". In: *Nuclear Instruments and Methods in Physics Research Section A: Accelerators, Spectrometers, Detectors and Associated Equipment* 936 (2019). Frontier Detectors for Frontier Physics: 14th Pisa Meeting on Advanced Detectors, pp. 229–230. ISSN: 0168-9002. DOI: https://doi.org/10.1016/j.nima.2018.09.138. URL: https://www.sciencedirect.com/science/article/pii/S0168900218312981.

[39] R. White for the CTA Collaboration. *SST Camera Production Plan.*

[40] Rongqing Hui. "Chapter 4 - Photodetectors". In: *Introduction to Fiber-Optic Communications.* Ed. by Rongqing Hui. Academic Press, 2020, pp. 125–154. ISBN: 978-0-12-805345-4. DOI: https://doi.org/10.1016/B978-0-12-805345-4.00004-4.

[41] Michele Palatiello et al. *Test results of a prototype device to calibrate the Large Size Telescope camera proposed for the Cherenkov Telescope Array.* 2017. arXiv: 1708.09289 [astro-ph.IM].

[42] *Thorlabs.* URL: https://www.thorlabs.com/.

[43] *High Performance Photodiode Sensors - 918D series.* Newport Corporation.

[44] *RP Photonics, flat-top beams.* URL: https://www.rp-photonics.com/flat_top_beams.html.

[45] *Pico Technology TC-08 datasheet.* URL: https://www.farnell.com/datasheets/2642973.pdf.

[46] *Semiconductors, Doping and the P-N Junction.* https://devxplained.eu/en/blog/p-n-junction.

[47] A. Nepomuk Otte. "On the efficiency of photon emission during electrical breakdown in silicon". In: *Nuclear Instruments and Methods in Physics Research Section A: Accelerators, Spectrometers, Detectors and Associated Equipment* 610.1 (2009). New Developments In Photodetection NDIP08, pp. 105–109. ISSN: 0168-9002. DOI: https://doi.org/10.1016/j.nima.2009.05.085. URL: https://www.sciencedirect.com/science/article/pii/S0168900209010390.